



저작자표시-비영리-변경금지 2.0 대한민국

이용자는 아래의 조건을 따르는 경우에 한하여 자유롭게

- 이 저작물을 복제, 배포, 전송, 전시, 공연 및 방송할 수 있습니다.

다음과 같은 조건을 따라야 합니다:



저작자표시. 귀하는 원저작자를 표시하여야 합니다.



비영리. 귀하는 이 저작물을 영리 목적으로 이용할 수 없습니다.



변경금지. 귀하는 이 저작물을 개작, 변형 또는 가공할 수 없습니다.

- 귀하는, 이 저작물의 재이용이나 배포의 경우, 이 저작물에 적용된 이용허락조건을 명확하게 나타내어야 합니다.
- 저작권자로부터 별도의 허가를 받으면 이러한 조건들은 적용되지 않습니다.

저작권법에 따른 이용자의 권리는 위의 내용에 의하여 영향을 받지 않습니다.

이것은 [이용허락규약\(Legal Code\)](#)을 이해하기 쉽게 요약한 것입니다.

[Disclaimer](#)

이학박사 학위논문

**Efficient Preparation of
Conjugated Block Copolymer Nanostructures
by One-Shot ROMP
and Self-Assembly during Polymerization**

원-샷 고리개환복분해중합과
합성 도중 자기조립 현상을 이용한
공액고분자 블록공중합체 나노구조의
효율적 합성법

2018년 2월

서울대학교 대학원
화학부 유기화학 전공
신수용

Abstract

Efficient Preparation of Conjugated Block Copolymer Nanostructures by One-Shot ROMP and Self-Assembly during Polymerization

Suyong Shin

Department of Chemistry

The Graduate School

Seoul National University

Development of strategies for block copolymer self-assembly in solution enabled preparation of various nanostructures having desired shape and functionality with high controllability. Even though the method for efficient and facile preparation of controlled nanostructures can be a bridge between academic researches developing novel nanomaterials and their practical applications, studies about simple preparation method have attracted less attention. Following four chapters describes the facile strategies for preparation of nanostructures containing useful conjugated block copolymers.

Chapter 2 reports the development of one-shot in situ nanoparticlization of conjugated polymers (INCP) method using

polyacetylene (PA) block copolymers. Large difference of reactivity between two comonomers, norbornene (NB) derivatives and cyclooctatetraene (COT) led to propagation of each monomer sequentially in the mixture solution, and resulting insoluble PA induced *in situ* self-assembly during polymerization. Additionally, effect of using a different type of monomers, *endo*-tricyclo[4.2.2.0]deca-3,9-diene (TD) derivatives, on polymerization kinetics and morphologies of resulting nanostructures was studied.

Chapter 3 presents the one-shot INCP of poly(*para*-phenylenevinylene) (PPV) block copolymers. One-shot ROMP of [2.2]paracyclophane-1,9-diene (PCPDE) with NB or TD produced nanostructures having fluorescent properties, useful for further applications. More bulky reaction site of PCPDE had an effect on one-shot polymerization kinetics, and the influence of the different kinetics on the mechanism of *in situ* self-assembly was demonstrated.

In Chapter 4, perfect one-shot block copolymerization and ultra-fast light-induced crystallization-driven self-assembly (LI-CDSA) of dimethoxy substituted PPV (MeO-PPV) block copolymers are reported. Simple and fast *cis* to *trans* photoisomerization of MeO-PPV led to LI-CDSA in THF, which could control growth of assembly structures in living manner.

The final chapter shows the application of fluorescent nanostructures prepared by one-shot INCP method to a chemical sensor in aqueous solution. Semi-solid state interaction of PPV core resulted in highly efficient fluorescence quenching toward explosive nitroaromatics in solution, depending on morphology of nanostructures. Additionally, the nanoparticles could selectively detect neutral analytes against charged molecules.

In summary, this thesis describes the development of facile

preparation of conjugated block copolymer nanostructures combining one-shot polymer synthesis and efficient self-assembly methods such as INCP and LI-CDSA. Additionally, we propose useful application of prepared nanostructures. We hope these researches will provide more variety to the strategies for efficient preparation of functional nanomaterials.

Keywords: *in situ* nanoparticlization of conjugated polymers, one-shot block copolymerization, ring-opening metathesis polymerization, polyacetylene, poly(*para*-phenylenevinylene), crystallization-driven self-assembly, chemical sensor

Student number: 2012-20281

Table of Contents

Abstract	i
----------------	---

Table of Contents	iv
-------------------------	----

Chapter 1. Introduction to strategies for facile preparation of nanostructures by self-assembly of block copolymers

1.1. Introduction	2
1.2. One-shot block copolymerization	3
1.3. <i>In situ</i> self-assembly	5
1.4. Thesis research	7
1.5. References	8

Chapter 2. One-shot *in situ* nanoparticlization of Polyacetylene block copolymers

2.1. Abstract	10
2.2. Introduction	11
2.3. Results and discussion	14
2.3.1. One-shot ring opening metathesis polymerization: Effect of the 1 st block on polymerization kinetics	14
2.3.2. One-shot <i>in situ</i> nanoparticlization: Effect of the 1 st block on nanostructures	23
2.4. Conclusion	36
2.5. Experimental section	37
2.6. Supporting information	43
2.7. References	43

Chapter 3. One-shot *in situ* nanoparticlization of Poly(*para*-phenylenevinylene) block copolymers

3.1. Abstract	45
3.2. Introduction	46
3.3. Results and discussion	49
3.3.1. One-shot <i>in situ</i> nanoparticlization of PNB- <i>b</i> -PPV: Effect of the 2 nd block on polymerization kinetics and nanostructures ·	49
3.3.2. One-shot <i>in situ</i> nanoparticlization of PTD- <i>b</i> -PPV: Effect of polymerization conditions on nanostructures	58
3.3.3. One-shot <i>in situ</i> nanoparticlization of PTD- <i>b</i> -PPV: Effect of polymerization kinetics on nanostructures	68
3.4. Conclusion	80
3.5. Experimental section	81
3.6 Supporting information	91
3.7. References	94

Chapter 4. One-shot block copolymerization and ultra-fast light-induced crystallization-driven self-assembly of Poly(*para*-phenylenevinylene-2,5-dimethoxy-*para*-phenylenevinylene) block copolymers

4.1. Abstract	97
4.2. Introduction	98
4.3. Results and discussion	100
4.3.1. One-shot synthesis of perfect block copolymers and their self-assembly by photoisomerization	100
4.3.2. Light-induced living crystallization-driven self-assembly ·	111

4.4. Conclusion	120
4.5. Experimental section	121
4.6. Supporting information	128
4.7. References	138

Chapter 5. Application of amplifying fluorescent polymer nanoparticles to selective detection of charge-neutral analytes

5.1. Abstract	140
5.2. Introduction	141
5.3. Results and discussion	143
5.4. Conclusion	150
5.5. Experimental section	151
5.6. Supporting information	154
5.7. References	156

Appendix: Supramolecular switching between flat sheets and helical tubules triggered by coordination interaction

Abstract	158
Introduction	159
Results and discussion	162
Conclusion	171
Experimental section	172
Supporting information	176
References	177

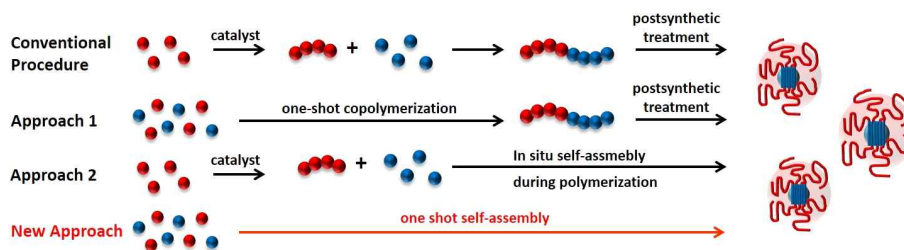
Abstract (Korean)	179
--------------------------------	------------

Chapter 1.

Introduction to strategies for facile preparation of nanostructures by self-assembly of block copolymers

1.1. Introduction

Molecular self-assembly opened a world of functional soft materials which structures and functionalities can be systematically tuned by a bottom-up approach.¹ Different molecular structures, compositions, properties, and their non-covalent interactions modulate shapes and functionalities of resulting structures in both bulk and solution states. Block copolymers have attracted considerable attention as building blocks for self-assembly due to high stability, ease of synthesis, and rich chemical variability.² Especially in solution, polymer assembly structures can exhibit complex morphologies with much higher stability having about three orders of magnitude lower critical micelle concentration than small-molecule aggregates, enabling applications in many fields such as biomaterials, photoelectric materials, sensors and catalysts.² Therefore, self-assembly of block copolymers into various types of nanostructures in solution has been studied extensively in recent years, since 1995.³ Not only preparation of conventional simple structures such as micelles and vesicles but also preparation of complex multicompart ment micelles which can lead to the formation of superstructures by their secondary self-assembly have been developed.⁴ The fabrication of such nanostructures requires multi-step synthetic procedures for block copolymers and then post-synthetic treatments such as the addition of selective solvents, dialysis, aging, or addition of glue molecules to induce self-assembly (Scheme 1.1, conventional procedure).²⁻⁴ If these time-demanding procedures at very low concentration can be simplified, self-assembly of block copolymers will become a more powerful tool for developing functional soft materials enabling their practical applications. However, in spite of well-studied methods for manipulating morphologies of nanostructures, researches for efficient self-assembly processes were still limited.



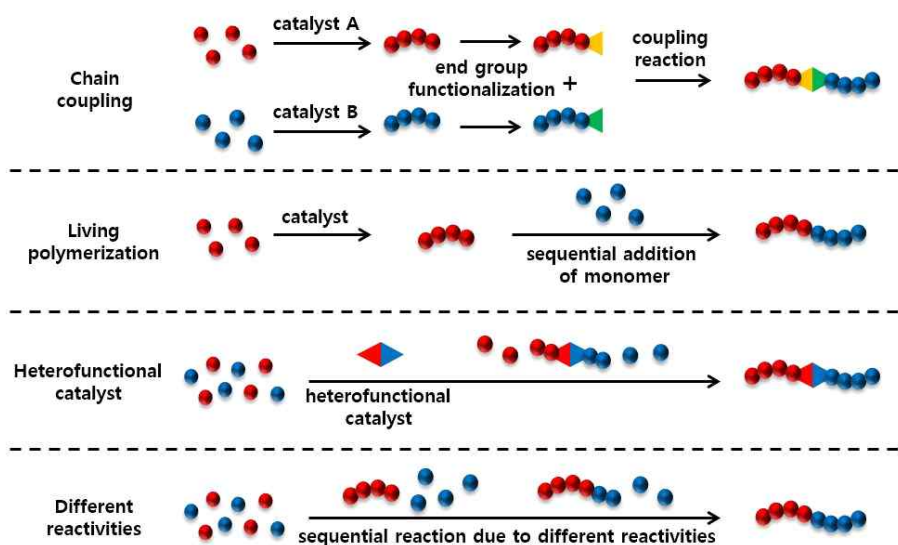
Scheme 1.1. Conventional and new strategies towards self-assembly of block copolymers.

1.2. One-shot block copolymerization

There are two viable strategies to simplify the procedure for preparation of self-assembled nanostructures from block copolymers. One is to develop a simpler synthetic process for block copolymers (Scheme 1.1 strategy 1). Block copolymers can be synthesized in different techniques (Scheme 1.2).⁵ The first method is using coupling reactions between the end groups of two different polymers (Scheme 1.2, the first scheme). Even though this method can provide unlimited variety to composition of block copolymers, it suffers from imperfect conversion resulting in remaining homopolymers and also from multi-step reactions and purification. Development of living polymerization enabled facile preparation of block copolymers by sequential addition of monomers in one-pot, but it still needs addition of monomers in appropriate time and condition (Scheme 1.2, the second scheme).

The most simple synthetic method is a one-shot polymerization method where all comonomers in the reaction vessel are polymerized in a single step.⁵⁻⁷ The one-shot block polymerization can be achieved by two different approaches. The first method is using heterofunctional initiators which contain two or more different initiation sites (Scheme 1.2, the third scheme).^{5,6} If the initiation sites tolerate each other and

the monomers at same reaction condition, the heterofunctional initiators could produce block copolymers in one-step by two different mechanisms simultaneously. For example, Grubbs' group reported a hetero-functional initiator which could do atom transfer radical polymerization (ATRP) and ring-opening metathesis polymerization (ROMP) simultaneously.^{6a} The heterofunctional initiator involving ring-opening polymerization (ROP) and nitroxide-mediated polymerization (NMP) was also reported by Hawker's group.^{6b}



Scheme 1.2. Different approaches to synthesize block copolymers.

Another approach to the one-shot copolymerization is using comonomers of the block copolymers which have large differences in their reactivities (Scheme 1.2, the fourth scheme).⁷ Endo's group^{7a} and Bisht's group^{7b} synthesized one-shot block copolymers using comonomers which showed different ROP reactivities. Russel group reported one-step synthesis of block copolymer using styrene and maleic

anhydride as the comonomers via nitroxide-mediated polymerization (NMP).^{7c} However, reports on the synthesis of block copolymers using this method are very rare due to difficulties of finding appropriate monomer pairs.

1.3. *In situ* self-assembly

The second strategy towards a more facile self-assembly procedure from block copolymers is to simplify or even eliminate post-synthetic treatments via the direct, *in situ* formation of the nanostructures (Scheme 1.1 strategy 2). Generally, block copolymers are synthesized in a good solvent for both blocks, thereby requiring additional procedures to provide driving force for self-assembly. Polymerization-induced self-assembly (PISA) method was developed for simplifying these processes by using block-selective solvents as polymerization media (Figure 1.1, left).⁸ Therefore this method leads to the direct formation of self-assembled nanostructures during polymerization by taking advantage of the vastly different solubilities of the constituting blocks of the copolymers. PISA typically uses reversible addition-fragmentation chain transfer (RAFT) polymerization to produce amphiphilic block copolymers in polar solvents such as water and methanol. Increasing degree of polymerization (DP) of second hydrophobic block induces self-assembly from spherical micelle morphology to cylindrical micelles and then platelets or vesicles depending on a block ratio. Recently, living anionic polymerization of block copolymers containing crystallizable core-forming block in *n*-hexanes also enabled *in situ* formation of uniform cylindrical micelles by polymerization-induced crystallization-driven self-assembly (PI-CDSA).⁹

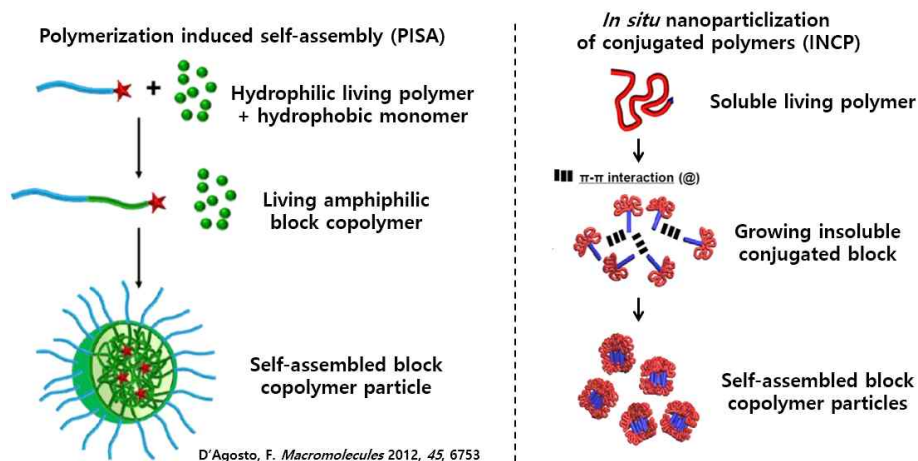


Figure 1.1. General principles of polymerization-induced self-assembly (PISA, left) and *in situ* nanoparticlization of conjugated polymers (INCP, right).

In situ nanoparticlization of conjugated polymers (INCP) is another method for preparing nanostructures composed of block copolymers in solution without post-treatment (Figure 1.1, right).¹⁰ INCP takes advantage of the strong π - π interactions and insolubility of the conjugated polymer without solubilizing sidechains as the driving forces for self-assembly. As a result, nanostructure formation spontaneously occurs in any organic solvent, and the resulting nanostructures are highly stable under heat and mechanical forces. Such strong interaction highly traps shape of the nanostructures during synthesis, resulting in nanocaterpillar, nanostar, and nanonetwork structures grown by step-growth attachment of micelle structures. Diblock copolymers containing insoluble conjugated block were synthesized by living polymerization methods such as ring-opening metathesis polymerization (ROMP),^{10a} cyclopolymerization,^{10b} and catalyst-transfer polycondensation (CTP).^{10c} The INCP method can provide well-defined nanostructures

containing conjugated polymers which have useful properties such as conductivity and optoelectronic properties, therefore the method is expected to be applied for simple preparation of functional nanomaterials in large scale.

1.4. Thesis research

Although there have been recent attempts to simplify synthesis and self-assembly process of block copolymers, it is still challenging to develop the most simple and efficient approach which combines above two strategies, one-shot copolymerization of comonomers leading to direct formation of nanostructures (Scheme 1.1 new approach). This research describes the development of efficient strategies for preparation of conjugated block copolymer nanostructures by combining one-shot ROMP and INCP, and the application of resulting nanostructures.

Chapter 2 reports the development of one-shot INCP method using polyacetylene (PA) block copolymers. Large difference of reactivity between norbornene (NB) derivatives and cyclooctatetraene (COT) led to propagation of each monomer sequentially, and resulting insoluble PA induced *in situ* self-assembly during polymerization. Additionally, effect of using different type of monomers, *endo*-tricyclo[4.2.2.0]deca-3,9-diene (TD) derivatives, on polymerization kinetics and morphologies of resulting nanostructures was studied.

Chapter 3 presents the one-shot INCP of poly(*para*-phenylenevinylene) (PPV) block copolymers. One-shot ROMP of [2.2]paracyclophane-1,9-diene (PCPDE) with NB or TD produced nanostructures having fluorescent properties, useful for further applications. More bulky reaction site of PCPDE had an effect on one-shot polymerization kinetics, and the influence of the different kinetics on the mechanism of *in situ* self-assembly was demonstrated.

In Chapter 4, perfect one-shot block copolymerization and ultra-fast light-induced CDSA (LI-CDSA) of dimethoxy substituted PPV (MeO-PPV) block copolymers are reported. Modulation of polymerization kinetics and solubility by adding minimum substituent on PPV was studied. Simple and fast *cis* to *trans* photoisomerization of MeO-PPV led to LI-CDSA in THF, which could control growth of assembly structures in living manner.

Chapter 5 shows the application of fluorescent nanostructures prepared by one-shot INCP method to a chemical sensor in aqueous solution. Semi-solid state interaction of PPV core resulted in highly efficient fluorescence quenching toward explosive nitroaromatics in solution, depending on morphology of nanostructures. Additionally, the nanoparticles could selectively detect neutral analytes against charged molecules.

1.5. References

- (1) Whitesides, G. M.; Mathias, J. P.; Seto, C. T. *Science* **1991**, *254*, 1312.
- (2) Mai, Y.; Eisenberg, A. *Chem. Soc. Rev.* **2012**, *41*, 5969.
- (3) (a) van Hest, J. C. M.; Delnoye, D. A. P.; Baars, M. W. P. L.; van Genderen, M. H. P.; Meijer, E. W. *Science* **1995**, *268*, 1592. (b) Zhang, L.; Eisenberg, A. *Science* **1995**, *268*, 1728. (c) Zhang, L.; Yu, K.; Eisenberg, A. *Science* **1996**, *272*, 1777.
- (4) (a) Moughton, A. O.; Hillmyer, M. A.; Lodge, T. P. *Macromolecules* **2012**, *45*, 2. (b) Qiu, H.; Gao, Y.; Boott, C. E.; Gould, O. E. C.; Harniman, R. L.; Miles, M. J.; Webb, S. E. D.; Winnik, M. A.; Manners, I. *Science* **2016**, *352*, 697.
- (5) Bernaerts, K. V.; Du Prez, F. E. *Prog. Polym. Sci.* **2006**, *31*, 671.
- (6) (a) Bielawski, C. W.; Louie, J.; Grubbs, R. H. *J. Am. Chem. Soc.*

- 2000**, *122*, 12872. (b) Mecerreyes, D.; Moineau, G.; Dubois, P.; Jérôme, R.; Hedrick, J. L.; Hawker, C. J.; Malmström, E. E.; Trollsas, M. *Angew. Chem., Int. Ed.* **1998**, *37*, 1274.
- (7) (a) Ariga, T.; Takata, T.; Endo, T. *Macromolecules* **1993**, *26*, 7106. (b) Wu, R.; AL-Azemi, T. F.; Bisht, K. S. *Macromolecules* **2009**, *42*, 2401. (c) Benoit, D.; Hawker, C. J.; Huang, E. E.; Lin, Z.; Russell, T. P. *Macromolecules* **2000**, *33*, 1505.
8. Charleux, B.; Delaittre, G.; Rieger, J.; D'Agosto, F. *Macromolecules* **2012**, *45*, 6753.
9. Boott, C. E.; Gwyther, J.; Harniman, R. L.; Hayward, D. W.; Manners, I. *Nat. Chem.* **2017**, *9*, 785
10. (a) Yoon, K.-Y.; Lee, I.-H.; Kim, K. O.; Jang, J.; Lee, E.; Choi, T.-L. *J. Am. Chem. Soc.* **2012**, *134*, 14291. (b) Kim, J.; Kang, E.-H.; Choi, T.-L. *ACS Macro Lett.* **2012**, *1*, 1090. (c) Lee, I.-H.; Amaladass, P.; Yoon, K.-Y.; Shin, S.; Kim, Y.-J.; Kim, I.; Lee, E.; Choi, T.-L. *J. Am. Chem. Soc.* **2013**, *135*, 17695.

Chapter 2.

One-shot *in situ* nanoparticlization of Polyacetylene block copolymers

2.1. Abstract

A simple one-shot method for nanostructure formation by the synthesis of Polyacetylene (PA) block-like copolymers was developed. The block-like copolymers could be prepared by the one-shot ring-opening metathesis polymerization (ROMP) of comonomers with large differences in their reactivities because the monomers that formed the first block, namely norbornene (NB) derivatives or endo-tricyclo[4.2.2.0]deca-3,9-diene (TD) derivatives, polymerized much faster than the monomers that formed the second PA block, cyclooctatetraene (COT). Better accessibility of TD to catalytic site led to the synthesis of near-perfect block copolymers. Owing to insoluble PA block, the copolymers formed various nanostructures such as nanospheres, nanocaterpillars, nanoaggregates, and two-dimensional sheet-like structures depending on the chemical structures of the soluble shell polymers and feed ratio of COT, during polymerization process.

2.2 Introduction

Polyacetylene (PA) is the simplest conjugated polymer, which opened a field of conductive polymers.¹ Despite intense interest in PA leading to extensive researches about synthetic methods and chemical and physical properties of it, applications of PA are still challenging because of low stability in air and insoluble property in any solvent. In general, introducing solubilizing substituents and synthesizing block copolymers containing soluble block were common methods to overcome the solubility problem of insoluble conjugated polymers including PA.² Approaching problem from the opposite direction, taking advantage of the insoluble property of PA, we developed direct preparation of nanostructures composed of PA block copolymers during polymerization (Figure 2.1).³ The PA block copolymers were synthesized by ring-opening metathesis polymerization with sequential addition of norbornene (NB) derivatives and cyclooctatetraene (COT), using the highly active and fast initiating third-generation Grubbs catalyst as the initiator (Figure 2.1, a).^{3a} After polymerization of soluble polynorbornene (PNB) block, propagation of insoluble PA block led to aggregation of polymers into spherical micelle structures due to strong π - π interaction between PAs. PA second block could be further propagated with living chain end expanding the core of micelles composed of insoluble PAs. When PNB shell could not solvate the enlarged PA core, the cores spontaneously attached each other to prevent exposure of insoluble part and produced undulated nanocaterpillar structures composed of connected spherical micelles without rearrangement of polymer chains to smooth cylindrical shape because of highly trapped state of cores due to strong π - π interaction. We named this efficient method to prepare nanostructures utilizing insolubility of conjugated polymers for the driving force for

self-assembly during polymerization as *in situ* nanoparticlization of conjugated polymers (INCP). Thereafter, preparation of more complex three-dimensional aggregates composed of PA block copolymers by INCP method was reported (Figure 2.1, b).^{3b} Changing soluble 1st block from PNB to poly(endo-tricyclo[4.2.2.0]deca-3,9-diene) (PTD) which had more rigid property induced further interaction of nanocaterpillars to aggregated structures due to more exposure of PA cores.

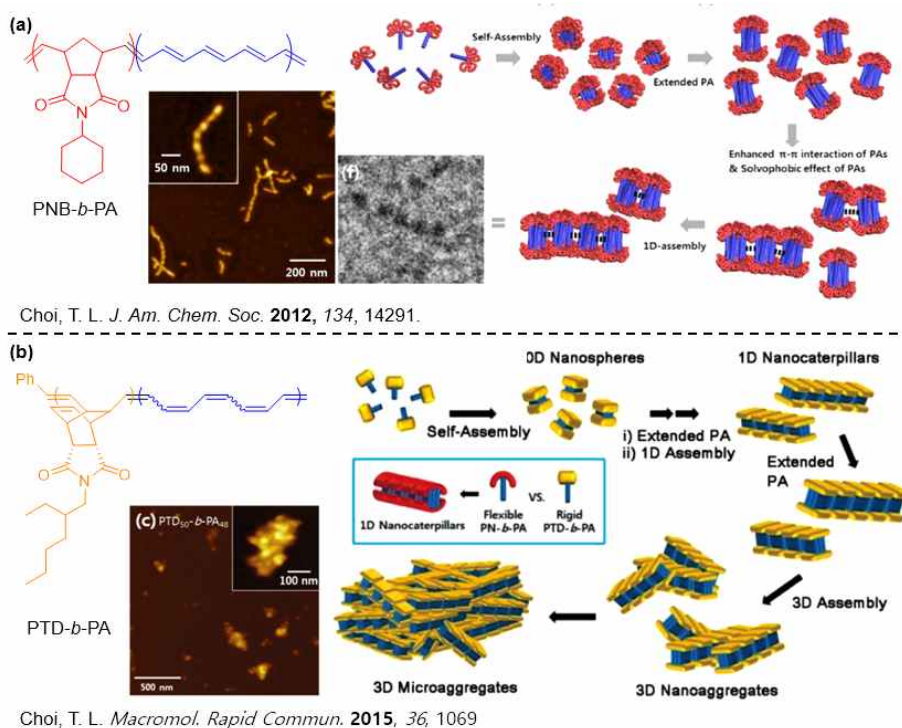


Figure 2.1. Previous reports about INCP of (a) PNB-*b*-PA and (b) PTD-*b*-PA into nanocaterpillar and nanoaggregate structures.³

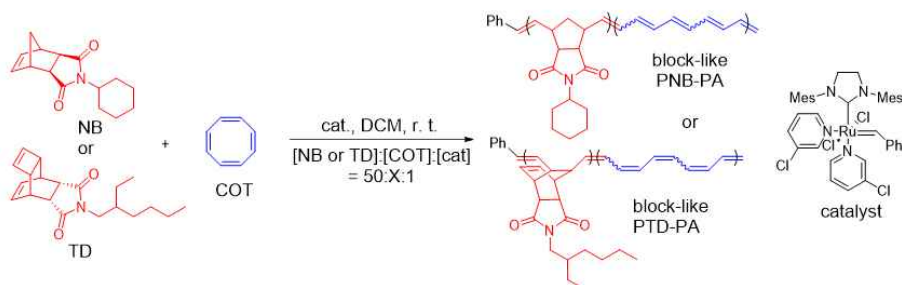
During our previous researches preparing nanostructures composed of PNB-*b*-PA and PTD-*b*-PA by simple INCP method, we observed a vastly different rate between the ROMP of NB or TD

monomers (typically 10~30 min for degree of polymerization (DP)=50) and the ROMP of COT (6~18 hours for DP=50).³ By taking advantage of the substantial difference in reactivity between the comonomers, we envisioned that block copolymers could be prepared by the simple copolymerization of NB or TD and COT in one-shot, because NB or TD would be consumed prior to the ROMP of COT. Then, an extremely simple method for the self-assembly of block copolymers would be feasible via a one-shot production of block copolymers containing insoluble PA block which could undergo direct self-assembly via INCP.

In this chapter, we report a simple one-shot INCP method using ROMP to produce block-like copolymers that spontaneously undergo various self-assembly processes. First, block-like copolymers containing a PA block were prepared by the one-shot ROMP of NB or TD and COT. Effect of two different types of 1st block monomers, NB and TD derivatives, on polymerization kinetics were observed by various analysis. Second, nanostructures prepared during one-shot block copolymerization were observed and compared to the nanostructures of the block copolymers obtained by the conventional sequential addition method. Modulating structure of solubilizing 1st block could affect to shape of resulting nanostructures.

2.3. Results and discussion

2.3.1. One-shot ring opening metathesis polymerization: Effect of the 1st block on polymerization kinetics



Scheme 2.1. Synthesis of PNB-PA and PTD-PA block-like copolymers by one-shot ROMP

To determine whether or not one-shot copolymerization of NB or TD and COT would produce block copolymers, we synthesized copolymers using the one-shot method summarized in Scheme 2.1. An initiator, the highly active and fast-initiating third-generation Grubbs catalyst, was added to the reaction mixture of two comonomers, NB or TD and COT, in dichloromethane (DCM). The conversion of each comonomer, NB or TD and COT, during one-shot copolymerization was monitored via in situ ¹H NMR (Figure 2.2). The kinetics experiment using NB and COT as the comonomers was conducted at 5 °C owing to the rapid polymerization of NB with the third-generation Grubbs catalyst at room temperature, whereas the conversion of TD and COT was slow enough to be monitored at room temperature. Since the ROMP of NB and TD was much faster than the ROMP of COT, only a small portion of, or almost no COT was consumed until the NB or TD monomer was fully consumed (Figure 2.2, a and b). By calculating the

propagation rate of each monomer during one-shot ROMP from the logarithmic conversion vs. time plot, we observed that the propagation rate of NB was 24-times faster than that of COT (0.066 vs. 0.0028 for the rate constants, Figure 2.2, c), and the propagation rate of the TD was 170-times faster than that of COT (0.12 vs. 0.00071 for the rate constants, Figure 2.2, d).

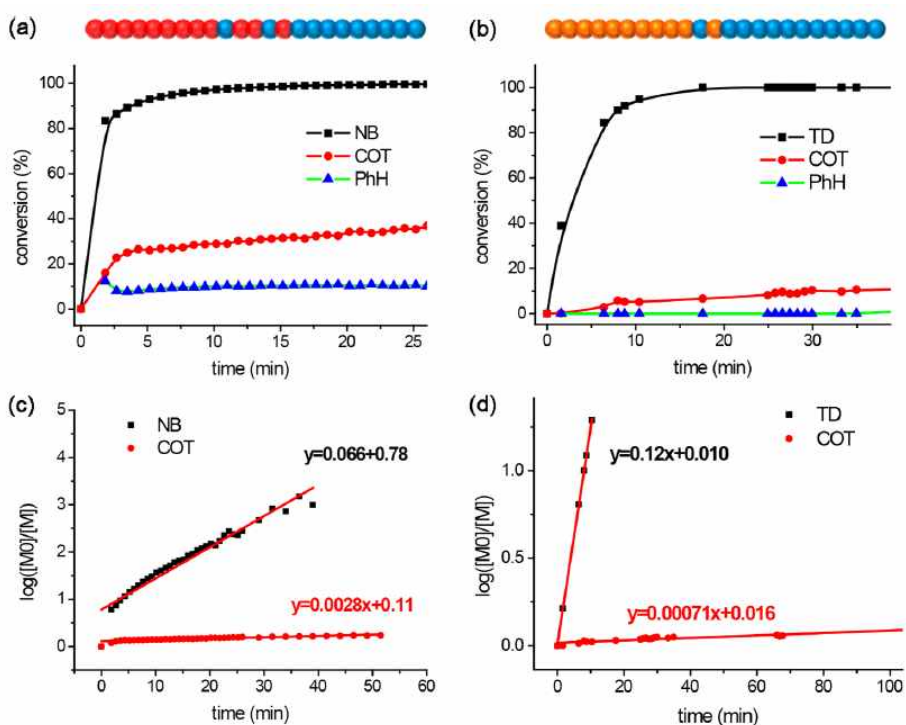


Figure 2.2. Conversion vs. time and logarithmic conversion vs. time plot for ROMP of (a),(c) NB and COT at 5 °C and (b),(d) TD and COT at room temperature with feed ratio $[NB]$ (or $[TD]$): $[COT] = 50:30$ at 140 mM based on the concentration of COT.

This large difference in the reaction rates between NB or TD and COT arises from the difference in the ring-opening rate of each

monomer. Since the driving force of the ring-opening of cyclic monomers is the relief of ring strain, the ring-opening of NB and TD is very fast and irreversible due to the large ring-strain energy of the olefin on the bridged bicyclic six-membered ring of NB (27 kcal/mol) and cyclobutene of TD (30 kcal/mol). However, the ring-opening of the less-strained COT (2.5 kcal/mol) is very slow and reversible.⁴ Therefore, when the initiator is added to the reaction mixture containing NB or TD and COT, the ring-opening of NB or TD preferentially occurs to produce PNB or PTD polymers, and subsequently the ring-opening of COT occurs slowly and reversibly to form PA.

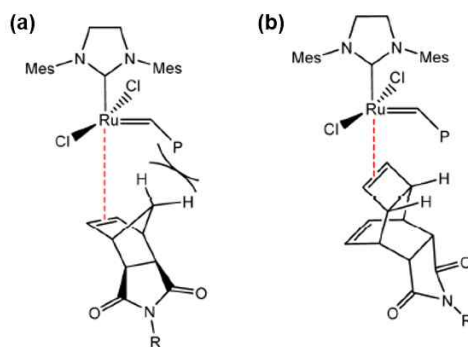


Figure 2.3. Schematic explanation for the steric on (a) NB and (b) TD during approaching to initiator.⁵

Upon comparing the relative reaction rate between TD and COT ($k_{p,TD}/k_{p,COT}$) and that of NB and COT ($k_{p,NB}/k_{p,COT}$), we observed that the former was seven times larger than the latter ($k_{p,TD}/k_{p,COT} = 170$ vs. $k_{p,NB}/k_{p,COT}$, Figure 2.2, d and c). This phenomenon could be explained by the difference in the rate of catalyst coordination to the NB and TD monomers. Previously, we reported that the initiator could bind faster to the TD derivatives than to the NB derivatives, because

the cyclobutene moiety on the TD monomers has less local steric hindrance around its active olefin, whereas the olefin on the NB monomers is more hindered due to a neighboring bridging methylene group (Figure 2.3).⁵ Thus, one can expect that the preference toward the TD monomer over COT would lead to a near-perfect, block-like microstructure for the PTD-PA copolymer, even via the one-shot copolymerization method.

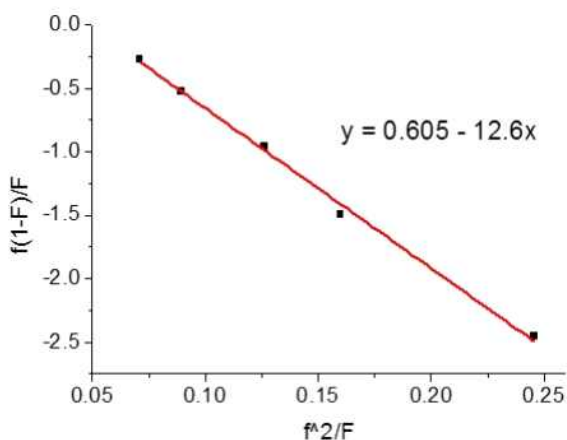


Figure 2.4. Fineman-Ross plot of the copolymerization using NB and COT as the comonomers.

To confirm the reactivity differences of the comonomers, the reactivity ratios for each pair of the comonomers were measured using Fineman-Ross equation (Experimental section).⁶ As a result, the reactivity ratios of NB and COT were calculated to be $r_1 = 12.6$ for NB and $r_2 = 0.605$ for COT (Figure 2.4). These values matched well with the values for gradient copolymerization ($r_1 \gg 1 \gg r_2$). However, we could not estimate the reactivity ratios of TD and COT by the same method because COT was not consumed at all at the

early stage due to the too large different reactivities between the TD and COT monomers.

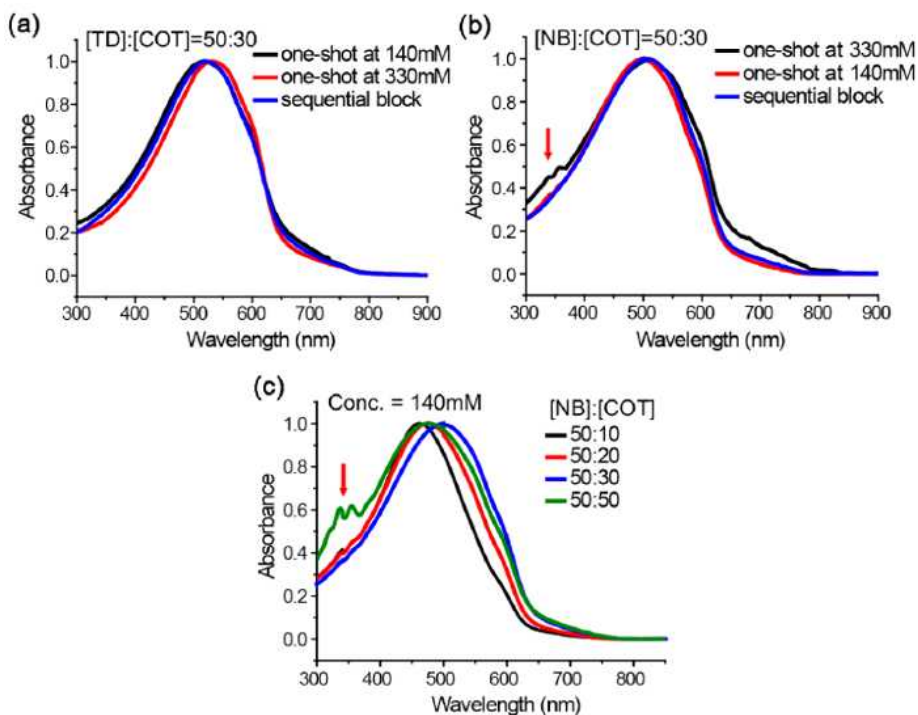


Figure 2.5. UV/Vis absorbance spectra of the block-like copolymers polymerized at different concentrations, and comparison to authentic block copolymers using (a) TD and COT and (b) NB and COT as comonomers. (c) PNB-PA block-like copolymers polymerized with various monomer feed ratios.

UV/Vis spectroscopy also supported the block-like microstructure of the polymers prepared by one-shot copolymerization (Figure 2.5). The PTD-PA block-like copolymer showed almost the same UV/Vis spectrum as that of the PTD-*b*-PA block copolymer (Figure 2.5, a), suggesting that the PTD-PA copolymer was a

near-perfect block-like copolymer as implied by the kinetic studies (Figure 2.2, b and d). However, when the PNB-PA block-like copolymer was prepared at 330 mM, based on the concentration of COT, its spectrum contained some additional signals near 330-390 nm (Figure 2.5, b, black line with a red arrow), which were absent from the spectrum of the PNB-b-PA block copolymer synthesized by sequential monomer addition (Figure 2.5, b, blue line). According to the Fieser-Kuhn rule (Experimental section),⁷ which estimates the λ_{\max} values of oligoenes and the experimental spectra of oligoenes,^{4a} the new signals from the PNB-PA block-like copolymers could be attributed to oligoenes containing five to seven conjugated double bonds (Figure 2.6). This result implies that oligoene domains were inserted into the PNB-rich domain, as indicated by the kinetic analysis (Figure 2.2, a and c).

n	5	6	7	8	9
λ_{\max} (nm)	311.5	340.8	366.7	389.2	408.3

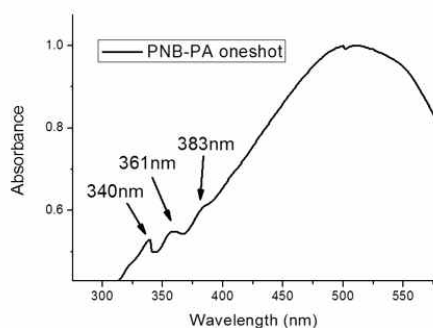


Figure 2.6. The calculated λ_{\max} values of short PA which has the number of double bonds 5-9, by Fieser-Kuhn rule (table). UV/vis absorbance spectrum of PNB-PA one-shot copolymer, synthesized at 330mM using monomer feeding ratio of [NB]:[COT]=50:30 (graph).

Table 2.1. Synthesis of PNB-PA block-like copolymers at different concentrations.

Entry	[NB]:[COT]:[cat]	Conc.(M) ^a	Reaction time (h)	COT conv. (%) ^b	PhH (%) ^{b,c}	Yield (%)
1	50:30:1	0.14	7	>99	19	92
2	50:30:1	0.33	6.5	>99	13	92

^aBased on [COT]. ^bMeasured by ¹H NMR. ^cYield of benzene formation calculated on the basis of the total number of double bonds from converted COTs.

To achieve more block-like microstructures via the ROMP of NB and COT by the one-shot method, the polymerization was conducted at a lower concentration, specifically 140 mM based on the concentration of COT. As expected, the absorption signals of the oligoenes almost disappeared from the UV/Vis spectrum (Figure 2.5, b, red line), indicating that the resulting copolymers contained less oligoene defects in the PNB-rich domain. Therefore, more block-like structures were produced at a lower concentration than at higher concentrations. Presumably, copolymerization at the lower concentration increased the benzene generation as a result of back-biting, thereby shortening the length of the oligoene defects on the shell block. More amount of benzene generated at the lower concentration, as observed by ¹H NMR, supports this assumption (Table 2.1). Alternatively, the lower concentration could favor the ROMP of NB over COT because the ring-opening of COT is reversible process due to its low ring strain. Additionally, we observed that the amount of inserted oligoenes increased with higher feed ratios of COT. The UV/Vis spectrum of the copolymer with the feed ratio of [NB]:[COT] = 50:50 had stronger signals attributed to the oligoenes, even though the polymerization was

carried out at 140 mM based on [COT] (Figure 2.5, c, green line with a red arrow). However, the signals corresponding to the oligoenes disappeared from the spectra of the copolymers with COT feed ratios lower than 30 (Figure 2.5, c).

The effects of the comonomers and synthetic conditions on the block-like microstructures were further investigated by liquid ^1H NMR spectroscopy. Our previous results regarding INCP revealed that the NMR signals for the second insoluble polymer blocks were undetectable by liquid NMR, owing to the core-shell formation of the block copolymers via INCP.³ For example, peaks corresponding to the conjugated PAs, whose chemical shifts ranged from 6 to 7 ppm, were absent from the spectra of the PNB-*b*-PA and the PTD-*b*-PA block copolymers. Upon comparison of the NMR spectra of the conventional block copolymers with the spectra of the block-like copolymers synthesized by the one-shot method, the PTD-PA block-like copolymers showed a ^1H spectrum identical to that of the authentic PTD-*b*-PA block copolymers (Figure 2.7, a). This further supported the near-perfect block microstructure of the PTD-PA copolymer prepared by the one-shot approach. In addition, the PNB-PA block-like copolymer with a lower feed ratio (50:20) exhibited a spectrum almost identical to that of the independently prepared block copolymer (Figure 2.7, b). On the other hand, as the feed ratio of COT increased to 50, the spectrum of the PNB-PA block-like copolymer showed weak but stronger oligoene signals in the range of $\delta = 6\text{-}7$ ppm (Figure 2.7, b). These more oligoene signals suggested the presence of short PA defects on the PNB-rich domain, because the well-solvated PNB-rich shell could be detected by liquid NMR, whereas most long PAs forming the core were not detected. In short, the NMR results supported the conclusions obtained by kinetic and UV/Vis analyses (Figure 2.2, a,c and 2.5, c).

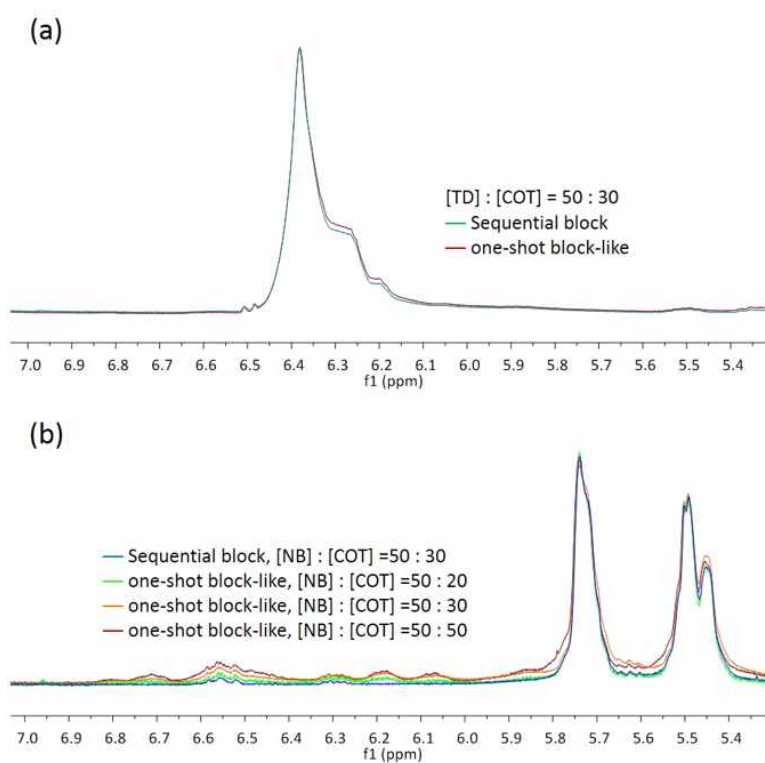


Figure 2.7. Overlays of ^1H NMR spectrum with olefinic regions of (a) PTD-*b*-PA block copolymer and PTD-PA block-like copolymer, and (b) PNB-*b*-PA block copolymer and PNB-PA block-like copolymer prepared with different feed ratio of COT.

2.3.2. One-Shot *in situ* nanoparticlization: Effect of the 1st block on nanostructures

Table 2.2. Synthesis of PNB-PA and PTD-PA block-like copolymers with various feed ratios of COT.

Entry	Comonomer ^a	COT (eq.)	Conc.(M) ^b	Reaction time (h)	COT conv. (%) ^c	PhH (%) ^{c,d}	Yield (%)	D _h (nm) ^e
1	NB	10	0.14	2	>99	22	97	37.8
2	NB	20	0.14	3	>99	22	94	50.8
3	NB	30	0.14	7	>99	19	92	106
4	NB	50	0.14	5.5	86	15	87	122
5	TD	10	0.14	5	66	8	63	83.6
6	TD	20	0.14	9	88	24	95	295
7	TD	30	0.14	13	>99	19	97	576
8	TD	30	0.33	13	96	18	96	625
9	TD	50	0.14	13	95	23	91	2,670

^ause 50 eq. ^bBased on [COT]. ^cMeasured by ¹H NMR. ^dYield of benzene formation calculated on the basis of the total number of double bonds from converted COTs. ^eMeasured by DLS.

To verify formation of nanostructures during one-shot synthesis of block-like copolymers containing insoluble PA as the 2nd block, we synthesized various copolymers using one-shot ROMP. Using 50 equivalents of NB and TD, we varied the feed ratio of COT (Table 2.2) to determine whether a similar structural evolution from 0D micelles to 1D nanocaterpillars from PNB-*b*-PA^{3a} and from 0D micelles to 3D nano and microaggregates from PTD-*b*-PA^{3b} would be possible via one-shot INCP. In all cases, soluble polymers were isolated in high yields after simple precipitation in methanol. The resulting polymers were analyzed by AFM and DLS (Figure 2.8-10); both techniques

confirmed that regardless of the synthetic method, the copolymers synthesized by the one-shot method behaved like the block copolymers synthesized by the sequential addition method. AFM clearly showed the formation of nanospheres and 1D undulated nanocaterpillars from PNB-PA (Figure 2.8, a-e). Moreover, the formation of 3D nanoaggregates from PTD-PA copolymers was visualized by AFM and their sizes increased with increasing feed ratios of COT (Figure 2.9, a-e). The resulting nanostructures from PNB-PA and PTD-PA copolymers showed the same structural evolution as those from the authentic block copolymers (Figure 2.8, f and 2.9, f).³ Furthermore, DLS analysis of the nanostructures synthesized by the one-shot method revealed that the average hydrodynamic diameter (D_h) of nanostructures for both PNB-PA and PTD-PA in chloroform increased with increasing feed ratios of COT (Table 2.2 and Figure 2.10). Additionally, the measured data matched well with the sizes of the nanostructures observed in the AFM images (Figure 2.8-9), and also with the increase of D_h in the previous nanostructures formed by block copolymers synthesized by sequential monomer addition.³ These macroscopic analysis suggested that the newly synthesized copolymers produced by one-shot copolymerization had block-like microstructures, which were similar to those of conventional block copolymers produced by the sequential method.

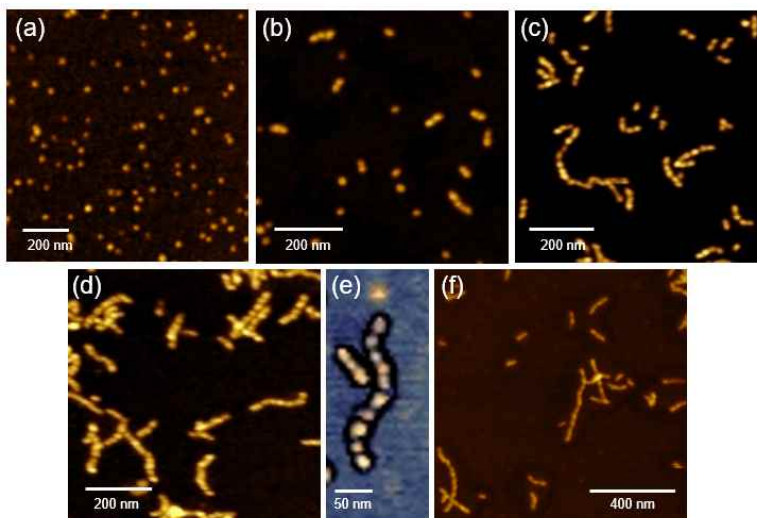


Figure 2.8. AFM height images of nanostructures from the PNB-PA block-like copolymers prepared by monomer ratios $[NB]:[COT] =$ (a) 50:10, (b) 50:20, (c) 50:30, and (d) 50:50 and (e) phase image of $[NB]:[COT] = 50:30$. (f) Comparison to the AFM height image of nanostructures from the PNB-b-PA block copolymer of $[NB]:[COT] = 50:30$.^{3a}

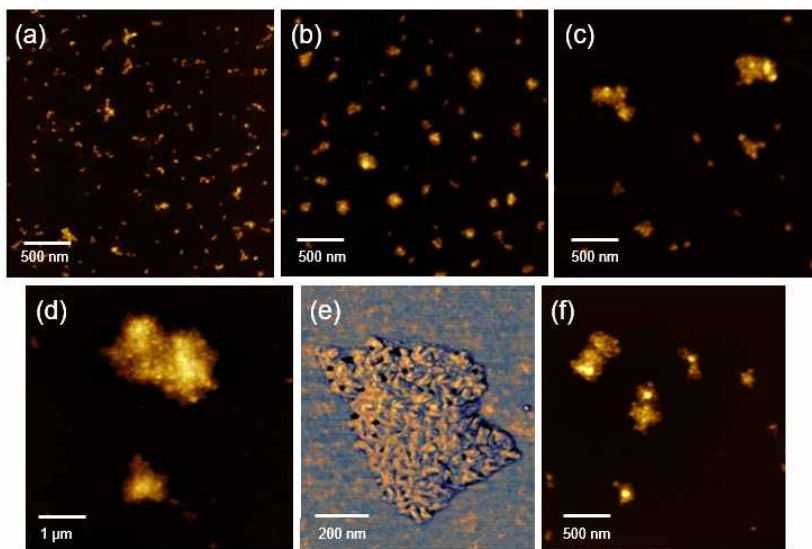


Figure 2.9. AFM height images from PTD-PA block-like copolymers prepared by monomer ratio $[TD]:[COT] =$ (a) 50:10, (b) 50:20, (c) 50:30, and (d) 50:50, and (e) phase image of $[TD]:[COT] =$ 50:30. (f) Comparison to the AFM height image of nanostructures from PTD-b-PA block copolymer of $[TD]:[COT] =$ 50:30.^{3b}

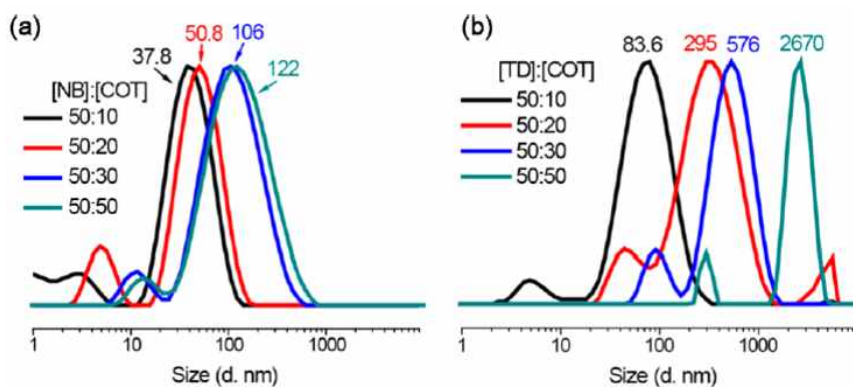


Figure 2.10. DLS profiles of nanostructures formed from (a) PNB-PA and (b) PTD-PA block-like copolymers with various COT ratios.

We revealed that the PNB-PA block-like copolymers had the gradient composition by polymerization kinetics and various analysis. This phenomenon could slightly shorten the length of the second PA block when compared to the PNB-*b*-PA block copolymer. To observe the influence of the shorter length of PA block on the resulting nanostructures, we compared the self-assembly structures composed of the PNB-PA block-like copolymers to those composed of the PNB-*b*-PA block copolymers. The structural distribution was estimated by calculating the ratio of the populations of the wormlike and spherical micelles. The number of worm and micelle structures composed of PNB-PA block-like copolymers with monomer feed ratio [NB]:[COT] = 50:30 was counted in two AFM images with 2 μm x 2 μm size (Figure S2.1). As a result, the number of worm was 90 and 89 and the number of sphere was 30 and 49 for each images. So the calculated worm/sphere ratio was, worm/sphere = 179/79 = 2.3. The worm/sphere ratio of the PNB-*b*-PA block copolymer with same monomer feed ratio was 2.6,^{3a} so the PNB-PA block-like copolymer had slightly more sphere structures. Thus, influence to the resulting nanostructure formation was not that significant.

During the in situ monitoring of the one-shot copolymerization using ^1H NMR, we observed an interesting reduction in the integration of the polymer signals for both PNB-PA and PTD-PA block-like copolymers (Figure 2.11-12). As the polymerization proceeded, the intensity of the exposed PA signals at $\delta = 6-7$ ppm decreased gradually. More surprisingly, not only did the intensity of the PA signals decrease, but those of the PNB or PTD olefin signals ($\delta = 5.7$ and 5.5 ppm for PNB and 6.35 ppm for PTD) decreased as well (Figure 2.11-12, a). The plot of the relative integration changes in the polymer signals vs. time showed these changes more clearly (Figure

2.11-12, b).

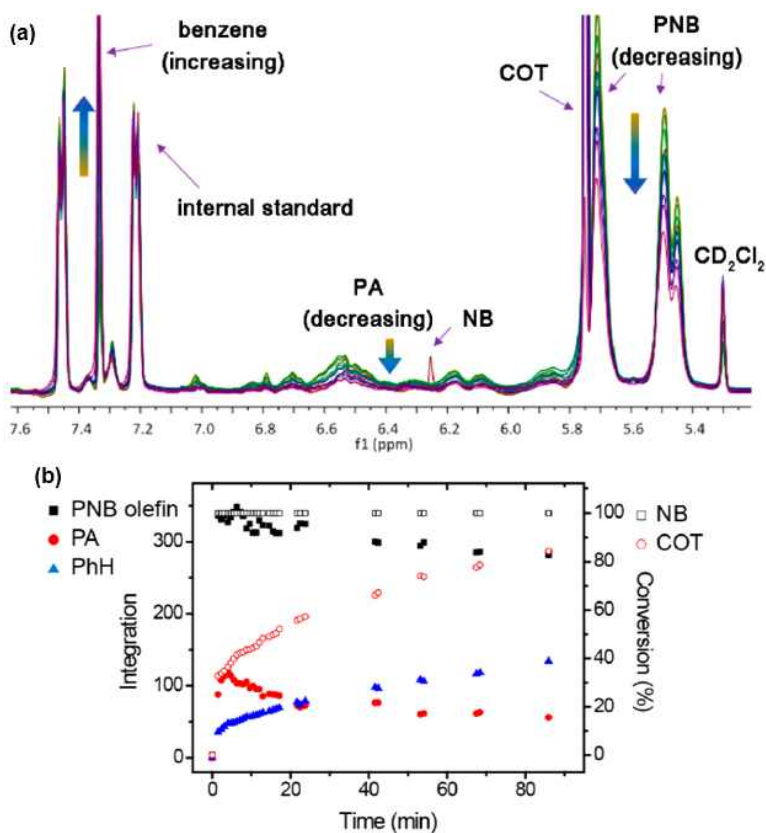


Figure 2.11. In situ monitoring of changes in ^1H NMR integration of block-like copolymers. The copolymerization was conducted at 140 mM based on the concentration of COT at room temperature. (a) Overlay of in situ ^1H NMR spectra of PNB-PA block-like copolymer over time. (b) Integration vs. time plot for PNB, PA, and benzene signals and conversion vs. time plot for each monomer.

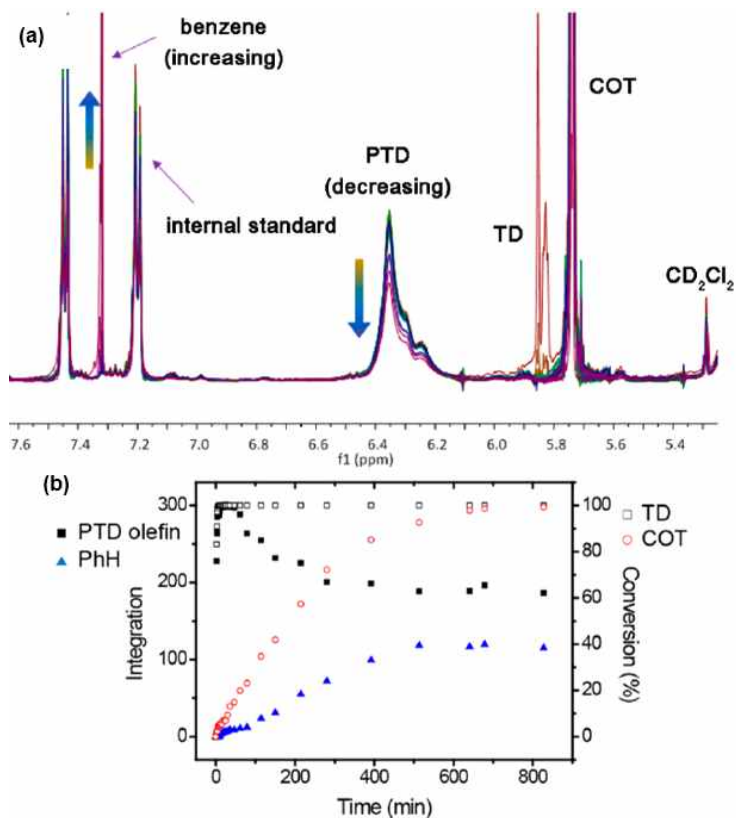


Figure 2.12. In situ monitoring of changes in ^1H NMR integration of block-like copolymers. The copolymerization was conducted at 140 mM based on the concentration of COT at room temperature. (a) Overlay of in situ ^1H NMR spectrum and (b) integration and conversion vs. time plot for PTD-PA block-like copolymer.

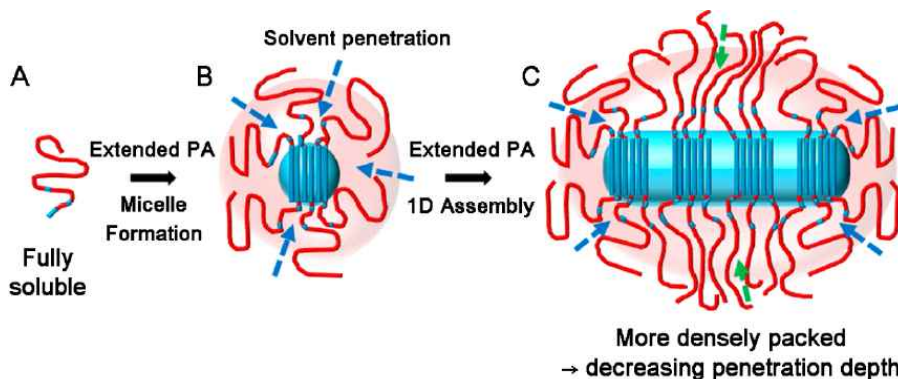
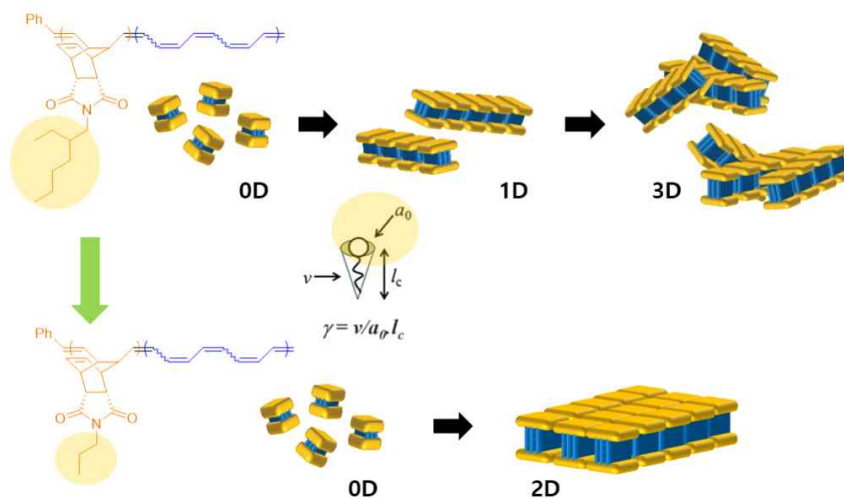


Figure 2.13. Schematic illustration of the nanostructure formation and solvent penetration into the micelles.

We believe that these phenomena may give further insight to the INCP process. First, in the case of the PNB-PA block-like copolymerization, every part of the polymer chain, including the oligoenes, can be detected by liquid NMR during the early stage of the polymerization, because the PNB chain with very short PAs is fully solvated (A in Figure 2.13). As the ROMP of COT proceeds to form elongated solvophobic PA, the polymer chains self-assemble into spherical micelles, so that the soluble PNB shell covers the insoluble PA core and the intensity of the signal attributed to PA decreases (B in Figure 2.13). During this process, a small part of the PNB-rich domain near the PA core may be buried together with the PA core, resulting in a reduction in the integration of the signals corresponding to PNB. With the further elongation of the PA core, the spherical micelle structure is not sufficient to cover the extended PA core, and the micelles spontaneously cling to each other to form 1D nanocaterpillar structures.^{3a} This process leads to tightening of the shell as the polymer chains condense, and more of the chains near the core become less mobile (C in Figure 2.13). Thus, the signal intensity of

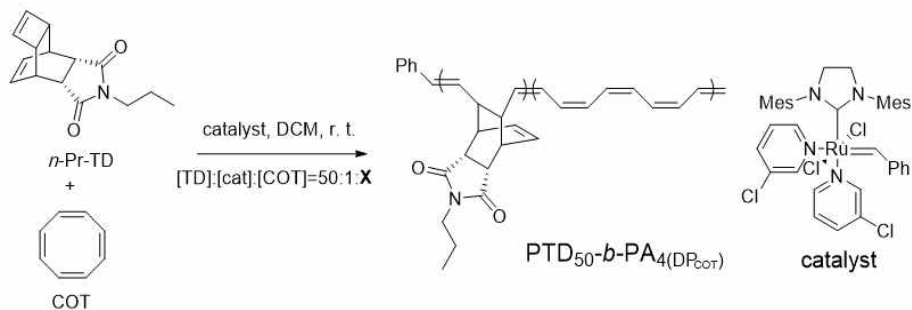
the polymers decreases because this tightly packed or hardly solvated corona takes a solid-like state, similar to the PA core and it becomes harder for NMR solvents to penetrate deep into the shell (Figure 2.13, green arrows).⁸ Secondly, a larger decrease in the PTD intensity was observed during the one-shot polymerization of TD and COT (Figure 2.11-12, b). This was because the PTD-PA block-like copolymer self-assembled into 3D-aggregates, or higher dimensional nanostructures with denser packing than the 1D assembly of PNB-PA.^{3b} Therefore, a larger portion of the PTD shell becomes concealed and undetectable by ¹H NMR. In short, the changes in the NMR intensities during polymerization may indirectly shed light on how various INCP processes actually occur in solution.



Scheme 2.2. Proposed design to prepare two-dimensional sheet-like structures by decreasing size of solubilizing substituent on the 1st block to increase core-core interaction during INCP process.

Even though more rigid PTD block leads to formation of higher dimensional structures with more core-core interaction than the nanostructures generated from BCPs containing flexible PNB block, the building blocks of three-dimensional nanostructures, nanocaterpillars, were attached without controlled directionality, leading to irregular structures. If we control the stacking of building blocks in the same direction, more well-defined structures such as two-dimensional sheet-like structures can be prepared. We assumed that two-dimensional interaction between spherical micelles should be easier than the parallel interaction between nanocaterpillars without defect (Scheme 2.2). To achieve direct growth of sheet-like structures from spherical micelles, we decreased size of solubilizing substituent of rigid PTD block from ethylhexyl group to *n*-propyl group to decrease shielding of a core by shell and then increase core-core interaction.

Table 2.3. Synthesis of PTD-PA block-like copolymers containing smaller *n*-propyl groups on the 1st block.



Entry	[TD]:[COT]:[cat]	Conc.(M) ^a	Reaction time (h)	COT conv. (%) ^b	PhH (%) ^{b,c}	DP _{COT}	Yield (%)	D _h (nm) ^d
1	50:20:1	0.14	4	23	24	3	81	95
2	50:20:1	0.14	4.5	46	20	7	85	600
3	50:20:1	0.14	5	69	33	9	88	700

^aBased on [COT]. ^bMeasured by ¹H NMR. ^cYield of benzene formation calculated on the basis of the total number of double bonds from converted COTs. ^dMeasured by DLS.

PTD-PA block-like copolymers containing smaller *n*-propyl substituent on the 1st block were synthesized by one-shot ROMP (Table 2.3). Using 50 equivalents of *n*-Pr-TD and 20 equivalents of COT, we varied the polymerization time from 4 hours to 4.5 and 5 hours to prepare block-like copolymers with slightly different DP of PA block because the nanostructures could be evolved more sensitively by expanding cores with the shell having poor solubilizing ability.^{3b} The resulting polymers showed structural growth from spherical micelles and their small aggregates to sheet-like structures and then three-dimensional aggregates from AFM images (Figure 2.14, a-c). As expected, smaller solubilizing substituent led to self-assembly of block copolymers with very short PA block as DP 3, and the spherical micelles interconnected

each other in two-dimensional directions directly without forming nanocaterpillar structures (Figure 2.14, a). TEM image of PTD-PA having block ratio of 50:7 exhibited sheet-like structures composed of individual spherical micelles (Figure 2.14, d). To confirm that the sheet-like structures were stable in solution, not generated by drying process during sample preparation, cryo-TEM imaging and DLS measurement of chloroform solution were carried out. Similar assembled structures with low electron density due to monolayered micelles were observed from cryo-TEM images (Figure 2.14, e). Furthermore, DLS analysis showed increasing D_h of nanostructures for PTD-PA in chloroform with increasing DP of PA, which was roughly matched with the size of nanostructures observed from dry images (Figure 2.14, f). This analysis supported that the two-dimensional sheet-like structures assembled from spherical micelles were prepared successfully in solution during simple one-shot synthesis of PTD-PA block-like copolymers.

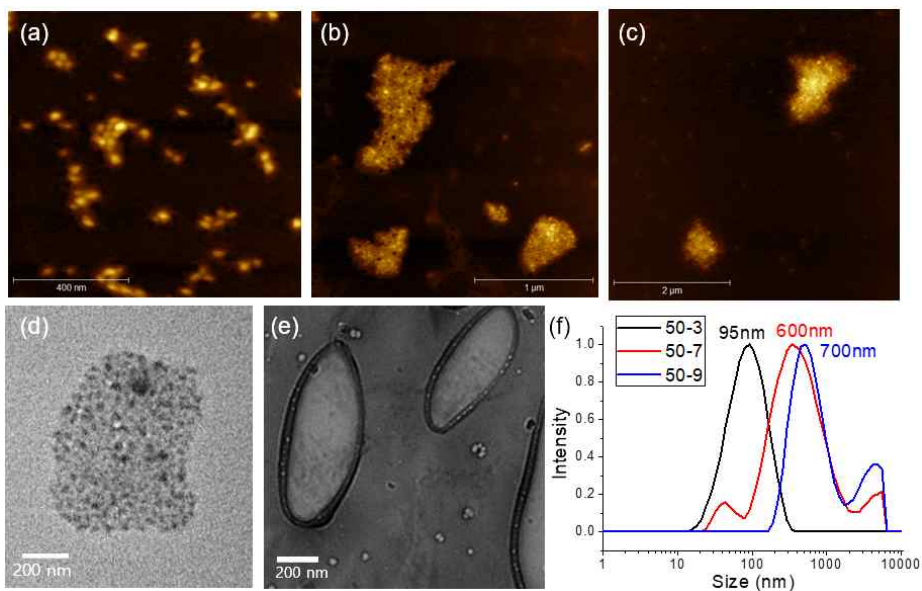


Figure 2.14. AFM height images from PTD-PA block-like copolymers with *n*-propyl substituent on PTD with the block ratio of (a) 50:3, (b) 50:7, and (c) 50:9. (d) A TEM image and (e) a cryo-TEM image of PTD-PA with *n*-propyl substituent on PTD having the block ratio of 50:7. (f) DLS profiles of PTD-PA with *n*-propyl substituent on PTD having different block ratios in chloroform at 0.1 mg/ml.

2.4. Conclusion

Various nanostructures could be successfully prepared via simple one-step procedure by achieving one-shot synthesis of block-like copolymers containing insoluble PA block which can be spontaneously self-assembled during the polymerization. The different reactivities of the comonomers, NB or TD and COT enabled sequential ROMP in the mixture solution to produce block-like copolymers. The nanostructures formed from the block-like microstructures of the copolymers were essentially the same as those obtained from the block copolymers synthesized by sequential monomer addition. Notably, introducing PTD as the 1st block could produce near-perfect, block-like PTD-PA by the one-shot ROMP due to more favorable reactivity toward the Grubbs catalyst. Moreover, modulating the rigidity and solubility of the 1st block by using PNB and PTD with different substituents enabled preparation of different kinds of nanostructures such as one-dimensional nanocaterpillars, three-dimensional nanoaggregates, and also two-dimensional sheet-like structures.

2.5. Experimental section

Characterization

NMR spectra were recorded by Varian/Oxford As-500 (500 MHz for ^1H /125 MHz for ^{13}C) spectrometer. 4,4-Dimethylbiphenyl was used as an internal standard for ^1H NMR analysis. UV/vis spectra were obtained by a Jasco Inc. UV/vis spectrometer V-630, and dynamic light scattering (DLS) data were obtained by a Malvern Zetasizer Nano ZS. Multimode 8 and Nanoscope V controller (Veeco Instrument) were used for AFM imaging. All images were obtained on tapping mode using noncontact mode tip from Nanoworld (Pointprobe tip, NCHR type) with spring constant of 42 N m⁻¹ and tip radius of ≤ 8 nm.

Materials

All reagents were commercially available from Acros, Alfa, Sigma Aldrich and TCI and used without further purification unless specified otherwise. All anhydrous deuterium solvents ($\geq 99.95\%$) were purchased from Euriso-Top[®] and were used degassed for 10 mins before polymerization. The third generation Grubbs catalyst was prepared by the reported method.⁹

Synthesis of monomers

Both monomers, NB and TD, were prepared by the method from the previous literatures.^{3,10}

N-cyclohexyl-exo-norbornene-5,6-dicarboximide (NB monomer)

^1H NMR (500 MHz, CDCl_3) : δ 6.27 (t, 2H), 3.91-3.40 (m, 1H), 3.25 (d, 2H), 2.60 (d, 2H), 2.09-2.18 (m, 2H), 1.25-1.85 (m, 10H). ^{13}C NMR (125 MHz, CDCl_3) : δ 178.4, 138.1, 51.8, 47.6, 45.4, 42.7, 29.0, 26.0, 25.2

7,8-N-(2-ethylhexyl)succinimide-endo-tricyclo[4.2.2.02.5]deca-3,9-diene (TD monomer)

^1H NMR (500 MHz, CDCl_3): δ 0.86-0.89 (m, 6 H), 1.20-1.26 (m, 8 H), 1.65 (s, 1 H), 2.77 (s, 2 H), 2.82 (s, 2 H), 3.17 (s, 2 H), 3.30 (d, 2 H), 5.90 (m, 4 H); ^{13}C NMR (125 MHz, CDCl_3): δ 179.18, 138.10, 128.48, 44.36, 43.36, 42.55, 37.64, 36.83, 30.46, 28.59, 23.82, 23.13, 14.21, 10.45.

General procedure for the one-shot synthesis of block-like copolymers

Both comonomers (0.063 mmol for NB or TD and 0.013.0.063 mmol for cyclooctatetraene (COT)) were weighed in a 2 mL sized screw-cap vial with septum and purged with argon. Anhydrous and degassed dichloromethane was added (0.06.0.42 mL) to the vial. The solution of the third-generation Grubbs catalyst (1.0 mg, 0.0013 mmol) was added (0.03 mL) to the monomer solution at once under vigorous stirring, and the vial was tightly sealed by using parafilm and Teflon tape. The mixture was stirred for 2.13 h at the room temperature. The reaction was quenched by excess ethyl vinyl ether. The crude mixture was precipitated into methanol, and the obtained dark powder was dried in vacuo.

Poly(NB)-PA block-like copolymers

Yield: 87.97% (see Table 2.1 and 2.2, entries 1-4). ^1H NMR (500 MHz, CDCl_3): δ 6.08.6.82 (m), 5.76 (s, 1H), 5.45.5.50 (d, 1H), 3.88 (s, 1H), 3.28.2.67 (m, 4H), 2.16 (m, 3H), 1.81 (s, 2H), 1.65.1.55 (m, 4H), 1.30.1.20 (m, 3H). ^{13}C NMR (125 MHz, CDCl_3): δ 178.5, 132.1, 52.6, 51.5, 50.9, 46.7.46.2, 43.0. 41.0, 29.0, 26.1, 25.3 (all the PNB-PA one-shot copolymers have identical ^1H NMR and ^{13}C NMR spectra, except the intensity of δ 6.08.6.82 signal at ^1H NMR).

Poly(TD)-PA block-like copolymers

Yield: 63.95% (see Table 2.2, entries 5-9). ^1H NMR (500 MHz, CDCl_3): δ 6.32 (s, ^1H), 5.09 (s, 1H), 3.20.2.70 (br, 7H), 1.68 (s, 1H), 1.59 (s, 1H), 1.25.1.16 (br, 8H) 1.00.0.81 (br, 6H). ^{13}C NMR (125 MHz, CDCl_3): δ 178.7, 132.4, 131.3 44.0 (br), 42.7, 40.8, 38.6 (br), 37.5, 30.6, 28.7, 23.7, 23.3, 14.3, 10.4 (all the PTD-PA one-shot copolymers have identical ^1H NMR and ^{13}C NMR).

^1H NMR analysis for COT conversion and benzene formation

COT conversion was calculated from the final COT/(internal standard) ratio divided by initial COT/(internal standard) ratio. Also, benzene formation (%) was calculated from the number of double bonds to form benzene divided by the number of total double bonds theoretically attached to the polymer. (Chemical shift - 4,4-dimethylbiphenyl : δ 2.37, δ 7.22, δ 7.46, CH of COT : δ 5.76, CH of Benzene : δ 7.36)

***In situ* ^1H NMR analysis for monitoring consumption of comonomers**

Both comonomers (0.094 mmol for NB or TD, and 0.057 mmol for COT) and 4,4-dimethylbiphenyl (~3 mg, an internal standard) were added into screw-cap NMR tube and purged with argon. Anhydrous and degassed CD_2Cl_2 was added (0.37 ml) to the NMR tube and stabilized at appropriate temperature in NMR instrument. Then, the initial ratio between comonomers and the internal standard was measured by ^1H NMR analysis. After that, the solution of the third-generation Grubbs catalyst (1.5 mg, 0.0019 mmol, 0.03 mL) was added and the conversion of the two monomers was monitored with time until the complete consumption of both monomers.

Atomic force microscopy (AFM)

The atomic force microscopy experiments were performed with a thin film prepared by spin-coating one drop of the polymer solution (~ 0.02 mg polymer/mL, CHCl_3 ; spinning rate = 3000 rpm for 30 sec). The solvent was filtered by $0.2\text{-}\mu\text{m}$ PTFE filter before making the solution. The thin films were prepared on mica substrates. All images were obtained on tapping mode using non-contact mode tips from Nanoworld (Pointprobe tip, NCHR type) with spring constant of 42 N m^{-1} and tip radius of $\leq 8\text{ nm}$.

Transmission electron microscopy (TEM)

Dry-TEM and cryo-TEM imaging were performed by JEM-2100 operated at 120 kV and SC 1000 CCD camera (Gatan Inc.). The samples for dry-TEM imaging were prepared by drop casting one drop ($\sim 10\ \mu\text{L}$) of sample solution (0.1 mg/mL) on the carbon-coated copper grid. The cryo-TEM experiments were performed with a thin film of solution ($5\ \mu\text{L}$, 0.1 mg/mL) transferred to a lacey supported grid. The thin solution films were prepared under solvent vapor saturated condition (chloroform) within a custom-built environmental chamber in order to prevent evaporation of solvent from sample solution. The excess liquid was blotted with filter paper for 2-4 seconds, and the thin solution films were rapidly vitrified by plunging them into liquid ethane ($-170\text{ }^\circ\text{C}$) using Gatan CryoplungeTM3 system. The grid was transferred on a Gatan 626 cryoholder, using a cryo-transfer device. After that they were transferred to a JEM-2100. Direct imaging was carried out at a temperature of approximately $-175\text{ }^\circ\text{C}$ and with a 120 kV accelerating voltage.

Dynamic laser light scattering (DLS)

The DLS experiments were performed with polymer-chloroform solution (0.1 mg polymer/mL CHCl₃) in a quartz glass cell (Hellma Analytics).

UV/vis spectroscopy

The UV/vis spectra were obtained from polymer-chloroform solution (0.01-0.1 mg polymer/mL CHCl₃) in a quartz glass cell (Hellma Analytics).

Reactivity ratio calculation

Fineman-Ross plot method⁶ was used for determining reactivity ratios of NB and COT, and TD and COT. The series of monomer mixture with different ratio (70:30, 60:40, 50:50, 40:60, and 30:70) was prepared and the reaction was conducted at 0 °C and terminated at early stage of polymerization (< 20 sec). The conversion of each monomer was observed by ¹H NMR. Fineman-Ross equation was at below.

$$\frac{f(1-F)}{F} = r_2 - r_1\left(\frac{f^2}{F}\right)$$

$f = \frac{M_1}{M_2}$ of feeding ratio, $F = \frac{M_1}{M_2}$ of ratio in polymer

Using this equation, the reactivity ratios of NB and COT were calculated to be $r_1 = 12.6$ (NB) and $r_2 = 0.605$. However, the reactivity ratios of TD and COT could not be estimated because no COT was reacted at early stage of polymerization because of the too large reactivity difference with the TD monomer.

Calculated λ_{\max} values of polyenes

Fieser-Kuhn rule⁷ was used for calculating theoretical λ_{\max} values of inserted short polyenes during one-shot copolymerization of NB and COT:

$$\lambda_{\max} = 114 + 5M + n(48.0 - 1.7n) - 16.5R_{\text{endo}} - 10R_{\text{exo}}$$

where M is the number of alkyl substituents and ring residues in the conjugated system, n is the number of conjugated double bonds, R_{endo} is the number of rings with endocyclic double bonds, and R_{exo} is the number of rings with exocyclic double bonds. For polyacetylene (PA), there is no substituent or ring, so M, R_{endo} , and R_{exo} equals to zero. Then, the λ_{\max} values depending on the number of conjugated double bonds, n, are calculated below in the range of 300-400 nm, in which the absorbance spectra of PNB-PA one shot copolymer have signals (Figure 2.6). Compared the calculated values with experimental values, the calculated values when n is 6, 7, or 8 are similar with the peaks showed at the spectrum of PNB-PA one-shot copolymer. The somewhat difference is assumed that it can be from cis/trans PA structures.

2.6 Supporting information

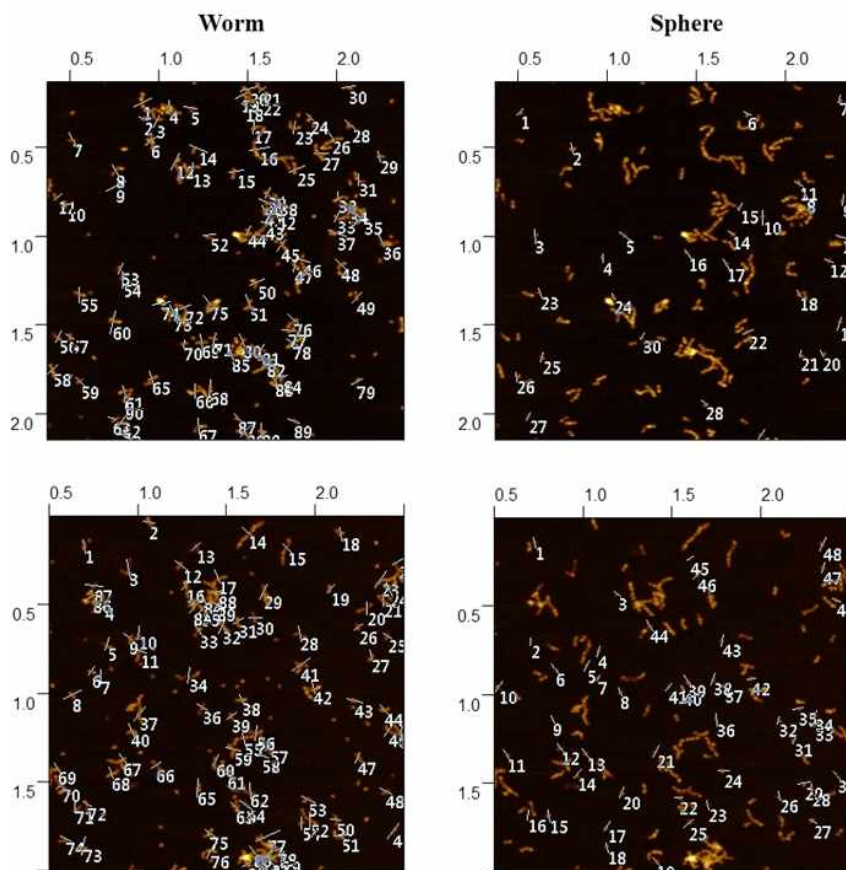


Figure S2.1. Counting the number of the worm-like structures and the spherical structures composed of PNB-PA block-like copolymers in two different AFM images.

2.7. References

[†]Portions of this chapter have been previously reported, see: Shin, S.; Yoon, K.-Y.; Choi, T.-L. *Macromolecules* **2015**, *48*, 1390.

(1) (a) Shirakawa, H. *Angew. Chem., Int. Ed.* **2001**, *40*, 2574. (b) Etemad, S.; Heeger, A. *Annu. Rev. Phys. Chem.* **1982**, *33*, 443.

- (2) (a) Gorman, C. B.; Ginsburg, E. J.; Grubbs, R. H. *J. Am. Chem. Soc.* **1993**, *115*, 1397. (b) Wu, C.; Niu, A.; Leung, L. M.; Lam, T. *J. Am. Chem. Soc.* **1999**, *121*, 1954. (c) Scherman, O. A.; Rutenberg, I. M.; Grubbs, R. H. *J. Am. Chem. Soc.* **2003**, *125*, 8515.
- (3) (a) Yoon, K.-Y.; Lee, I.-H.; Kim, K. O.; Jang, J.; Lee, E.; Choi, T.-L. *J. Am. Chem. Soc.* **2012**, *134*, 14291. (b) Yoon, K. Y.; Shin, S.; Kim, Y. J.; Kim, I.; Lee, E.; Choi, T. L. *Macromol. Rapid Commun.* **2015**, *36*, 1069.
- (4) (a) Scherman, O. A.; Grubbs, R. H. *Synth. Met.* **2001**, *124*, 431. (b) Khoury, P. R.; Goddard, J. D.; Tam, W. *Tetrahedron* **2004**, *60*, 8103.
- (5) Kim, K. O.; Shin, S.; Kim, J.; Choi, T.-L. *Macromolecules* **2014**, *47*, 1351.
- (6) (a) Kelen, T.; Tu.do.s, F. J. *Macromol. Sci., Chem.* **1975**, *A9*, 1. (b) Tidwell, P. W.; Mortimer, G. A. *J. Polym. Sci., Part A* **1965**, *3*, 369. (c) Shin, E. J.; Brown, H. A.; Gonzalez, S.; Jeong, W. H.; Hedrick, J. L.; Waymouth, R. M. *Angew. Chem., Int. Ed.* **2011**, *50*, 6388.
- (7) Gebhard, R.; van Dijk, J. T. M.; van Ouwkerk, E.; Boza, M. V. T. J.; Lugtenburg, J. *Recl. Trav. Chim. Pays-Bas* **2010**, *110*, 459.
- (8) (a) Kwon, G.; Naito, M.; Yokoyama, M.; Okano, T.; Sakurai, Y.; Kataoka, K. *Langmuir* **1993**, *9*, 945. (b) Bu.tu.n, V.; Wang, X.-S.; de Paz Ba.n.ez, M. V.; Robinson, K. L.; Billingham, N. C.; Armes, S. P. *Macromolecules* **2000**, *33*, 1.
- (9) Kang, E.-H.; Lee, I. S.; Choi, T.-L. *J. Am. Chem. Soc.* **2011**, *133*, 11904.
- (10) Kim, K. O.; Choi, T.-L. *Macromolecules* **2013**, *46*, 5905.

Chapter 3.

One-shot *in situ* nanoparticlization of Poly(*para*-phenylenevinylene) block copolymers

3.1. Abstract

One-shot synthesis of poly(*para*-phenylenevinylene) (PPV) block copolymers via ROMP of [2.2]paracyclophane-1,9-diene (PCPDE) successfully produced fluorescent nanostructures during polymerization. Sterically demanding PCPDE reacted much slower than monomers for solubilizing blocks, norbornene (NB) and *endo*-tricyclo[4.2.2.0]deca-3,9-diene (TD) derivatives, and resulted in synthesis of near-perfect block copolymers. Too severe steric hindrance between TD and PCPDE caused uncontrolled polymerization kinetics with extremely slow initiation of the PPV 2nd block, and this polymerization kinetics affected to the kinetics of self-assembly to produce unique fractal structures in solution.

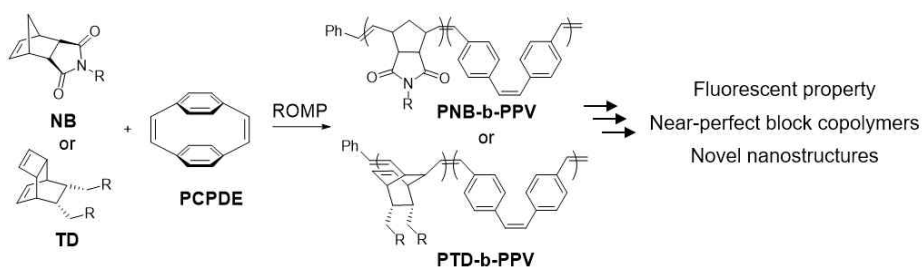
3.2. Introduction

In Chapter 2, a facile method for the preparation of dimensionally controlled nanostructures from polyacetylene (PA) block copolymers (BCPs) using ring-opening metathesis polymerization (ROMP) was developed. The self-assembly occurs concurrently with polymer synthesis due to strong π - π interaction of insoluble PA blocks, and the block copolymers were synthesized by one-shot addition of comonomers having largely different reactivities. However, the intrinsic limitations of PA such as low stability in air and backbiting reaction during synthesis using ROMP hindered useful application of the nanostructures.

Another conjugated polymer which can be a possible candidate for simple preparation of nanostructures by *in situ* nanoparticlization of conjugated polymers (INCP) using ROMP is poly(*para*-phenylenevinylene) (PPV). Various synthetic routes to prepare PPV by ROMP have been developed since 1992.¹ Among them, the most simple and well-defined method is using [2.2]paracyclophane-1,9-diene (PCPDE) and Grubbs catalyst, reported by Turner's group in 2006.^{1c} ROMP using PCPDE produced PPV having *cis-trans* alternating configuration, with relatively low PDI and controlled length in a living manner. The propagation rate of PPV was quite slow because of steric congestion between *ortho* hydrogens of PCPDE and the bulky ligands of the catalyst,² which led us to envision a one-shot block copolymerization with fast reacting norbornene (NB) or *endo*-tricyclo[4.2.2.0]deca-3,9- diene (TD) derivatives. Additionally, PPV is very well-known for its intriguing optoelectronic properties and also has better stability under air, providing possibilities to be applied to various fields such as biotherapy, imaging, and chemical sensors.

In the previous chapter, the influence of the 1st block on nanostructures was demonstrated. The role of the 2nd block composing

core of nanostructures can be observed by introducing another conjugated polymer, PPV, as the 2nd block. Additionally, polymerization conditions can have a critical effect on nanostructures prepared during polymerization. Various studies about the role of concentration of initiator, polymerization temperature, ionic strength, pH as well as the polymerization kinetics in the morphology of nanostructures prepared by polymerization-induced self-assembly (PISA) have been reported.³ However, only the influence of polymerization livingness on the nanostructures prepared by INCP was studied.⁴ In order to obtain more diverse nanostructures, further research on the relationship between morphologies and polymerization conditions or kinetics is required.



Scheme 3.1. one-shot synthesis of PPV block copolymers using NB or TD and PCPDE

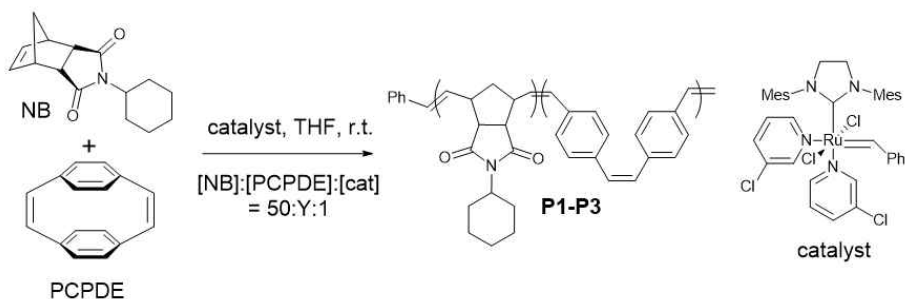
In this chapter, we report the one-shot preparation of fluorescent nanostructures through *in situ* nanoparticlization of PPV block copolymers synthesized by one-shot ROMP using NB or TD derivatives and PCPDE as comonomers (Scheme 3.1). By exploiting a dramatic difference in reactivity of comonomers, block copolymers having near-perfect block microstructures could be synthesized. Simply changing the 2nd block from PA to PPV did not induce different nanostructures due to highly trapped structures without well-defined

interaction such as crystallization. But surprisingly, we revealed that different polymerization kinetics produced different nanostructures by changing kinetics of self-assembly during polymerization, resulting in unique fractal nanostructures composed of PTD-*b*-PPVs. This result strongly supports that the nanostructures were generated during polymerization process, thereby emphasizing the importance of polymerization condition, which equals self-assembly condition of the INCP process, for determining nanostructures.

3.3. Results and discussion

3.3.1. One-shot *in situ* nanoparticlization of PNB-*b*-PPV: Effect of the 2nd block on polymerization kinetics and nanostructures

Table 3.1. Synthesis of PNB-*b*-PPV by one-shot ROMP using NB and PCPDE.



Polymer	[NB]:[PCPDE]:[cat]	Reaction time (h)	PCPDE conv. (%) ^a	Yield (%)	<i>D</i> _h (nm) ^b
P1	50:10:1	4	>99	82	80
P2	50:20:1	8	>99	91	155
P3	50:30:1	12	>99	93	220

^aMeasured by ¹H NMR. ^bMeasured by DLS.

The PPV BCPs were prepared from the living ROMP of two different types of monomers, NB derivatives for the solubilizing first block, and non-substituted PCPDE for the insoluble second block, using the highly active and fast initiating third-generation Grubbs catalyst in tetrahydrofuran (THF) (Table 3.1). Qualitative observations from our previous studies⁵ and those performed by other groups^{1c} indicated that PCPDE derivatives polymerized at a much slower rate (typically requiring overnight reactions, even at elevated temperatures) than NB

derivatives (complete conversion within minutes at room temperature). This led us to envision a one-shot copolymerization wherein all necessary components (monomers, catalyst, and solvent) are introduced simultaneously to prepare BCPs. To quantitatively determine the polymerization rate difference, time-dependent competitive monomer conversion was monitored by ^1H NMR spectroscopy at $0\text{ }^\circ\text{C}$ (Figure 3.1, a and b). As expected, a significant difference was observed in the propagation rates (k_p of NB being about 100 times greater than that of PCPDE), corresponding to the incorporation of a single PCPDE unit for every 48 repeating units of NB, and indicating that the one-shot copolymerization produced well-defined BCP microstructures. The conversion of NB and PCPDE reached 95% and 6%, respectively, within 5 minutes. This represents a significant improvement compared to the one-shot ROMP from mixtures of NB and cyclooctatetraene (COT) reported in Chapter 2, in which 27% conversion of the slow-reacting COT was observed while the conversion of NB reached 95%, yielding tapered copolymer architectures. The corresponding difference in the k_p of NB and COT was 24-fold. Although the ring strain of PCPDE (42 kcal/mol)⁶ is nearly 15 kcal/mol higher than that of NB (27 kcal/mol),⁸ k_p of PCPDE is significantly smaller because of the large steric hindrance of the phenyl rings that retard the approach of the catalyst (Figure 3.2).²

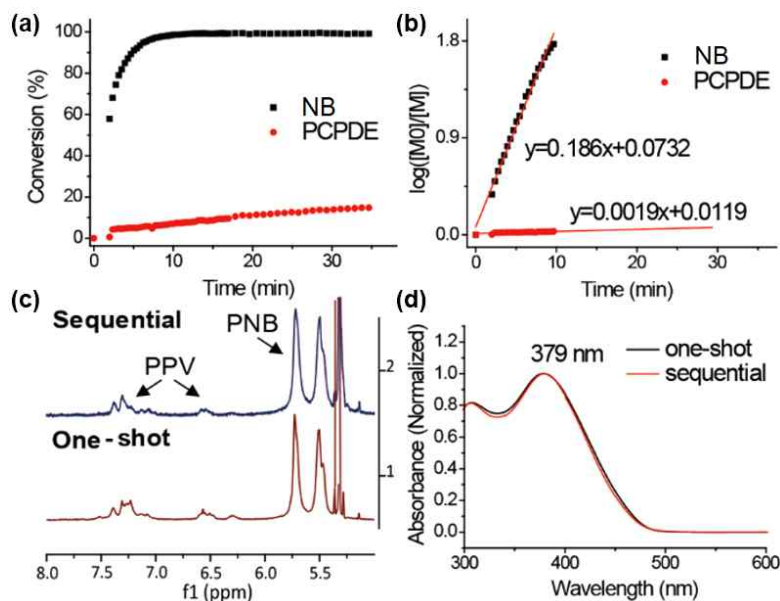


Figure 3.1. One-shot copolymerization of PNB-*b*-PPV. Conversion vs. time (a) and logarithmic conversion vs. time (b) plots for one-shot ROMP of NB and PCPDE at 0 °C with a feed ratio [NB]:[PCPDE]= 50:20 at 0.1 M based on the concentration of PCPDE. ¹H NMR spectra (500 MHz, CD₂Cl₂) (c) and UV/Vis absorbance spectra (d, 0.05 mg/mL, normalized) of PNB-*b*-PPV synthesized by conventional sequential monomer addition and **P2** synthesized by one-shot ROMP.

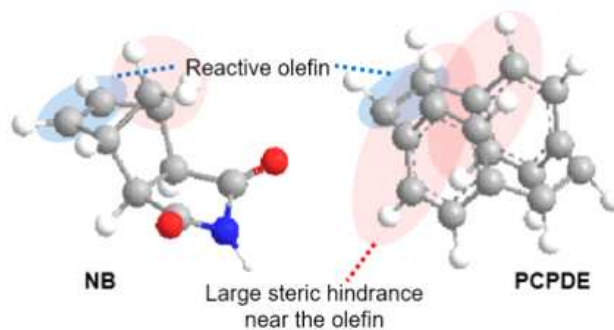


Figure 3.2. Comparison between the steric hindrance near the reactive olefin of NB and PCPDE monomers.

To verify the similarities between the microstructures of the PPV BCPs obtained from the conventional sequential monomer addition and from the one-shot copolymerization, their ^1H NMR and UV/Vis absorbance spectra were compared (Figure 3.1, c and d). The nearly identical ^1H NMR and UV/Vis absorbance spectra indicated that the blocky microstructure and the degree of conjugation of the PPV block were essentially the same, respectively, regardless of the synthetic procedure. Additionally, the PPV resonances were nearly absent in the ^1H NMR spectra of both BCPs, suggesting the successful in situ formation of a core-shell structure with insoluble PPV cores from the polymerization (Figure 3.1, c).

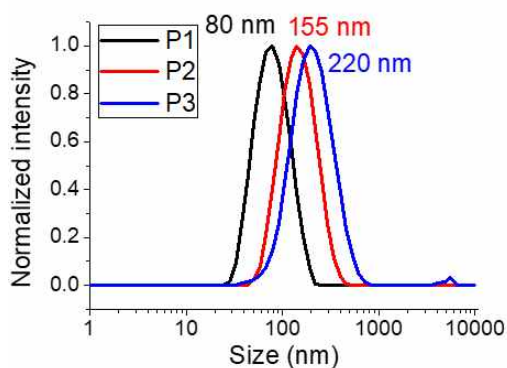


Figure 3.3. DLS profiles of **P1-P3** in chloroform with a polymer concentration of 0.1 mg/mL

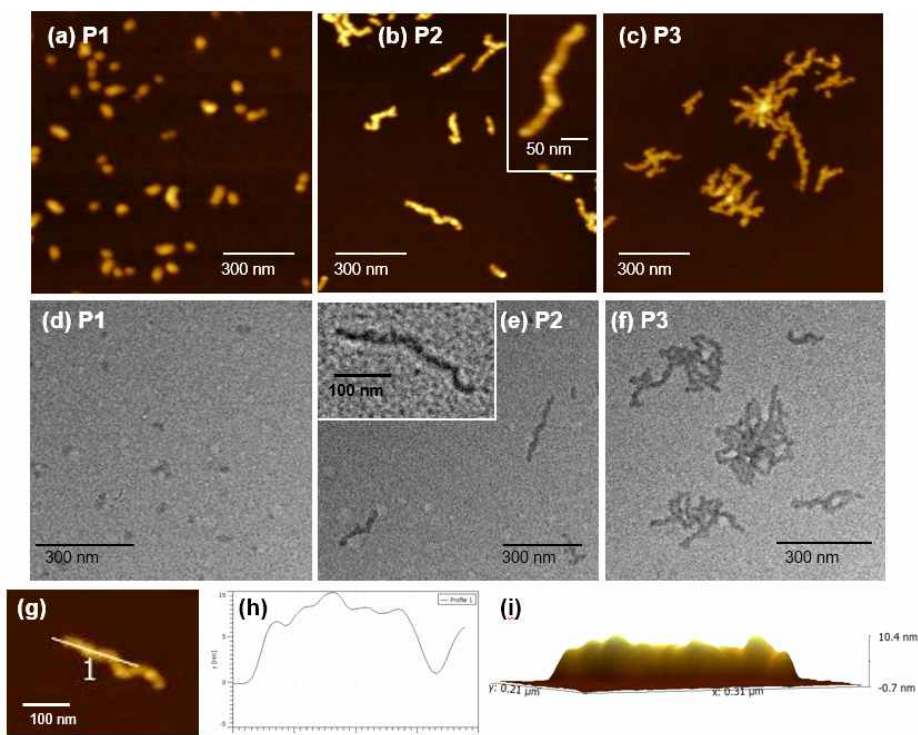


Figure 3.4. AFM images (a-c) and TEM images (d-f) of nanostructures of BCPs prepared from chloroform solutions of **P1-P3**, respectively. (g) AFM topography, (h) height profile, and (i) 3D projection image of **P2**, indicating undulated nanocaterpillar structure.

Polymers with various feed ratios were easily prepared using this simple, one-shot block copolymerization (Table 3.1) and analyzed by dynamic light scattering (DLS), atomic force microscopy (AFM), and transmission electron microscopy (TEM). The DLS analysis of **P1-P3** in chloroform without any post-synthetic treatment showed increasing hydrodynamic diameters (D_h) from 80 nm to 220 nm with increasing feed ratio of PCPDE from 10 to 30 (Figure 3.3), suggesting direct self-assembly during the one-shot copolymerization. The AFM and TEM images of **P1-P3** clearly show the evolution of nanostructures

from spheres to rods by one-dimensional (1D) growth (with a maximum length of 300 nm) and then to multi-armed star-like micelles (Figure 3.4). Unlike typical worm-like BCP micelles, these nanocaterpillars and star-like structures showed undulating height profiles by AFM and loosely associated cores as observed by TEM. These observations suggest the formation of caterpillar-like structures, similar to those observed from PA BCPs in Chapter 2 (Figure 3.4, inset images of b and e, and g-i).⁴ Additionally, the size of the nanostructures measured from the AFM and TEM images was roughly consistent with their D_h from DLS, indicating that the nanostructures were preserved in solution. The samples taken during polymerization without quenching and precipitation processes also showed same morphological evolution with **P1-P3**, supporting *in situ* formation of nanostructures without any post-synthetic treatments (Figure S3.1).

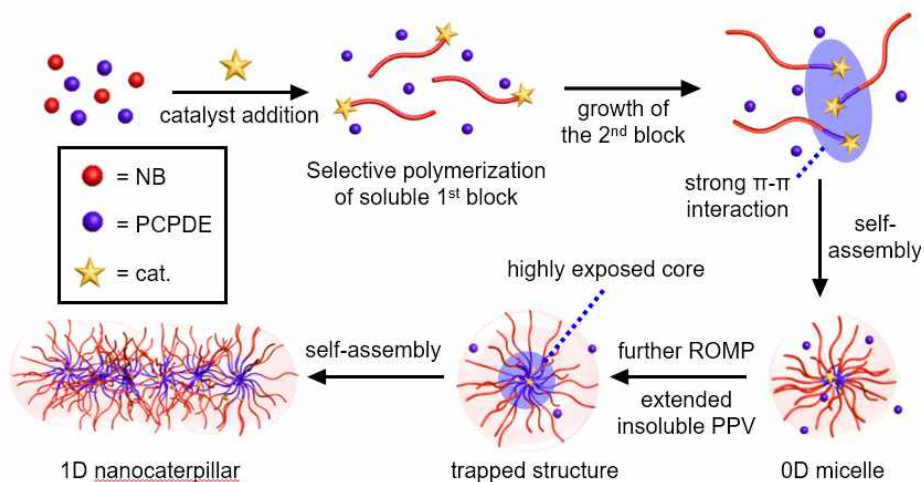


Figure 3.5. Proposed mechanism of stable PNB-*b*-PPV nanoparticle formation via one-shot INCP.

The mechanism of in situ self-assembly during the one-shot copolymerization is proposed as follows (Figure 3.5).⁴ After the rapid ROMP of the norbornene derivatives, the ROMP of PCPDE proceeds to give the insoluble PPV second block, which immediately forms nanospheres through strong π - π interactions. The propagating carbenes remain active in the cores, and the diffusion of PCPDE leads to further propagation and core expansion. This eventually gives rise to secondary assembly of the nanospheres to give kinetically trapped nanocaterpillar structures or star-like micelles at higher PCPDE loadings. Unlike the conventional amphiphilic BCP micelles at equilibrium, core fusion is inhibited because of the low chain mobility of the PPV core due to their strong π - π interactions (Figure 3.4).

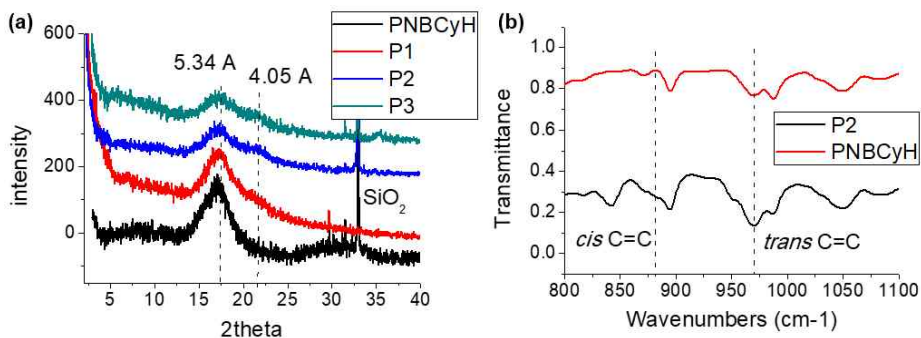


Figure 3.6. (a) Film XRD spectra of **P1-P3** compared with the spectrum of PNBCyH homopolymer. All samples were prepared by drop casting of polymer solutions (10 mg/ml, chloroform) on SiO₂ wafer. (b) The FTIR spectra of **P2** and PNBCyH homopolymer indicating both cis (CH=CH at 880 cm⁻¹) and trans (CH=CH at 970 cm⁻¹) vinylenes in PPV backbone.

The crystallinity of the PPV BCP nanostructures prepared from one-shot INCP was analyzed by X-ray diffraction (XRD), which showed a weak and broad signal at 4.05°, indicating a low crystallinity of the PPV domain, along with an interchain distance of PNBCyH first block⁸ at 5.34 Å (Figure 3.6, a). The low crystallinity of the PPV core could be attributed to the high content of cis olefins, typical in the backbone of PPVs prepared via ROMP.^{1c} The presence of cis olefins was further confirmed using FT-IR (Figure 3.6, b).⁹ These observations suggest that the low solubility of unsubstituted PPV and the strong interchain π - π interactions are the driving forces for INCP, rather than the crystallization of the core. Therefore, the PNB-*b*-PPV formed similar nanocaterpillar structures to those prepared by PNB-PA in Chapter 2, despite introduction of the different core block.

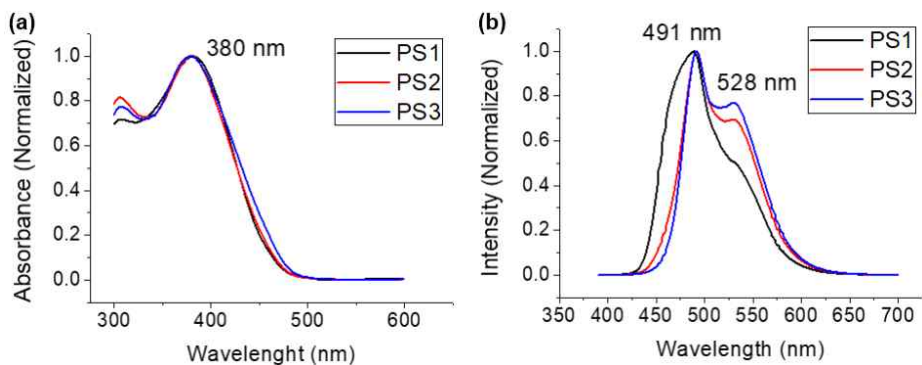
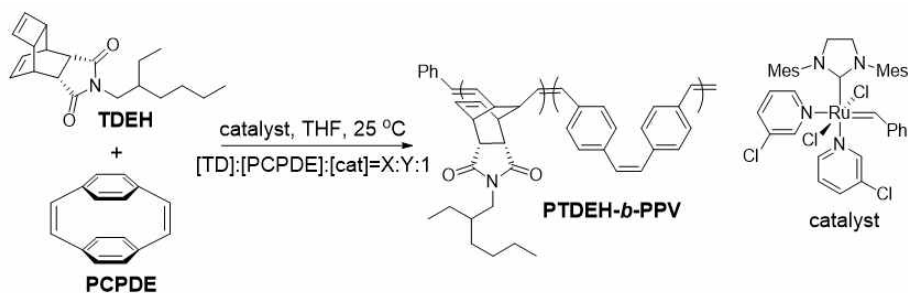


Figure 3.7. (a) The absorbance spectrum and (b) the emission spectrum of **P1-P3** in chloroform (Concentration of all polymer solution = 0.05 mg/ml). The emission of **P1** at the region of shorter wavelength and smaller 2nd peak indicates weaker aggregation due to shorter PPV.

The UV/Vis spectra of the PPV BCPs showed an absorption maximum at 380 nm in chloroform, and an optical band gap of 2.6 eV, which were blue-shifted compared to those of conventional alkoxy-substituted MEH-PPV¹⁰ and more similar to those of alkyl substituted PPV synthesized by ROMP¹¹ (Figure 3.7, a, and Table S3.1). The photoluminescence spectrum also showed similar trend having an emission maximum at 491 nm (Figure 3.7, b). The internal quantum yields of the nanoparticles were 8.8-11.2 % in chloroform (Table S3.2). Cyclic voltammetry showed that HOMO of the PPV BCP is -5.6 eV, which is 0.3 eV lower than that of MEH-PPV (Figure S3.2).¹² These lower optoelectronic values may be attributed to the absence of electron-donating alkoxy substituents and the mixed cis/trans configuration of the PPV backbone.^{11, 13}

3.3.2. One-shot *in situ* nanoparticlization of PTD-*b*-PPV: Effect of polymerization conditions on nanostructures

Table 3.2. Synthesis of PTD-*b*-PPV by one-shot ROMP using different conditions



Polymer	[TD]:[PCPDE]:[cat]	Conc. (mM) ^a	Temp. (°C)	Reaction time (h)	Conv. (%) ^b	DP _{PPV}	Yield (%)	D _h (nm) ^c
P1	50:20:1	1.7	25	48	69	14	80	555
P2	100:30:1	1.7	25	48	62	19	90	310
P3	200:30:1	1.7	25	48	89	27	94	555
P4	200:30:1	3.4	25	48	94	28	97	250
P5	200:40:1	0.66	25	48	63	25	88	370
P6	200:30:1	1.7	40	7.5	90	27	96	605
P7	200:50:1	1.7	10	72	41	21	88	640

^aConcentration based on catalyst, which is identical to the number concentration of polymer chains for the self-assembly condition. ^bConversion of PCPDE calculated by ¹H NMR. ^cMeasured by DLS using a 0.1 mg/ml solution in chloroform.

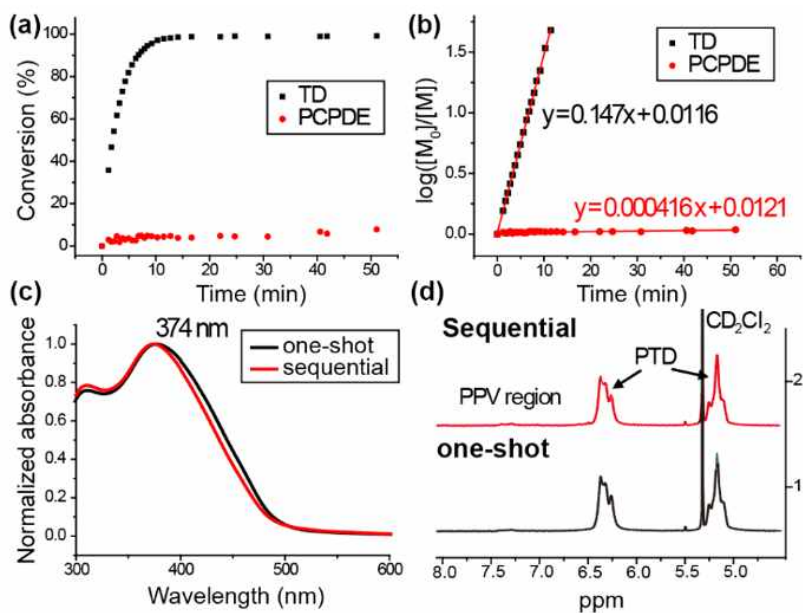


Figure 3.8. Plots of % conversion vs. time (a) and logarithmic conversion vs. time (b) for one-shot ROMP of TDEH and PCPDE with feed ratio of 50:20 ([TDEH]:[PCPDE]) at 0.1 M based on the concentration of PCPDE. UV/vis absorbance spectra (c) and ^1H NMR spectra (d) of PTDEH-*b*-PPVs synthesized by one-shot ROMP (black, bottom) and by conventional sequential monomer addition (red, top).

In order to prepare nanostructures with higher dimensionality, we synthesized PPV BCPs having rigid PTD 1st block by one-shot ROMP (Table 3.2). The synthesis was carried out by using TD derivatives and PCPDE as monomers with a fast-initiating third-generation Grubbs catalyst because the catalyst would preferentially react with the TD monomer having a sterically less hindered reactive cyclobutene moiety.¹⁴ As a result, despite copolymerization of TD and PCPDE monomers, the sterically bulkier and kinetically more demanding PCPDE would be consumed much later,² thereby producing PTD-*b*-PPVs. Then, the

aggregation of the resulting second block of insoluble PPV would drive the formation of core-shell nanostructures during polymerization via the INCP mechanism. Indeed, monitoring the conversion of TD monomers containing a 2-ethylhexyl group (TDEH) and PCPDE by *in situ* ^1H NMR suggested for one-shot block copolymerization (Figure 3.8, a). After 10 minutes of copolymerization, conversion of TDEH was already at 97% while that of PCPDE was only 4%. Furthermore, the propagation rate (k_p) of TDEH was 353 times faster than that of PCPDE (0.147 vs. 0.00042, Figure 3.8, b), enabling block copolymerization using a one-shot approach. To confirm the block-like microstructure of the resulting polymer, another PTDEH-*b*-PPV was synthesized by a conventional method of sequential monomer addition, and their ^1H NMR and UV/vis absorbance spectra were compared. Nearly identical spectra of the polymers prepared by two different methods supported the successful block copolymerization without short oligophenylene vinylene domains which would have been observed in an analogous gradient copolymer, demonstrated in Chapter 2. (Figure 3.8, c and d). Additionally, formation of the core-shell micellar structures was confirmed by the absence of signals corresponding to the PPV domains in the ^1H NMR spectrum in spite of a very strong PPV absorbance band ($\lambda_{\text{max}}=374$ nm) in the UV/vis absorbance spectrum indicating the presence of the PPV block.

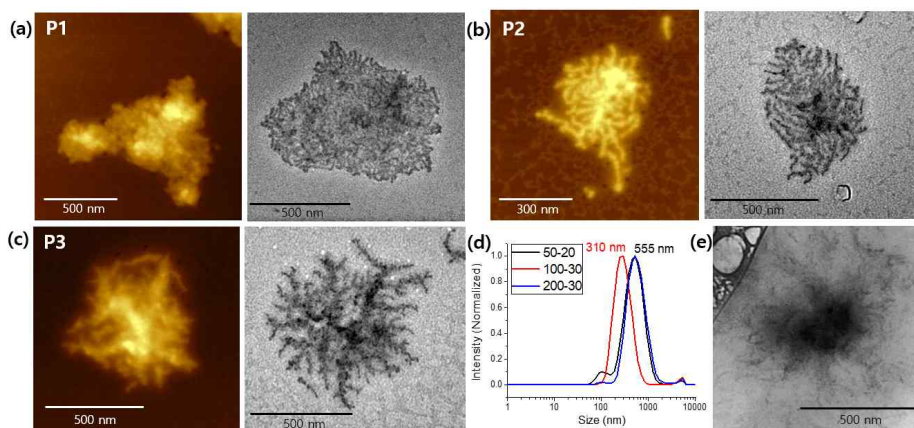


Figure 3.9. AFM (left) and TEM (right) images of PTD-*b*-PPV having a block ratio of 50:14 (**P1**, a), 100:19 (**P2**, b) and 200:27 (**P3**, c). DLS profiles (d) of different PTD-*b*-PPVs at 0.1 mg/ml in chloroform. Cryo-TEM image of **P3** (e) at 0.005 mg/ml in chloroform.

To obtain a well-defined assembly morphology, PTDEH-*b*-PPVs with different monomer feed ratios were prepared (Table 3.2, **P1-P3**). The resulting polymers in chloroform without further treatment were analyzed by DLS, AFM and TEM by spin-coating. **P1** synthesized with the feed ratio of 50:20 ([TDEH]:[PCPDE]) produced highly aggregated structures with an D_h of 555 nm (Figure 3.9, a and d). Increasing the solubilizing block to 100:30 (**P2**) reduced the irregular aggregation by enhancing the stabilization of the core, but still highly branched structures were observed ($D_h = 310$ nm, Figure 3.9, b and d). Further increasing the degree of polymerization (DP) of the solubilizing block to 200 (**P3**) produced unique fractal structures having many self-similar branches (Figure 3.9, c). To quantitatively characterize the fractal shapes, the fractal dimension (D_f)¹⁵ was calculated from the TEM images (see Experimental section and Figure S3.3). D_f has been used to characterize fractal patterns by quantifying structural complexity as the

ratio of the complexity changes to its measuring scales. So each fractal structure has its own D_f value and the characteristic D_f value for the ideal diffusion limited aggregation (DLA) fractal structure, which was generally prepared by irreversible binding of particles, is ~ 1.7 .¹⁶ Here, the calculated D_f value of **P3** was 1.73, close to the theoretical value. The average D_h value of 555 nm from DLS analysis was roughly matched with the size observed from TEM and AFM images (Figure 3.9, c and d), indicating that the nanostructures were obtained in solution. The cryo-TEM images of the vitrified chloroform solution also provided a fractal structure consistent with the structures observed from dry-TEM (Figure 3.9, e), supporting fractal formation in solution. This is significant considering the fact that most fractal structures are commonly generated on the surface of solid substrates¹⁷ and that formation of fractals composed of soft materials in solution is very rare.¹⁸

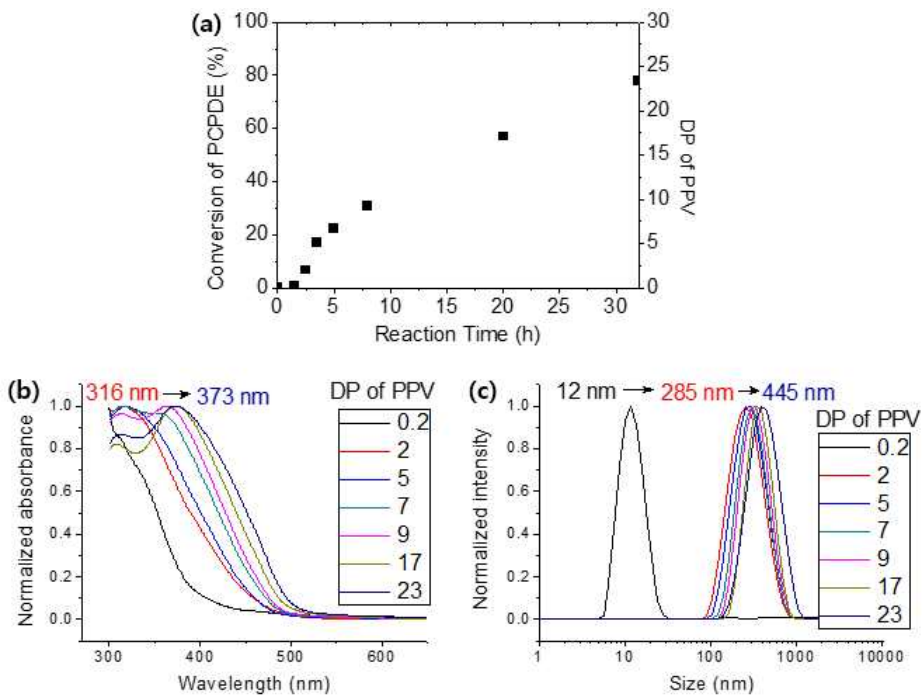


Figure 3.10. PCPDE conversion plot (a), UV/vis absorbance spectra (b), and DLS profiles (c) of PTDEH-*b*-PPVs taken from the reaction mixture at different time points. The feed ratio of 200:30 ([TDEH]:[PCPDE]) at 1.7 mM catalyst concentration was used for the experiment. The conversion was calculated by ^1H NMR. The reaction mixture was diluted with chloroform for the aforementioned analyses.

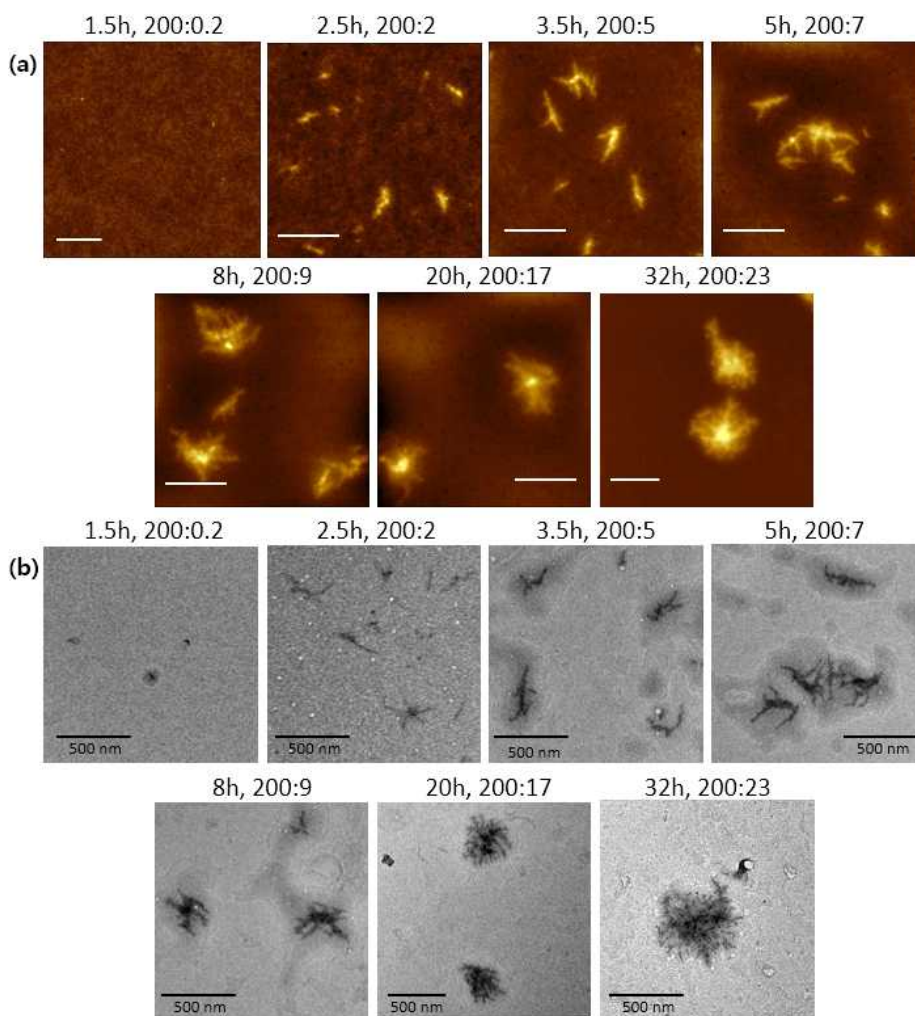


Figure 3.11. AFM (a) and TEM (b) images of PTDEH-*b*-PPVs taken from the reaction mixture at different time points. The ratios on the images indicate the actual block ratio of PTDEH-*b*-PPVs. The feed ratio of 200:30 ([TDEH]:[PCPDE]) at 1.7 mM catalyst concentration was used for the experiment. The conversion was calculated by ^1H NMR. The reaction mixture was diluted with chloroform for the aforementioned analyses.

To investigate the growth mechanism of the fractal nanostructures, time-dependent DLS, TEM, and AFM analysis were conducted by taking samples from the reaction mixtures over the course of the polymerization (Figure 3.10-11). The conversion of TDEH was quantitative, and the conversion of PCPDE, corresponding to the growth of the conjugated PPV block, was monitored by ^1H NMR and UV/vis analyses. As the reaction time progressed, the conversion of PCPDE increased from 0.7 to 77 % (corresponding to an average DP of 0.2 and 23) and so did λ_{max} , from 316 to 373 nm according to UV/vis analyses (Figure 3.10, a and b). With an average DP for PPV of 0.2, a small D_h value of 12 nm from DLS analysis was measured. Surprisingly, with still a low conversion (just 7 %) and an average DP of only 2, the D_h rapidly increased to 285 nm. Such large nanostructures were also observed by AFM and TEM images (Figure 3.11). Even though the relatively rigid backbone of the PTD block can enhance the PPV core-core interactions,^{5b} it was still unexpected and puzzling that the BCP self-assembly occurred with such a small ratio (200:2) of the insoluble block. Then, with time, the D_h of the nanostructures further increased to 445 nm and their morphology changed from rod-like to branched, and finally to fractal nanostructures (Figure 3.11). Interestingly, the center of the nanostructures and trunks of the branches got thicker, but the newly formed branch tips maintained their sharp structure. This fractal formation with gradient thickness cannot be explained by a conventional INCP mechanism,⁵ where nanostructures are self-assembled in a step-growth manner, from spherical micelles with similar sizes to linear structures, by irreversibly connecting each nanostructure. Thus, a different growth mechanism should account for the formation of the fractal nanostructures.

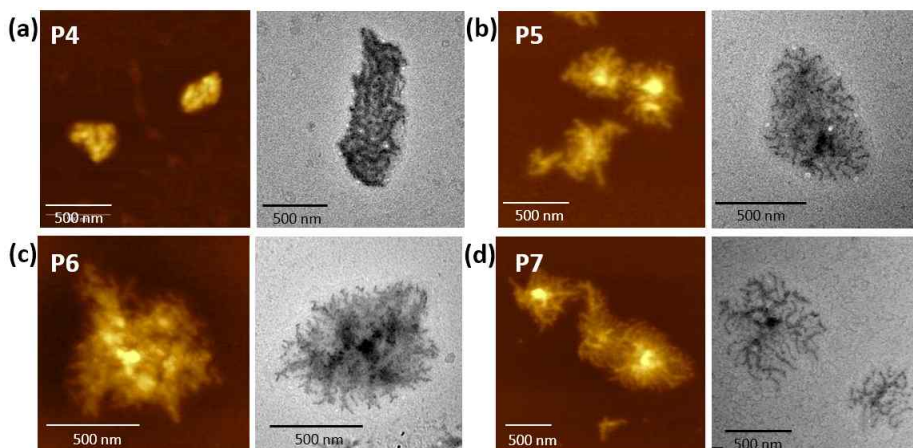


Figure 3.12. AFM (left) and TEM (right) images of PTDEH-*b*-PPVs synthesized by different conditions. Different concentrations based on catalyst: 3.4 mM (a, **P4**) and 0.66 mM (b, **P5**). Different temperatures: 40 °C (c, **P6**) and 10 °C (d, **P7**).

To explain the unusual fractal formation, we hypothesized that the assembly occurred by a DLA mechanism. In the DLA theory, particles in Brownian motion bind to each other irreversibly (nucleation) when they collide. Then, free particles continuously approach and bind to nuclei by random diffusion to produce DLA fractal structures.¹⁹ Thus, fractal growth by DLA occurs at concentrations sufficiently low to allow growth one particle at a time by random approach, preventing contact of particles in crowded conditions which would generate irregular aggregation.²⁰ To test this theory, PTDEH-*b*-PPVs were synthesized at different concentrations (Table 3.2, **P4**, and **P5**). To minimize the effect of the insoluble block ratio on nanostructures, polymers with a size similar to the PPV blocks (DP of 25-28) were prepared and imaged by AFM and TEM (Figure 3.12, a and b). Consistent with a DLA mechanism, **P4** synthesized at higher catalyst concentrations (3.4 mM vs. 1.7 mM) produced irregular aggregates

(Figure 3.12, a), hindering random diffusion before the collision of particles; while **P5**, synthesized at a lower catalyst concentration (0.66 mM), assembled into a fractal structure similar to **P3** (Figure 3.12, b). These results showed the importance of the polymerization concentration for fractal formation.

Temperature also can change diffusion dynamics of polymer particles producing different shapes of the fractals. According to the DLA theory, the particles following short random walks generally collide to outer branches to form open structures, while the particles following long random walks form compact structures by penetrating into the cluster core and avoiding contact with the outer branches. Therefore, the particles at higher temperature diffuse rapidly over long distance and form fractal structures having higher density.^{15, 20} At different temperature, PTDEH-b-PPVs were synthesized to confirm this phenomenon (Table 3.2. **P6** and **P7**). Because of too low solubility and slow propagation of PCPDE at the lower temperature, **P7** contained shorter PPV with DP of 21. Increasing the temperature to 40 °C led to more densely packed fractal structures while decreasing the temperature to 10 °C led to less crowded open fractals with longer branches (Figure 3.12, c and d). This shape dependency on the different polymerization conditions matched well with the fractal structures generated by DLA mechanism, and supported the nanostructures were formed during polymerization process.

3.3.3. One-shot *in situ* nanoparticlization of PTD-*b*-PPV: Effect of polymerization kinetics on nanostructures

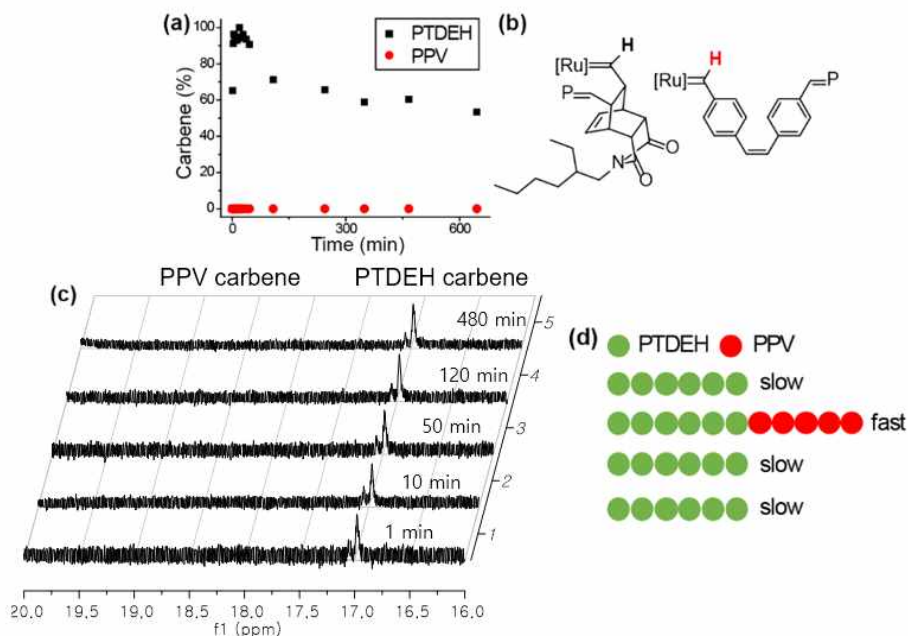


Figure 3.13. Percentage of remaining PTDEH and PPV propagating carbenes vs. time plot (a) for the one-shot ROMP of TDEH and PCPDE with feed ratio of 50:20 at 0.1 M PCPDE. (b) The structures of PTDEH (with black bold proton) and PPV (with red bold proton) propagating carbenes. (c) The propagating carbene region of ^1H NMR spectra taken during one-shot polymerization of TDEH and PCPDE. (d) Schematic representation of poorly controlled block copolymerization using TDEH and PCPDE.

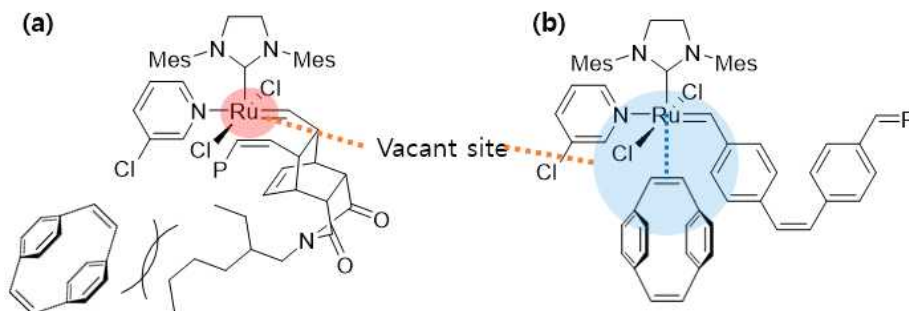


Figure 3.14. Schematic explanation for the steric on PCPDE approaching to PTDEH propagating center (a) and PPV propagating center (b).

It was still inexplicable why INCP from one-shot copolymerization of PTDEH-*b*-PPV would produce unique fractal nanostructures, presumably via a DLA mechanism, while other previous examples did not. To get more insights, a detailed kinetic analysis of a model block copolymerization was conducted by monitoring the carbenes of both propagating species using in situ ^1H NMR (Figure 3.13, a-c). The chemical shifts were easily distinguished as 17.0 ppm corresponding to propagating carbenes from PTDEH and 19.0 ppm to propagating carbenes from PPV. Surprisingly, the propagating carbene signal from the first block, PTDEH, decreased very slowly for more than 10 hours; indicating extremely slow initiation from the living end of PTDEH macroinitiators to produce the PPV block. This slow initiation is presumably due to the intense steric repulsion between the sterically hindered PTDEH chain end¹⁴ and the bulky olefin of PCPDE (Figure 3.14, a).² After the initiation of PPV, the new but smaller propagating carbenes of PPV=[Ru] would have a larger vacant site for the next PCPDE monomer leading to the faster propagation of PPV (Figure 3.14, b). Then, these growing PPV carbenes quickly disappeared due to

non-solvated core-shell self-assembly, resulting in the detection of a low amount of the PPV propagating carbenes throughout the polymerization (Figure 3.13, a-c). This slow initiation and fast propagation led to small k_i/k_p , resulting in poorly controlled polymerization of the PPV block (Figure 3.13, d) and discrepancy between the calculated average and the actual DP of PPV on the block copolymers for those with a successful chain extension from PTDEH to PPV. This accounts for the formation of seemingly premature assembly structures even with the average PPV DP of only 2 (Figure 3.10-11), since the actual DP for those nanostructures should be higher than 2. This implies that the uncontrolled, slow initiation of the insoluble PPV block could induce the gradual generation of block copolymers and then micellar structures instead of simultaneous self-assembly, and eventually, this becomes the key to the mechanism of fractal formation.

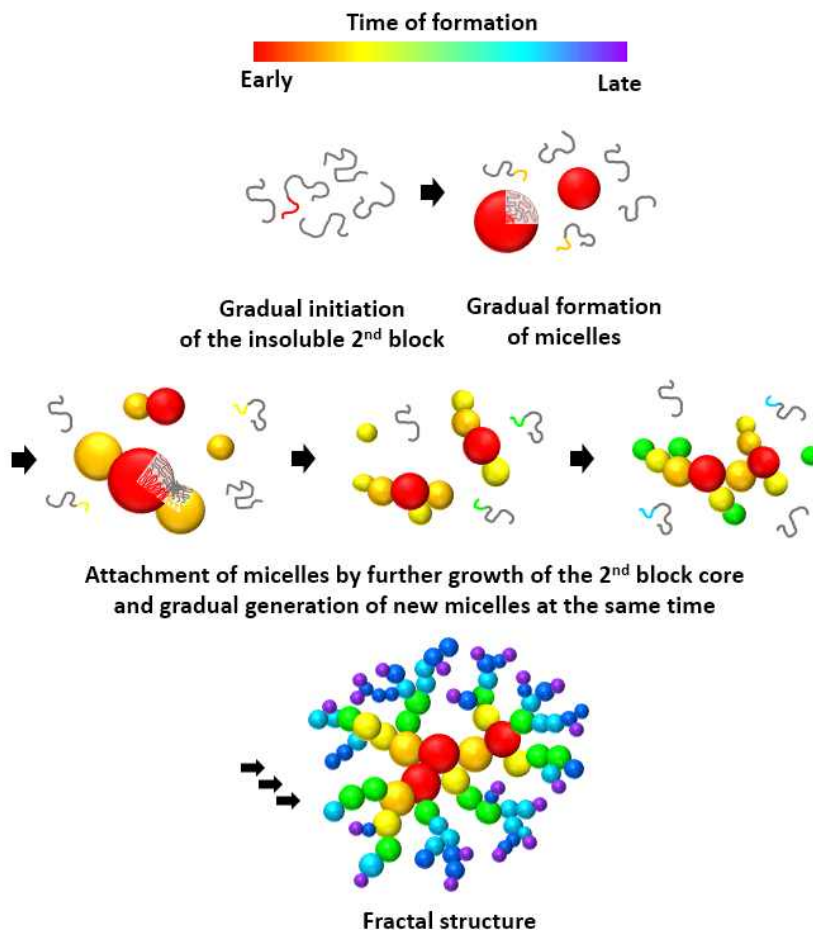


Figure 3.15. Proposed mechanism of fractal nanoparticle generation by gradual formation of new micelles from uncontrolled polymerization. The color change indicates the time of the insoluble block and micelle formation.

Considering the gradual generation of micelles by the uncontrolled polymerization, we propose that the unique fractal structures are formed by a continuous growth or chain-growth-like mechanism (Figure 3.15). In the early stage, the uncontrolled initiation of the PPV block generates a few micellar structures, and grows to

larger sizes due to monomer diffusion to the cores which still contain the propagating carbenes.⁵ Now, these can act as nuclei for fractal growth. Then, the newly generated micelles diffuse to the nuclei and start to grow, thereby making new additional branches by a chain growth-like mechanism. This gradual generation of micelles provides a sufficiently low concentration of micelles so that the DLA mechanism is operative. This is in strong contrast to the behavior previously observed with controlled polymerization kinetics, where a high concentration of micelles is generated from an early stage and a step-growth-like mechanism of micelle assembly to linear objects is observed (Figure 3.16).⁵

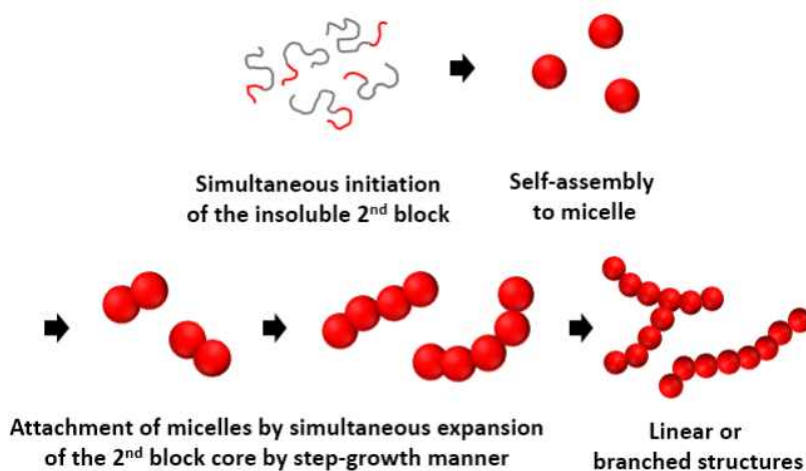
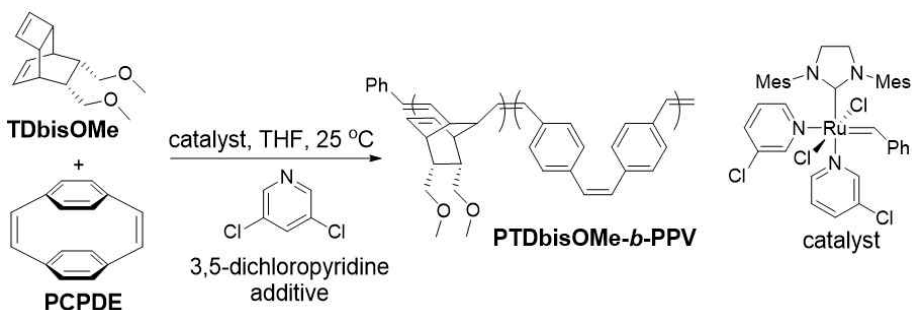


Figure 3.16. The mechanism of the conventional INCP by controlled living polymerization.

Table 3.3. Synthesis of PTD-*b*-PPV by one-shot ROMP using bismethoxy substituted TD, PCPDE, and 3,5-dichloropyridine additive.



Polymer	[TD]:[PCPDE] :[cat]:[additive]	Conc. (mM) ^a	Reaction time (h)	Conv. (%) ^b	DP _{PPV}	Yield (%)	D _h (nm) ^c
P8	200:30:1:0	1.7	48	90	27	95	560
P9	200:30:1:15	1.7	55.5	51	15	91	415
P10	200:30:1:0	1.7	2	49	15	89	440

^aConcentration based on catalyst, which is identical to the number concentration of polymer chains for the self-assembly condition. ^bConversion of PCPDE calculated by ¹H NMR. ^cMeasured by DLS using a 0.1 mg/ml solution in chloroform.

If this proposed gradual self-assembly accounts for the fractal formation via a DLA mechanism, then, well-controlled block copolymerization should produce micelles simultaneously and form the conventional linear caterpillar structures in a step-growth manner (Figure 3.16).⁵ To test this proposal, we tried to control the polymerization of PTD-*b*-PPV by increasing the k_i/k_p ratio. To accelerate the initiation rate, we used a less sterically hindered bismethoxy substituted TD monomer (TDbisOMe) instead of TDEH (Table 3.3, **P8**). Furthermore, 15 equivalents of the weakly coordinating 3,5-dichloropyridine additive were used to reduce the k_p of PPV as a result of competition with the PCPDE mono-mer (Table 3.3, **P9**). To check how the use of

TDbisOMe and the 3,5-dichloropyridine additive affected the controlled polymerization, another set of polymerization kinetic investigations by ^1H NMR were performed. The sequential addition of the monomers, by adding PCPDE after the full conversion of the TDbisOMe monomer, allowed us to get clearer kinetic data (Figure 3.17). The use of TDbisOMe led to a more rapid conversion of PTDbisOMe propagating carbenes to PPV propagating carbenes (Figure 3.17, a and b, and Figure 3.18), with a 6.7 times faster k_i than in the previous case using TDEH (Figure 3.17, c, 0.0046 vs 0.0007). This change also led to a 1.7 times faster k_p (Figure 3.17, d, 0.0014 vs 0.0008), resulting overall in a four-times higher k_i/k_p than when using TDEH as the monomer (3.3 vs 0.83). However, using TDbisOMe as the monomer alone could not sufficiently improve the control of block copolymerization, since half of PTDbisOMe carbenes still remained after the full conversion of PCPDE (Figure 3.17, a). On the other hand, introducing the additive significantly retarded the propagation of PPV by two (relative to TDEH) or 3.4 times compared with using only TDbisOMe without the additive (Figure 3.17, d). As a result, the k_i/k_p value increased 13.5 times (11 vs 0.83) due to the synergy of faster initiation of PPV from the PTDbisOMe propagating chain ends and much slower propagation of PPV. Therefore, this significantly high k_i/k_p value should result in well-controlled block copolymerization (Figure 3.18, c).

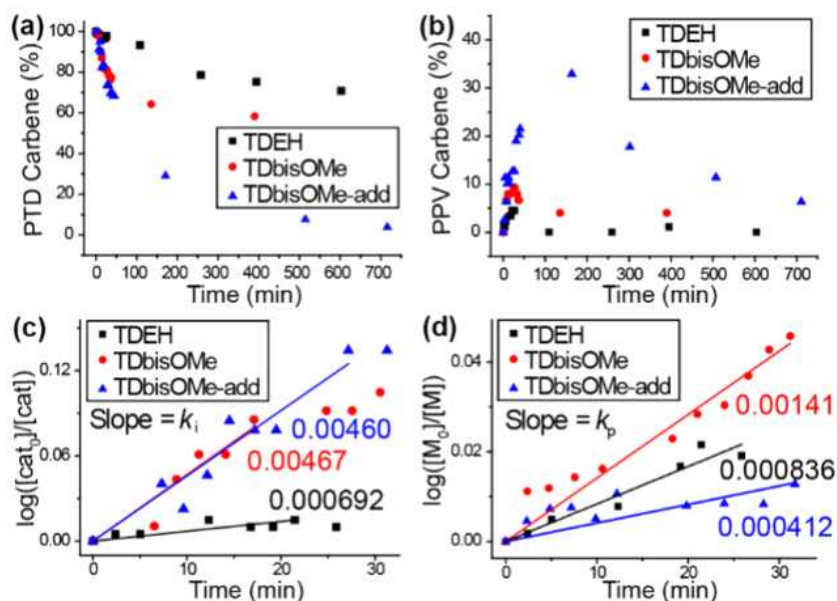


Figure 3.17. Reaction kinetic plots monitoring the change in the PTB propagating carbenes (a) and the PPV propagating carbenes (b) during the polymerization of PTB-*b*-PPV via the sequential addition of the monomers using TDEH or TDbisOMe as the first block monomer with or without 15 equivalents of 3,5-dichloropyridine additive. The kinetic plots to calculate various k_i (c) and k_p (d) of PPV at the early stage of the second block polymerization. The slope values are shown below the corresponding plots.

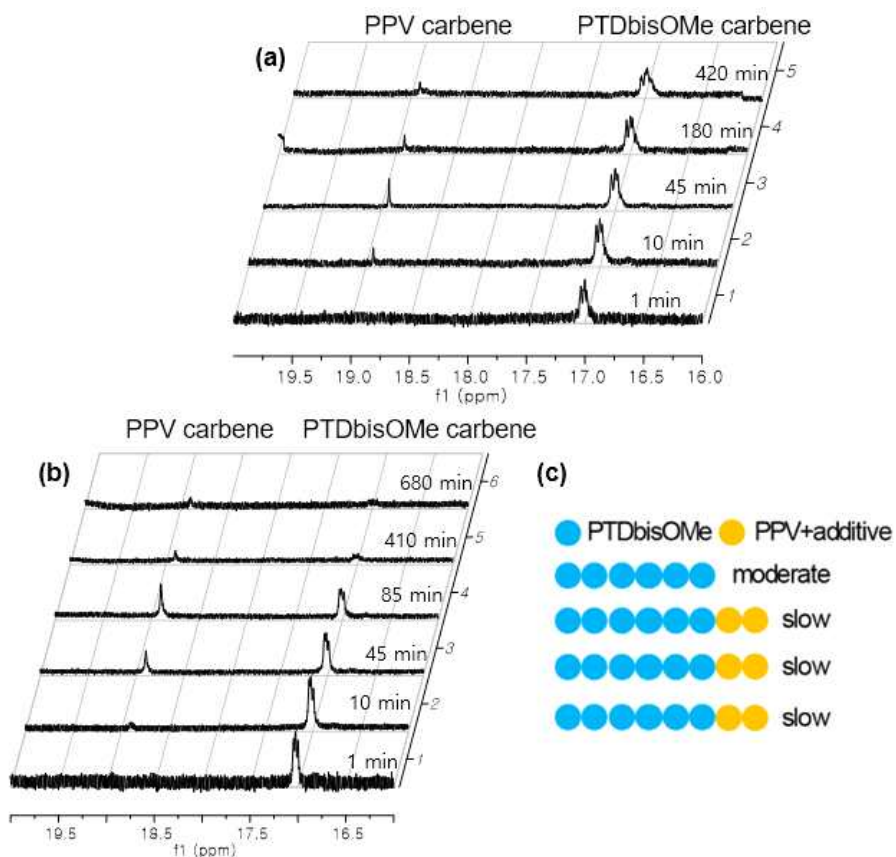


Figure 3.18. The propagating carbene region of ^1H NMR spectra taken during one-shot polymerization of TDbisOMe and PCPDE (a), and TDbisOMe and PCPDE with 3,5-dichloropyridine additive (b). (c) Schematic representation of well-controlled polymerization using TDbisOMe and PCPDE with 3,5-dichloropyridine additive.

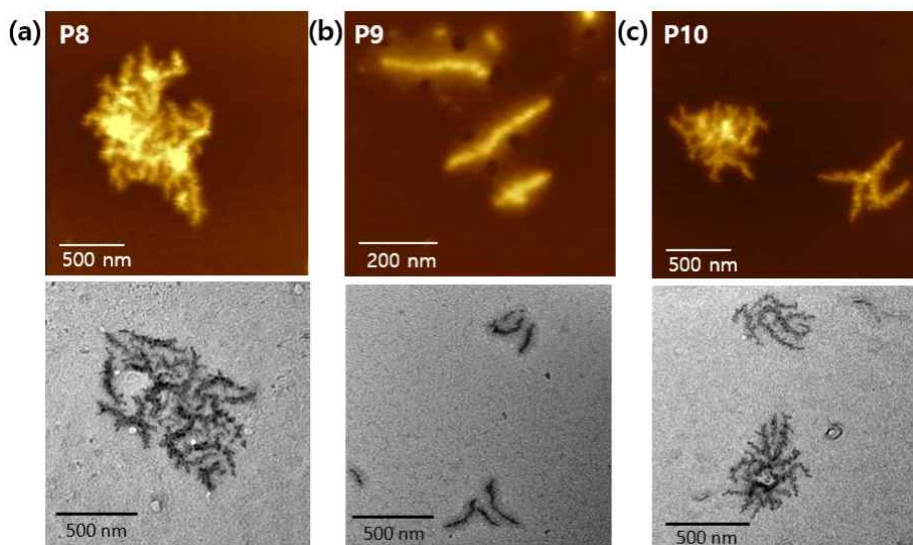


Figure 3.19. AFM (up) and TEM (down) images of PTDbisOMe-*b*-PPVs having block ratios of 200:27 (a, **P8**), 200:15 synthesized with 3,5-dichloropyridine (b, **P9**), and 200:15 without the additive (c, **P10**).

With this background kinetic information, we imaged **P8** and **P9** by AFM and TEM. As predicted, **P8** synthesized using only TDbisOMe still produced the fractal structures (Figure 3.19, a) because of insufficient control on the block copolymer microstructure. However, **P9** prepared with both TDbisOMe and the additive resulted in linear nanocaterpillar structures having a consistent thickness at the center and the tip (Figure 3.19, b), similar to the nanocaterpillar structures prepared by conventional INCP composed of PNB-*b*-PPV or PA block copolymers reported in Chapter 2.⁵ This observation is consistent with well-controlled block copolymerization with high k_i/k_p values, suggesting that the simultaneous growth of the PPV block produced linear, not fractal structures (Figure 3.19, b). Considering the shorter DP of PPV (15) caused by slow propagation with the additive, another BCP having a similar DP of PPV (15) was synthesized without additive as a control

experiment (Table 3.3, **P10**). Even with **P10** having a short average DP of PPV, poorly controlled block copolymerization resulted in the same fractal, not the linear structure (Figure 3.19, c). Therefore, the role of the weakly coordinating additive appears to be decisive to produce linear nanostructures instead of the fractal structures. The clear tendency between nanostructures and block copolymerization kinetics is in good agreement with our working hypothesis that polymerization kinetics can control micelle generation, which then determines the final morphology of the nanostructures prepared via an INCP method. Such a relationship between polymerization kinetics and nanostructures emphasizes the importance on researches about controlling reactivity of monomers.

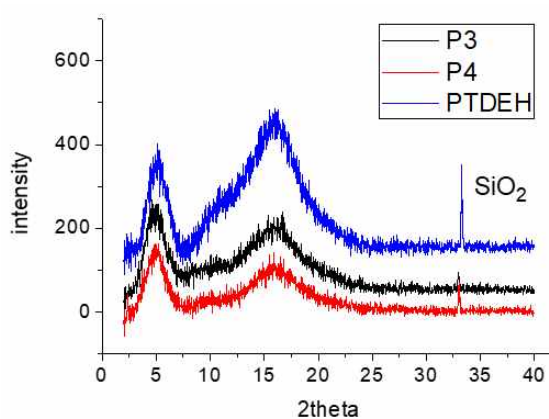


Figure 3.20. Film XRD spectra of **P3** and **P4** compared with the spectrum of PTDEH homopolymer. All samples were prepared by drop casting of polymer solution (10 mg/ml, chloroform) on SiO₂ wafer.

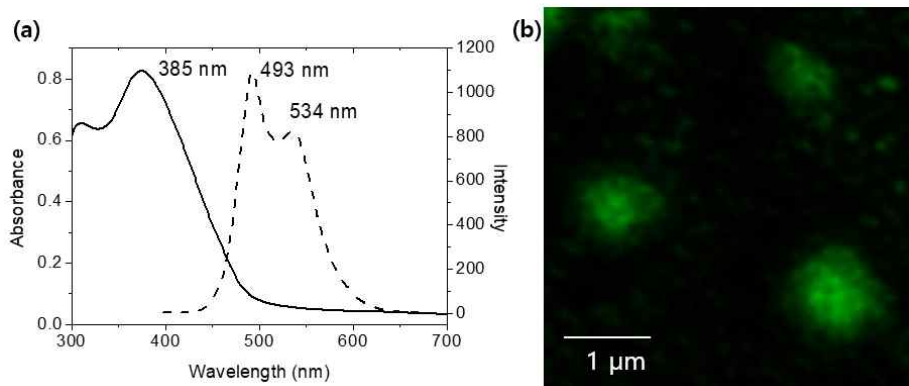


Figure 3.21. (a) Absorbance and emission spectra of **P3** in chloroform. at 0.05 mg/ml. (b) Fluorescent image of **P3**.

Lastly, various properties of the fractal particles prepared by PTDEH-*b*-PPV BCPs were investigated. The X-ray diffraction (XRD) analysis indicated that the PPV core was amorphous, which was also supported by the absence of a vibronic band or band shift on the UV/Vis absorbance spectra (Figure 3.20 and 3.21, a). These results indicate that the fractal structure was composed of kinetically trapped micelles in the absence of crystallization. As a result, the fluorescence quantum yield of the structures was 22.9 % in chloroform solution, somewhat higher than the value of PNB-*b*-PPV (8.8-11.2%). From this fluorescent property, one could also image the fractal particles by super-resolution fluorescent images (Figure 3.21, b). This class of fractal nanostructures having a high surface area can potentially be useful for sensors, imaging materials, and optoelectronic devices.

3.4. Conclusion

Fluorescent nanostructures were successfully prepared by facile one-shot INCP method using PCPDE as a monomer to synthesize PPV block copolymers. Sterically demanding PCPDE monomer retarded propagation of PPV, leading to near-perfect block copolymer microstructure of PNB-*b*-PPV synthesized by one-shot ROMP using NB and PCPDE. Even though the core-forming block was changed from PA to PPV, PNB-*b*-PPV formed similar nanocaterpillar structures to those prepared from PNB-*b*-PA, due to irregularly trapped PPV block without characteristic crystallization of PPV. One-shot copolymerization of PPV block copolymers with TD monomer produced novel nanostructures having unique fractal shape. Systematic studies of reaction kinetics revealed that the key factor for the self-assembly into fractal structures was the extremely slow initiation of PPV due to large steric hindrance between PTD propagating species and PCPDE. The uncontrolled polymerization kinetics of the PPV produced micelles not at once, but gradually. This led to nucleation of the micelles followed by the continuous formation of new branches from successive micelle supplies. Therefore, at sufficiently low polymerization concentrations, the irreversible binding of kinetically trapped micelles via a chain-growth-like mechanism accounted for the DLA fractal structures. Such a method for modulating nanostructures by altering polymerization conditions such as kinetics, concentration, and temperature was possible due to the unique characteristics of INCP method which allowed irreversible formation of nanostructures during polymerization. We expect this novel method can open the door for the development of novel self-assembly processes that would otherwise be challenging to accomplish via the conventional equilibrium-driven self-assembly of polymers.

3.5. Experimental section

Characterization

NMR spectra were recorded by Varian/Oxford As-500 (500 MHz for ^1H /125 MHz for ^{13}C) spectrometer and Bruker ultrashield spectrometer (600 MHz for ^1H /150 MHz for ^{13}C). UV/vis spectra were obtained by a Jasco Inc. UV/vis spectrometer V-630, and fluorescence spectra were obtained by FP-8300 (Jasco Inc.). Quantum efficiency was measured by QE-1200 (Otsuka Electronics). Dynamic light scattering (DLS) data were obtained by a Malvern Zetasizer Nano ZS. Film state X-ray diffraction (XRD) was performed by the National Instrumentation Center for Environmental Management (NICEM) at SNU using D8 Discover with GADDS (Bruker, Germany). IR spectra were measured on a Thermo Scientific Nicolet 6700 spectrometer. Cyclic voltammetry (CV) measurements were carried out on a CHI 660 Electrochemical Analyzer (CH Instruments, Inc., Texas, USA) using a degassed acetonitrile solution of tetrabutylammonium hexafluorophosphate (Bu_4NPF_6 , 0.1 M). Multimode 8 and Nanoscope V controller (Veeco Instrument) were used for AFM imaging. All images were obtained on tapping mode using noncontact mode tip from Nanoworld (Pointprobe tip, NCHR type) with spring constant of 42 N m⁻¹ and tip radius of ≤ 8 nm.

Materials

All reagents were commercially available from Acros, Alfa, Sigma Aldrich and TCI and used without further purification unless specified otherwise. 1,2-Dichloroethane was distilled under a nitrogen atmosphere over calcium hydride. All polymerizations were carried out under dry argon atmospheres using standard Schlenk techniques. THF was distilled over sodium and benzophenone and anhydrous deuterium THF solvent (≥ 99.95 %) were purchased from Euriso-Top[®]. THF solvents were

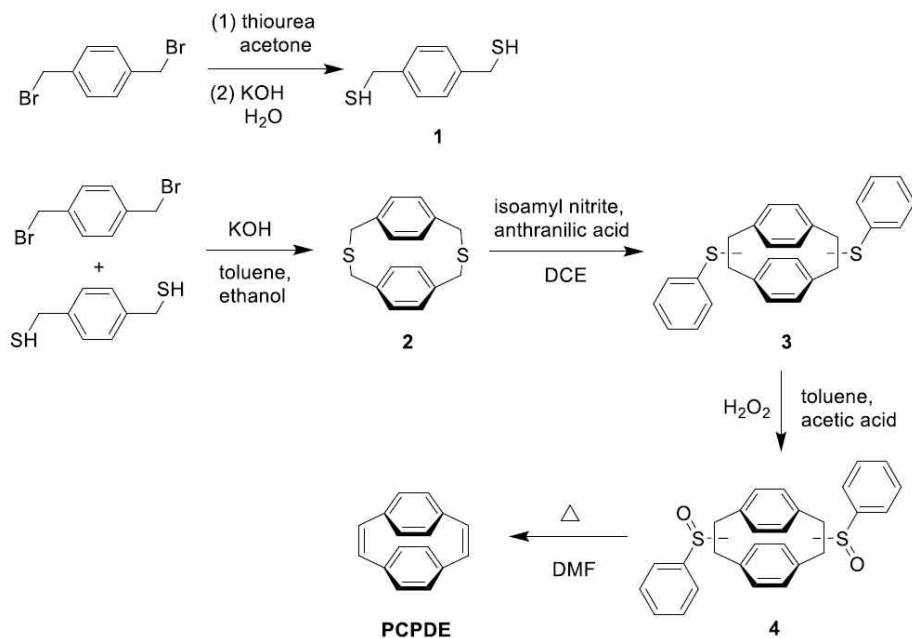
degassed by argon bubbling for 10 minutes before using on polymerization. The third generation Grubbs catalyst was prepared by the reported method.²²

Synthesis of monomers

Synthesis of 7,8-bismethoxymethyl-endo-tricyclo[4.2.2.0^{2.5}]deca-3,9-diene (TDbisOMe)

The 50 mL RBF with dialcohol (0.30g, 1.95 mmol) solution in tetrahydrofuran (15mL) was prepared. Then sodium hydride (60%, 0.23 g, 5.85 mmol) was added at 0 °C and the reaction mixture was stirred for 30 minutes increasing temperature to room temperature. Iodomethane (99%, 0.36 ml, 5.85 mmol) was added and then the mixture was stirred for 1.5 hours increasing temperature to 50 °C. After completion of the reaction, the mixture was quenched by addition of MeOH and water at 0 °C. The mixture was washed with saturated brine and then organic layer was extracted with ethyl acetate 3 times. The organic layer was dried with MgSO₄ and the solvent was removed on a rotary evaporator. The product was purified by column chromatography with ethyl acetate-hexane mixture (1:10 in volumetric ratio). The separated product solutions were collected and concentrated to yield 0.41 g of final product. Yield: 96 %; transparent liquid; ¹H NMR (500 MHz, CDCl₃): δ 5.94 (dd, J_{ab} = 3.25 Hz, J_{ac} = 4.75 Hz, 2H), 5.84 (s, 2H), 3.33-3.36 (m, 2H), 3.30 (s, 6H), 3.11-3.14 (m, 2H), 2.69 (s, 4H), 2.05 (t, J = 5.0 Hz, 2H); ¹³C NMR (125 MHz, CDCl₃): δ 137.86, 129.48, 73.78, 58.65, 45.70, 40.81, 37.86. HRMS (ESI, [M+Na]⁺): calculated for [C₁₄H₂₀NaO₂]⁺: m/z 243.1361, found m/z 243.1358.

Synthesis of [2,2]paracyclophane-1,9-diene (PCPDE)



Scheme 3.2. Synthetic routes to [2,2]paracyclophane-1,9-diene.

Synthesis of 1,4-bis(thiolatomethyl)benzene (1)

A suspension of 1,4-bis(bromomethyl)benzene (9.0 g, 34.1 mmol) and thiourea (6.2 g, 96.6 mmol) was dissolved in acetone (100 mL) and stirred under reflux for 5 hours. The solution was cooled and removed most of solvent. The resulting bis(isothiuronium) salt was collected and heated under reflux with a deoxygenated solution of KOH (7.64 g, 136 mmol) in water (210 mL) under a nitrogen atmosphere for 5 hours. Sulfuric acid was added under a nitrogen atmosphere with ice bath. The reaction mixture was extracted into DCM, the combined organic layers were washed with water, dry with anhydrous MgSO₄, filtered and evaporated. The crude product was precipitate from hot methanol

and gave compound 1 as white solids in a yield of 97%. ¹H NMR (600 MHz, CDCl₃): δ 7.28 (s, 4H), 3.73 (d, J = 7.8 Hz, 4H), 1.75 (t, J = 7.8 Hz, 2H). ¹³C NMR (150 MHz, CDCl₃): δ 140.29, 128.48, 28.73. HRMS (EI, [M]⁺): calculated for [C₈H₁₀S₂]⁺: m/z 170.0218, found m/z 170.0214.

Synthesis of 2,11-dithia[3,3]-paracyclophane (2)

A deoxygenated mixture of 1,4-bis(bromomethyl)benzene (7.6 g, 28.8 mmol) and 1,4-bis(thiolatomethyl)benzene (4.9 g, 28.8 mmol) in toluene (480 mL) was added dropwise to a solution of KOH (4.0 g, 71.3 mmol) in ethanol (720 mL) under a nitrogen atmosphere for a period at least 72 hours. After a further 2 hours, the solvent was evaporated and the residue was extracted with HCl and DCM. The organic layers were combined, washed by water, dried with anhydrous MgSO₄, filtered and evaporated. The residue were purified by column chromatography with using DCM:hexane (2:8) as the eluent. The cyclic compound was obtained as white solids in a yield of 63%. ¹H NMR (600 MHz, CDCl₃): δ 6.86 (s, 8H), 3.81(s, 8H). ¹³C NMR (150 MHz, CDCl₃): δ 135.65, 129.71, 38.45. HRMS (EI, [M]⁺): calculated for [C₁₆H₁₆S₂]⁺: m/z 272.0688, found m/z 272.0687.

Synthesis of bis(sulfide) compounds (3)

Isoamyl nitrite (11.3 mL, 84.2 mmol) was added dropwise into a solution of anthranilic acid (10.0 g, 20.63 mmol) and 2,11-dithia[3,3]-paracyclophane (5.6 g, 20.6 mmol) in dichloroethane (630 mL) under reflux and a nitrogen atmosphere for at least 30 minutes. The reaction mixture was boiled under reflux for another 30 minutes. After the reaction mixture was concentrated under reduced pressure, the residue was purified by column chromatography using a

solvent system of DCM and hexane (1:9). Collection of the main fraction gave the oil in a yield of 35%. ^1H NMR (600 MHz, CDCl_3): δ 7.47-7.42 (m, 4H), 7.17-7.24 (m, 4H), 7.12-7.17 (m, 2H), 6.96-7.07 (m, 2H), 6.41-6.81 (m, 6H), 4.37-4.81 (m, 2H), 3.75-3.83 (m, 2H), 2.67-2.90 (m, 2H). HRMS (EI, $[\text{M}]^+$): calculated for $[\text{C}_{28}\text{H}_{24}\text{S}_2]^+$: m/z 424.1314, found m/z 424.1311.

Synthesis of bis(sulfoxide) compounds (4)

Hydrogen peroxide (1.3 mL) was added dropwise to the solution of compound **3** (3.1 g, 7.22 mmol) in toluene (175 mL) and acetic acid (56 mL) at 0 °C under a nitrogen atmosphere over a period of 20 minutes. The mixture was allowed to warm up to room temperature and stirred for additional 18 hours. The resulting solution was then extracted successively with brine and DCM, dried with MgSO_4 and concentrated to give pale yellow oil in an overall yield of 99%. The compounds contain a large number of stereoisomers and were used as starting materials for the next step without purification. ^1H NMR (600 MHz, CDCl_3): δ 7.67-7.86 (m, 4H), 7.42-7.58 (m, 6H), 6.83-7.28 (m, 4H), 6.12-6.63 (m, 4H), 3.94-4.20 (m, 2H), 3.5-3.61 (m, 1H), 3.38-3.50 (m, 1H), 3.15-3.36 (m, 2H). HRMS (FD, $[\text{MH}]^+$): calculated for $[\text{C}_{28}\text{H}_{25}\text{O}_2\text{S}_2]^+$: m/z 457.1291, found m/z 457.1281.

Synthesis of [2,2]paracyclooctaphane-1,9-diene (PCPDE)

A solution of compound **4** in *N,N*-dimethylformamide was refluxed under a nitrogen stream for 20 hours. The solution was cooled to room temperature and extracted successively with dilute aqueous HCl and DCM, dried with anhydrous MgSO_4 , filtered and concentrate. The crude compound was then chromatographed over silica gel using DCM:hexane (1:9) for elution and gave PCPDE as white solids in a yield of 35%.

^1H NMR (600 MHz, CDCl_3): δ 7.20 (s, 4H), 6.50 (s, 8H). ^{13}C NMR (150 MHz, CDCl_3): δ 137.98, 137.20, 130.80. HRMS (EI, $[\text{M}]^+$): calculated for $[\text{C}_{16}\text{H}_{12}]^+$: m/z 204.0934, found m/z 204.0927.

General procedure for the one-shot INCP of PNB-*b*-PPV

Both comonomers (62.8 μmol for NB and 6.28-37.7 μmol for PCPDE) were weighed into a 2 mL sized screw-cap vial with a septum and purged with argon. Anhydrous and degassed THF was added (43-360 μL) to the vial. THF solution of the third-generation Grubbs catalyst (1.26 μmol) was added (20 μL) to the monomer solution at once under vigorous stirring. The mixture was stirred for 4-12 h at the room temperature. The reaction was quenched by excess ethyl vinyl ether. The crude mixture was precipitated into methanol(**P1-P3**), and the obtained powder was dried *in vacuo*.

Poly(NBCyH)-*b*-poly(PCPDE) one-shot copolymers (P1-P3)

Yield: 82-93% (see Table 3.1). ^1H NMR (500 MHz, CD_2Cl_2): δ 7.08-7.39 (m), 6.30-6.57 (m) 5.73 (s, 1H), 5.47-5.50 (d, 1H), 3.85 (s, 1H), 2.66-3.18 (m, 4H), 2.08 (s, 3H), 1.80 (s, 2H), 1.52-1.63 (m, 4H), 1.20-1.29 (m, 3H). ^{13}C NMR (125 MHz, CDCl_3): δ 178.6, 133.8, 132.0, 52.9, 52.6, 51.5, 50.9, 46.6, 46.1, 42.4, 41.0, 28.9, 26.0, 25.2 (all the PNBCyH-*b*-P(PCPDE) one-shot copolymers have identical ^1H -NMR and ^{13}C -NMR spectra).

General procedure for the one-shot INCP of PTD-*b*-PPV

Both comonomers (31.4-126 μmol for TDEH or TDbisOMe and 12.6-31.4 μmol for PCPDE) were weighed into a 4 mL sized screw-cap vial with a septum and purged with argon. Anhydrous and degassed THF was added (165-932 μL) to the vial. THF solution of

the third-generation Grubbs catalyst (0.63 μ mol) was added (20 μ L) to the monomer solution at once under vigorous stirring. The mixture was stirred for 2-72 h at different temperatures. The reaction was quenched by excess ethyl vinyl ether. The crude mixture was precipitated into methanol, and the obtained powder was dried *in vacuo*.

Poly(TDEH)-*b*-poly(PCPDE) one-shot copolymers (P1-P7)

Yield: 88-97% (see Table 3.4); ^1H NMR (500 MHz, CDCl_3): δ 6.32 (d, 2H), 5.14 (t, 2H) 2.69-3.24 (m, 8H), 1.62 (s, 1H), 1.20-1.25 (d, 8H), 0.84-0.87 (m, 6H); ^{13}C NMR (125 MHz, CDCl_3): δ 178.4, 132.3, 131.4, 44.1, 42.7, 40.9, 38.7, 37.5, 30.6, 28.7, 23.8, 23.2, 14.2, 10.4 (all the PTDEH-*b*-P(PCPDE) one-shot copolymers have identical ^1H -NMR and ^{13}C -NMR spectra).

Poly(TDbisOMe)-*b*-poly(PCPDE) one-shot copolymers (P8-P10)

P9 was synthesized by the general one-shot procedure using 3,5-dichloropyridine (9.43 μ mol) with the comonomers. Yield: 89-95% (see Table 3.5); ^1H NMR (500 MHz, CDCl_3): δ 6.20 (s, 2H), 4.92-5.03 (m, 2H) 3.02-3.27 (m, 10H), 2.82 (s, 2H), 2.25-2.56 (m, 4H); ^{13}C NMR (125 MHz, CDCl_3): δ 133.1, 132.7, 132.5, 131.5, 130.8, 73.7, 73.5, 73.1, 58.5, 47.8, 42.2, 41.9, 41.6, 41.4, 40.5 (all the PTDbisOMe-*b*-P(PCPDE) one-shot copolymers have identical ^1H NMR and ^{13}C NMR spectra).

***In Situ* ^1H NMR analysis of one-shot ROMP using NB and PCPDE**

157 μ mol of NB and 62.8 μ mol of PCPDE and hexamethyldisilane (~3 mg, an internal standard) were added into NMR tube and purged with argon. Anhydrous and degassed deuterated THF was added (550 μ L) to the NMR tube and stabilized at 0 $^\circ\text{C}$ in NMR instrument.

Then, the initial ratio of all compounds was measured by ^1H NMR analysis. After that, the solution of the third-generation Grubbs catalyst (3.14 μmol , 70 μL , 0 $^\circ\text{C}$) was added and the conversion of the two monomers was monitored by every 25 seconds. The measurement was done by Avance-500 (500 MHz for ^1H , Bruker, Germany) in the National center for Inter-University Research Facilities (NCIRF) at SNU.

***In situ* ^1H NMR analysis of one-shot ROMP using TD and PCPDE**

157 μmol of TDEH or TDbisOMe and 62.8 μmol of PCPDE and hexamethyldisilane (~ 3 mg, an internal standard) were added into NMR tube and purged with argon. Anhydrous and degassed deuterated THF was added (550 μL) to the NMR tube and then the initial ratio of all compounds was measured by ^1H NMR analysis. After that, the solution of the third-generation Grubbs catalyst (3.14 μmol , 70 μL) was added and the conversion of the two monomers and the amount of remaining propagating carbenes were monitored by every 50 seconds. The feed ratio and the concentration were fixed to 50:20 ([TD]:[PCPDE]) and 0.1 M based on the concentration of PCPDE, respectively, in order to detect protons from propagating carbenes which show very weak signals.

Atomic force microscopy (AFM)

The atomic force microscopy experiments were performed with a thin film prepared by spin-coating one drop of the polymer solution ($\sim 0.02\text{mg}$ polymer/mL, CHCl_3 : spinning rate = 3000 rpm for 30 sec). The solvent was filtered by 0.2- μm PTFE filter before making the solution. The thin films were prepared on mica substrates. All images were obtained on tapping mode using non-contact mode tips from Nanoworld (Pointprobe tip, NCHR type) with spring constant of 42 N

m-1 and tip radius of ≤ 8 nm.

Transmission electron microscopy (TEM)

Dry-TEM and cryo-TEM imaging were performed by JEM-2100 operated at 120 kV and SC 1000 CCD camera (Gatan Inc.). The samples for dry-TEM imaging were prepared by drop casting one drop ($\sim 10 \mu\text{L}$) of sample solution (0.1 mg/mL) on the carbon-coated copper grid. The cryo-TEM experiments were performed with a thin film of solution ($5 \mu\text{L}$, 0.1 mg/mL) transferred to a lacey supported grid. The thin solution films were prepared under solvent vapor saturated condition (chloroform) within a custom-built environmental chamber in order to prevent evaporation of solvent from sample solution. The excess liquid was blotted with filter paper for 2-4 seconds, and the thin solution films were rapidly vitrified by plunging them into liquid ethane ($-170 \text{ }^\circ\text{C}$) using Gatan CryoplungeTM3 system. The grid was transferred on a Gatan 626 cryoholder, using a cryo-transfer device. After that they were transferred to a JEM-2100. Direct imaging was carried out at a temperature of approximately $-175 \text{ }^\circ\text{C}$ and with a 120 kV accelerating voltage.

Stimulated Emission Depletion (STED) Microscopy (fluorescent imaging)

STED images were obtained using a Leica TCS SP8 X STED microscope (Leica Microsystems). Excitation wavelength was 405 nm and depletion was achieved with a 592 nm laser. The sample was prepared by spin-coating one drop of the polymer solution (0.1 mg/mL, 3000 rpm for 30 sec using CHCl_3 solution) on a cover glass. The cover glass coated with sample was glued to the slide glass by clear nail polish.

Calculation of Fractal Dimension (D_f)

D_f value of **P3** was measured from binarized TEM images using ImageJ program by commonly used box-counting method. By this method, the number of boxes needed to cover the object, $N(r)$, is counted using different box size r . Then the fractal dimension D_f can be obtained from the equation defined by

$$D_f = \lim_{r \rightarrow 0} \frac{\log N(r)}{\log(r)}$$

The box sizes of 2, 3, 4, 6, 8, 12, 16, 32, and 64 were used for the calculation.

3.6. Supporting information

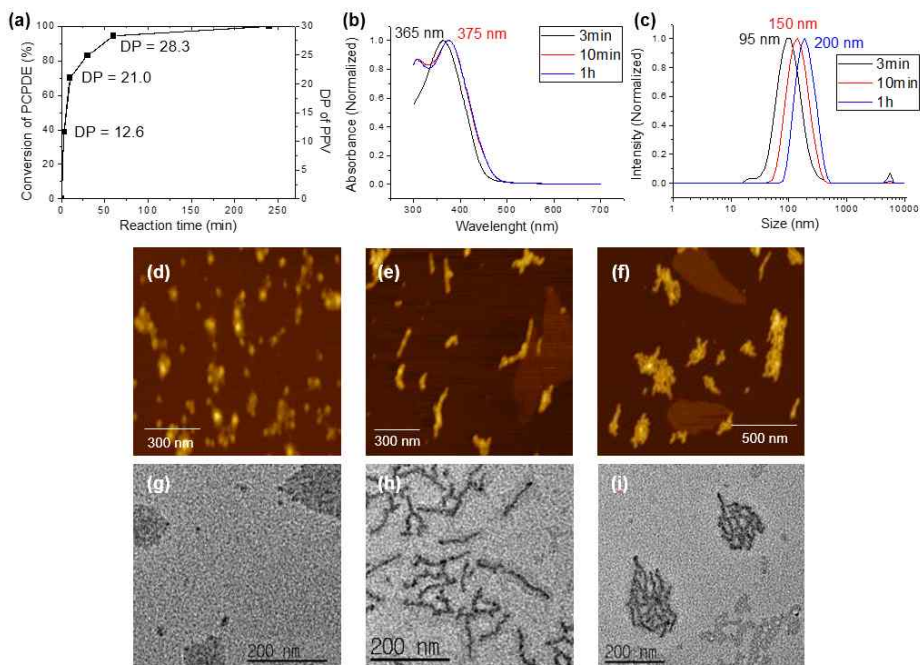


Figure S3.1. Analysis of samples taken during one-shot ROMP of PNBCyH-*b*-PPV with a monomer ratio of 50:30 ([NBCyH]:[PCPDE]). (a) PCPDE conversion plot. The conversions and average DP of PPV were measured by ^1NMR . UV/Vis absorbance (b), DLS profiles (c), and AFM and TEM images of samples taken at 3 min (d, g), 10 min (e, h) and 60 min (f, i) after initiation. The measured samples were prepared by taking aliquots during the polymerization at different times and then the samples were diluted in THF without any quenching or precipitation processes.

Table S3.1. Optical E_g , HOMO, and LUMO level calculated from the UV/vis spectra and CV spectra.

Polymer	Optical E_g (eV) ^a	HOMO (eV) ^b	LUMO (eV) ^c
P1	2.7	-5.6	-2.9
P2	2.6	-5.6	-3.0
P3	2.6	-5.6	-3.0

^acalculated from the onset point of the UV/vis spectra (Figure 3.8, a). ^bHOMO = -4.8-($E_{ox,onset}$ - $F_{C1/2}$) (Figure 3.9). ^cLUMO = HOMO + optical E_g

Table S3.2. Quantum efficiency (QE) of **P1-P3**

Polymer	External QE (%)	Internal QE (%)
P1	5.1	8.8
P2	9.6	14.2
P3	8.4	11.2

The above values were obtained by absolute QE measurement using integrating hemisphere technique (QE-1200, Otsuka Electronics) at the transmittance values between 0.2-0.6 at the λ_{max} .

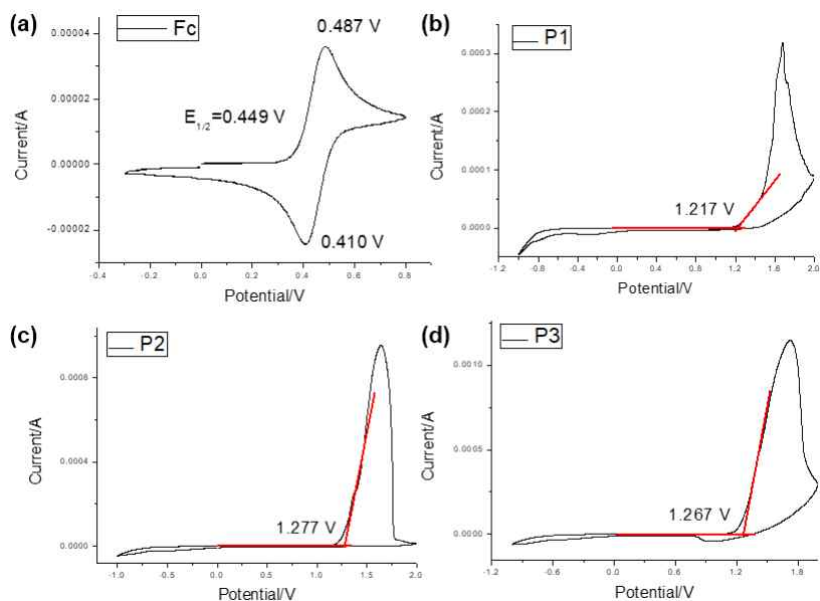


Figure S3.2. Cyclic voltammograms of (a) ferrocene standard (1 mM in acetonitrile) and (b-d) **P1-P3** (polymer film on the glassy carbon working electrode prepared by drop casting of the polymer solution with the concentration of 5 mg/ml). Ag/Ag⁺ (0.1M AgNO₃ in acetonitrile) reference electrode and platinum wire counter electrode were used at a scan rate of 100 mV/s.

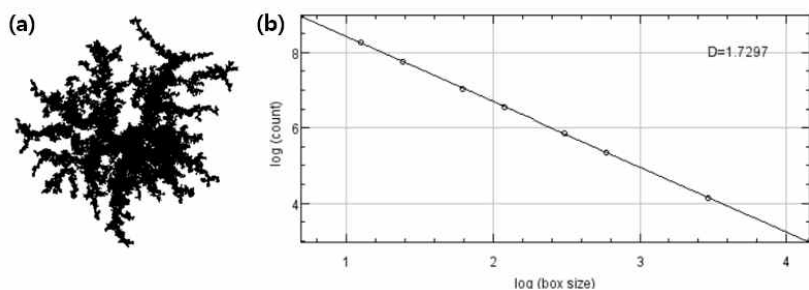


Figure S3.3. D_f measurement of the fractal structure. (a) Binarized TEM image of **P3**. (b) The box-counting plot from the binarized image. The slope indicated the D_f value of 1.7297.

3.7. References

[†]Portions of this chapter have been previously reported, see: (a) Shin, S.; Lim, J.; Gu, M.-L.; Yu, C.-Y.; Hong, M.; Char, K.; Choi, T.-L. *Polym. Chem.* **2017**, *8*, 7507. (b) Shin, S.; Gu, M.-L.; Yu, C.-Y.; Jeon, J.; Lee, E.; Choi, T.-L. *J. Am. Chem. Soc.* **2018**, *140*, 475.

(1) (a) Grubbs, R. H.; Conticello, V. P.; Gin, D. L. *J. Am. Chem. Soc.* **1992**, *114*, 9708. (b) Bunz, U. H. F.; Maker, D.; Porz, M. *Macromol. Rapid. Commun.* **2011**, *33*, 886. (c) Yu, C.-Y.; Turner, M. L. *Angew. Chem. Int. Ed.* **2006**, *45*, 7797.

(2) Miao, Y.-J.; Bazan, G. C. *Macromolecules* **1994**, *27*, 1063.

(3) (a) Khor, S. Y.; Truong, N. P.; Quinn, J. F.; Whittaker, M. R.; Davis, T. P. *ACS Macro Lett.* **2017**, *6*, 1013. (b) Zhou, W.; Qu, Q.; Xu, Y.; An, Z. *ACS Macro Lett.* **2015**, *4*, 495. (c) Zhou, D.; Dong, S.; Kuchel, R. P.; Perrier, S.; Zetterlund, P. B. *Polym. Chem.* **2017**, *8*, 3082. (d) Blackman, L. D.; Doncom, K. E. B.; Gibson, M. I.; O'Reilly, R. K. *Polym. Chem.* **2017**, *8*, 2860.

(4) (a) Yoon, K.-Y.; Lee, I.-H.; Choi, T.-L. *RSC Adv.* **2014**, *4*, 49180. (b) Lee, I.-H.; Choi, T.-L. *Polym. Chem.* **2016**, *7*, 7135.

(5) (a) Yoon, K.-Y.; Lee, I.-H.; Kim, K. O.; Jang, J.; Lee, E.; Choi, T.-L. *J. Am. Chem. Soc.* **2012**, *134*, 14291. (b) Yoon, K. Y.; Shin, S.; Kim, Y. J.; Kim, I.; Lee, E.; Choi, T. L. *Macromol. Rapid Commun.* **2015**, *36*, 1069.

(6) de Meijere, A.; Kozhushkov, S. I.; Rauch, K.; Schill, H.; Verevkin, S. P.; Kümmerlin, M.; Beckhaus, H.-D.; Rüchardt, C.; Yufit, D. S. *J. Am. Chem. Soc.* **2003**, *125*, 15110.

(7) Schleyer, P. v. R.; Williams, J. E.; Blanchard, K. R. *J. Am. Chem. Soc.* **1970**, *92*, 2377.

(8) Wang, H. Y.; Meng, X.; Jin, G. X. *Dalton Trans.* **2006**, *0*, 2579.

(9) Wang, F.; Xie, F. He, Z.; Li, M.; Hanif, M.; Gu, X.; Yang, B.;

- Zhang, H.; Lu, P.; Ma, Y. *J. Polym. Sci., Part A: Polym. Chem.* **2008**, *46*, 5242.
- (10) Kim, D. Y.; Grey, J. K.; Barbara, P. F. *Synth. Met.* **2006**, *156*, 336.
- (11) Lidster, B. J.; Kumar, D. R.; Spring, A. M.; Yu, C.-Y.; Turner, M. L. *Polym. Chem.* **2016**, *7*, 5544.
- (12) Zhong, Z.; Hu, Z.; Jiang, Z.; Wang, J.; Chen, Y.; Song, C.; Han, S.; Huang, F.; Peng, J.; Wang, J.; Cao, Y. *Adv. Electron. Mater.* **2015**, *1*, 1400014.
- (13) Yu, C.-Y.; Horie, M.; Spring, A. M.; Tremel, K.; Turner, M. L. *Macromolecules* **2010**, *43*, 222.
- (14) Kim, K. O.; Shin, S.; Kim, J.; Choi, T.-L. *Macromolecules* **2014**, *47*, 1351.
- (15) Falconer, K., Alternative Definitions of Dimension. In *Fractal Geometry*, John Wiley & Sons, Ltd: 2005; pp 39-58.
- (16) Nicolas-Carlock, J. R.; Carrillo-Estrada, J. L.; Dossetti, V. *Sci. Rep.* **2016**, *6*, 19505.
- (17) (a) Chen, H.; Pan, S.; Pang, X.; Feng, S.; Peng, C.; Xiong, Y.; Li, L.; Xiong, Y.; Xu, W. *J. Macromol. Sci. Part A* **2012**, *49*, 533. (b) Ramanathan, M.; Darling, S. B. *Soft Matter* **2009**, *5*, 4665. (c) Bracha, D.; Bar-Ziv, R. H. *J. Am. Chem. Soc.* **2014**, *136*, 4945.
- (18) (a) Tong, Z.; Zhang, R.; Ma, P.; Xu, H.; Chen, H.; Li, Y.; Yu, W.; Zhuo, W.; Jiang, G. *Langmuir* **2017**, *33*, 176. (b) Cao, H.; Yuan, Q.; Zhu, X.; Zhao, Y. P.; Liu, M. *Langmuir* **2012**, *28*, 15410.
- (19) (a) Nicolas-Carlock, J. R.; Carrillo-Estrada, J. L.; Dossetti, V. *Sci. Rep.* **2016**, *6*, 19505. (b) Witten, T. A.; Sander, L. M. *Phys. Rev. Lett.* **1981**, *47*, 1400. (c) Sander, L. M. *Contemp. Phys.* **2000**, *41*, 203.
- (20) (a) Meakin, P. *Phys. Rev. Lett.* **1983**, *51*, 1119. (b) Chishty, S. Q.; Farooqui, M.; Khizer, M.; Rajeshaikh, B. B. *Orient. J. Chem.* **2013**,

29, 1183.

(21) (a) Thomas, S. W.; Joly, G. D.; Swager, T. M. *Chem. Rev.* **2007**, 107, 1339. (b) Zhu, C.; Liu, L.; Yang, Q.; Lv, F.; Wang, S. *Chem. Rev.* **2012**, 112, 4687. (c) Grimsdale, A. C.; Chan, K. L.; Martin, R. E.; Jokisz, P. G.; Holmes, A. B. *Chem. Rev.* **2009**, 109, 897.

(22) Kang, E.-H.; Lee, I. S.; Choi, T.-L. *J. Am. Chem. Soc.* **2011**, 133, 11904.

Chapter 4.

One-shot block copolymerization and ultra-fast light-induced crystallization-driven self-assembly of Poly(*para*-phenylenevinylene-2,5-dimethoxy-*para*-phenylenevinylene) block copolymers

4.1. Abstract

Perfect one-shot block copolymerization of Polynorbornene-*b*-poly(*para*-phenylenevinylene-2,5-dimethoxy-*para*-phenylenevinylene) (PNB-*b*-MeO-PPV) was achieved by ring opening metathesis polymerization (ROMP) using norbornene (NB) derivatives and dimethoxy substituted [2.2]paracyclophane-1,9-diene (PCPDE) as comonomers. A coordination of a methoxy substituent to Ru propagating carbene during polymerization significantly retard the propagation rate of MeO-PPV, and then the polymerization of MeO-PPV proceeded after the 1st block monomer, NB, was fully consumed. Dimethoxy substituents also provided appropriate solubility to the PPV backbone, leading to light-induced crystallization-driven self-assembly (LI-CDSA) of PNB-*b*-MeO-PPV into micro-long fiber-like micelles containing a crystalline MeO-PPV core. These fiber-like micelles could grow in living manner, producing micelles having controlled length with narrow dispersity and ABA type triblock comicelles or gradient comicelles composed of segmented or gradual composition of shells. This LI-CDSA could be carried out in around 5 minutes using 5W white LED as a light source.

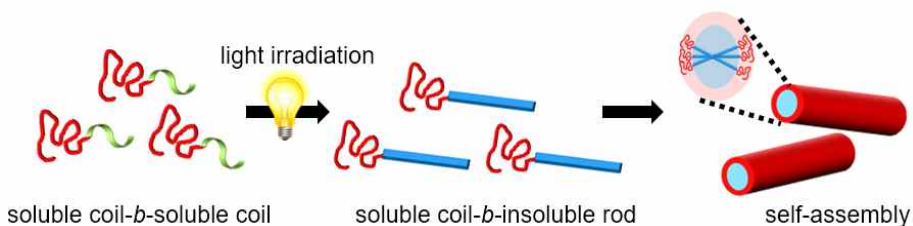
4.2. Introduction

Development of strategies for self-assembly of block copolymers (BCPs) in solution enabled preparation of various nanoparticles having desired shapes by precise control of properties of BCPs such as chemical structures, molecular weight, number and ratio of blocks, and physical properties, and also conditions of self-assembly such as solvents, temperature, pH, ionic strength, and concentration.¹ Crystallization-driven self-assembly (CDSA) is one of the breakthrough strategies for precise self-assembly of BCPs.² This method exploits crystallization of BCPs containing crystallizable block as the driving force for self-assembly, producing nanoparticles having “living” end. These properties make the CDSA process analogous to a living polymerization, leading to preparation of not only uniform structures with controlled size but also block micelles which have segmented composition. Furthermore, the block micelles composed of amphiphilic shells with controlled length can do secondary self-assembly to superstructures in a selective solvent. Thus, preparation of precisely controlled uniform polymer nanoparticles having complex architectures and compositions became possible.

In previous chapters, we could efficiently produce various nanoparticles composed of conjugated BCPs in one-step without post-synthetic treatments, exploiting strong π - π interaction of insoluble conjugated polymers. This strong interaction enabled generation of kinetically trapped structures stable under various conditions.³ However, this property also caused lack of crystallinity of cores and made it hard to generate well-ordered structures. For example, in Chapter 3, nanostructures prepared by poly(*para*-phenylenevinylene) (PPV) BCPs had amorphous PPV cores even though PPV is a crystallizable polymer.⁴ The high content of *cis* configuration of PPV synthesized by

ring-opening metathesis polymerization (ROMP) due to intrinsic structure of the monomer, [2.2]paracyclophane-1,9-diene (PCPDE),⁵ is another reason to prevent crystalline core formation during *in situ* nanoparticlization of PPV BCPs synthesized by ROMP. Even though *cis*-to-*trans* isomerization of PPV can be easily carried out by light irradiation,⁶ photoisomerization of core after formation of nanoparticles could not change the structures significantly because the structure was already trapped.⁷

In 2008, different solubility of phenyl-substituted PPV depending on the configuration was reported.^{6b} PPV having a high content of *cis*-olefin showed good solubility owing to the twisted, coiled configuration. After photoisomerization to *trans*-configuration, solubility of PPV decreased and the polymer was precipitated due to highly conjugated rod structure of *trans*-PPV, which facilitated the packing of the polymer chains. Inspired by this solubility change by isomerization, we envisioned a light-induced self-assembly of PPV BCPs, exploiting insoluble property after photoisomerization as the driving force for self-assembly (Scheme 4.1). In this chapter, we synthesized poly(*para*-phenylenevinylene-2,5-dimethoxy-*para*-phenylenevinylene) (MeO-PPV) BCPs by one-shot ROMP, which had good solubility after synthesis but became insoluble after photoisomerization to *trans* configuration due to appropriate solubility from dimethoxy substituents. All-*trans*-MeO-PPV BCPs in THF self-assembled into fiber-like-micelle having a crystalline core, enabling living-CDSA of BCPs. Notably, rapid photoisomerization of MeO-PPV in solution led to ultra-fast CDSA in a few minutes, with on-off control of growth of fiber-like-micelles by turning on and off the light.



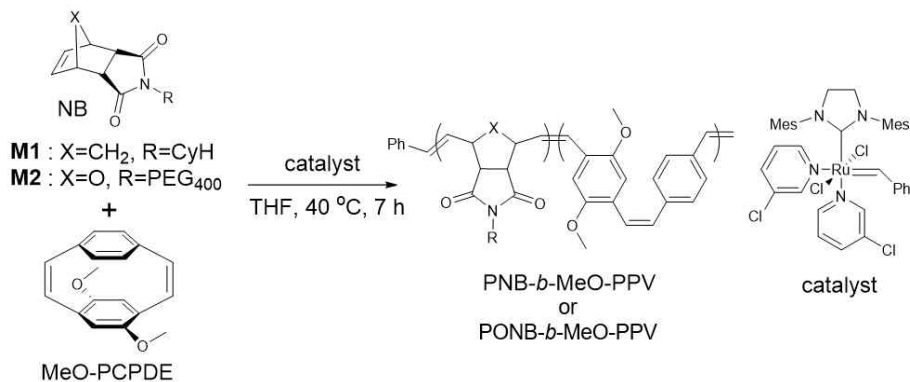
Scheme 4.1. Schematic representation of light-induced self-assembly.

4.3. Results and discussion

4.3.1. One-shot synthesis of perfect block copolymers and their self-assembly by photoisomerization

In chapter 3, non-substituted PPV block was insoluble even before isomerization to *trans*-configuration, and aggregated during polymerization. For successful LI-CDSA, *cis*-rich PPV block synthesized by ROMP should have good solubility, but it should become insoluble after light-induced isomerization to *trans*-dominant configuration, thereby triggering assembly into PPV crystalline core. Thus, we introduced short dimethoxy substituents to PPV for minimum solubility because large substituents would enhance the solubility of PPV even after isomerization. Additionally, we expected that the one-shot ROMP using norbornene (NB) derivatives and dimethoxy group substituted PCPDE (MeO-PCPDE) could improve block copolymer microstructure of PNB-*b*-MeOPP_V on that of BCPs synthesized by one-shot ROMP using NB and non-substituted PCPDE or cyclooctatetraene (COT), because coordination of methoxy group to Ru propagation carbene during propagation could further decrease the propagation rate of MeO-PPV.⁸

Table 4.1. Synthesis of PNB-*b*-MeO-PPV by one-shot ROMP using **M1**, **M2** and MeO-PCPDE.



Entry	NB	[NB]:[MeO-PCPDE]:[cat]	Conv. (%) ^a	Yield (%)	M _n (kDa) ^b	PDI ^b
1	M1	50:20:1	>99	98	25.7	1.13
2	M1	50:0:1	>99	97	17.6	1.03
3 ^c	M1	50:20:1	>99	98	24.1	1.08
4	M2	50:15:1	>99	95	29.5	1.22
5	M1	20:15:1	>99	90	11.3	1.13

^acalculated by ¹H NMR. ^bDetermined by THF SEC calibrated using polystyrene standards. ^cSynthesized by conventional sequential addition of two monomers.

Using fast-reacting NB monomer (**M1**) and MeO-PCPDE as comonomers and fast-initiating third-generation Grubbs catalyst, we tried one-shot ROMP of PNB₅₀-*b*-MeO-PPV₂₀ (Table 4.1, entry 1). The conversion of each monomer was monitored by *in situ* ¹H NMR at 0 °C for the detection of fast conversion of **M1**. Indeed, MeO-PCPDE was reacted after the full consumption of **M1**, producing PNB₅₀-*b*-MeO-PPV₁₅ with the perfect BCP microstructure (Figure 4.1, a). The propagation rate of **M1** was 574 times faster than that of MeO-PCPDE (Figure 4.1, b, 0.247 vs 0.00043). This confirmed that the

addition of substituents on PCPDE induced significant retardation of propagation resulting in sufficient reactivity difference between comonomers, compared to the one-shot ROMP from the mixture of **M1** and non-substituted PCPDE (6% conversion of PCPDE during 95% conversion of **M1** with 98 times faster propagation of **M1**) of COT (27% conversion of COT during 95% conversion of **M1** with 24 times faster propagation of **M1**), reported in Chapter 2 and 3. The size-exclusion chromatography (SEC) trace of the resulting PNB₅₀-*b*-MeO-PPV₂₀ in THF exhibited an unimodal signal without other signals from aggregates at high molecular weight region ($M_n = 25.7$ kDa, PDI = 1.13, Figure 4.1, c)³ indicating that the resulting BCP was dissolved in THF as single chain as we intended. Comparing this SEC trace with those of PNB₅₀ homopolymer ($M_n = 17.6$ kDa, PDI = 1.03, Table 4.1, entry 2) showing clear peak shift from the 1st block and of PNB₅₀-*b*-MeO-PPV₂₀ synthesized by conventional sequential addition of two monomers ($M_n = 24.1$ kDa, PDI = 1.08, Table 4.1, entry 3) showing two similar signals verified that the BCP was successfully prepared by one-shot ROMP. Another PONB₅₀-*b*-MeO-PPV₁₅ ($M_n = 29.5$ kDa, PDI = 1.22, Table 4.1, entry 4) showing good solubility in various solvents was prepared by one-shot ROMP using oxanorbornene (ONB) derivatives containing biocompatible polyethylene glycol (PEG, **M2**). This simple one-shot protocol to prepare BCPs containing easily functionalized PNB⁹ and fluorescent and semi-conducting PPV would further broaden the scope and preparation of functional polymer materials.

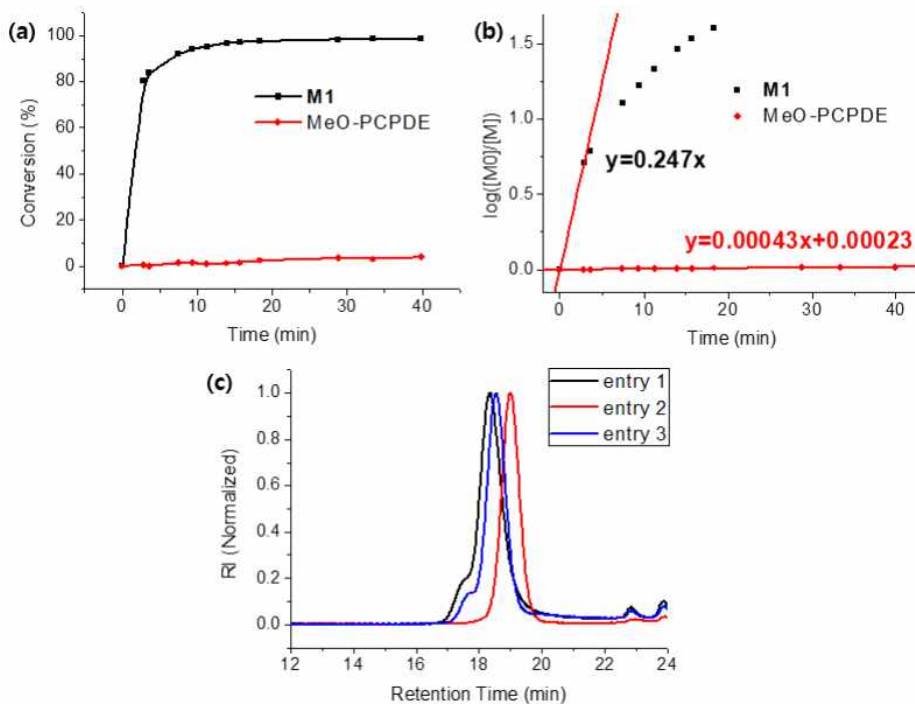


Figure 4.1. (a) Conversion vs. time and (b) logarithmic conversion vs. time plots for one-shot ROMP of **M1** and MeO-PCPDE at 0 °C with a feed ratio of $[M1]:[MeO-PCPDE] = 50:20$ at 0.1 M based on the concentration of MeO-PCPDE. (c) SEC traces of $PNB_{50}\text{-}b\text{-}MeO\text{-}PPV_{20}$ synthesized by one-shot ROMP (entry 1), PNB_{50} (entry 2), and $PNB_{50}\text{-}b\text{-}MeO\text{-}PPV_{20}$ synthesized by conventional sequential addition of monomers (entry 3).

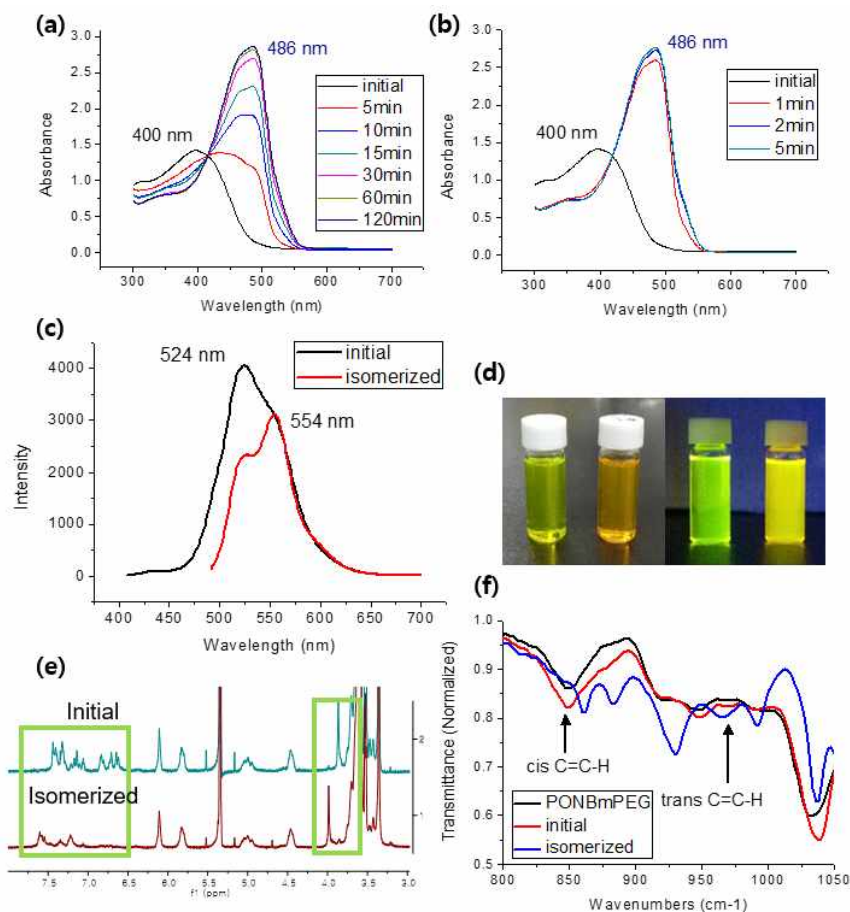


Figure 4.2. Various spectroscopic analysis of PONB₅₀-*b*-MeO-PPV₁₅ at 0.1 mg/ml in THF before and after photoisomerization. UV/vis absorbance spectra before and after (a) fluorescent light and (b) 5W white LED light irradiation for various time. (c) Fluorescent emission spectra. (d) Photographs of solution before (left vial) and after (right vial) isomerization (left) and those under UV light (right). (e) ¹H NMR spectra in *d*₂-DCM. (f) FT-IR spectra compared to PONB₅₀ homopolymer.

To demonstrate the feasibility of LI-CDSA, PONB₅₀-*b*-MeO-PPV₁₅ in THF (a good solvent for the both block) before and after photoisomerization was analyzed by various spectroscopic methods (Figure 4.2). First, UV/vis analysis indicated that the initial *cis*-rich MeO-PPV block successfully and rapidly isomerized to *trans*-dominant configuration showing red-shifted UV/vis absorbance spectrum (λ_{max} of 400 to 486 nm) in just 5 min of 5W LED exposure (Figure 4.2, b) while it took about 1 hour under fluorescent light (Figure 4.2, a). Fluorescent spectrum after isomerization exhibited a significant reduction of emission at 524 nm and a stronger emission peak at 554 nm compared to the initial BCP, implying some aggregation on self-assembly of BCPs after isomerization (Figure 4.2, c).¹⁰ This isomerization of MeO-PPV₁₅ block could be also visually identified by their color changes in solution, from yellow to orange and from green to yellow emission under UV lamp (Figure 4.2, d). Furthermore, this isomerization to *trans*-PPV was also confirmed by ¹H NMR and FT-IR spectra. ¹H NMR spectra showed disappearance and emergence of signals at 3.87 ppm and 4.00 ppm, respectively, corresponding to OCH₃ protons of methoxy group on a *cis*-rich MeO-PPV₁₅ and all-*trans*-MeO-PPV₁₅ (Figure 4.2, e).⁵ Also, aromatic proton signals (6.5-7.7 ppm) showed significant change shifting to downfield region. In addition, reduced integration of the signals to 56% (by setting the olefin signal from PONB₅₀ block as a standard) after isomerization implied for some self-assembly of BCPs forming cores made of MeO-PPV₁₅. Lastly, FT-IR spectra showing decreasing signal from *cis*-olefins (850 cm⁻¹) and increasing signal from *trans*-olefins (965 cm⁻¹) further confirmed the isomerization (Figure 4.2, f).^{6b}

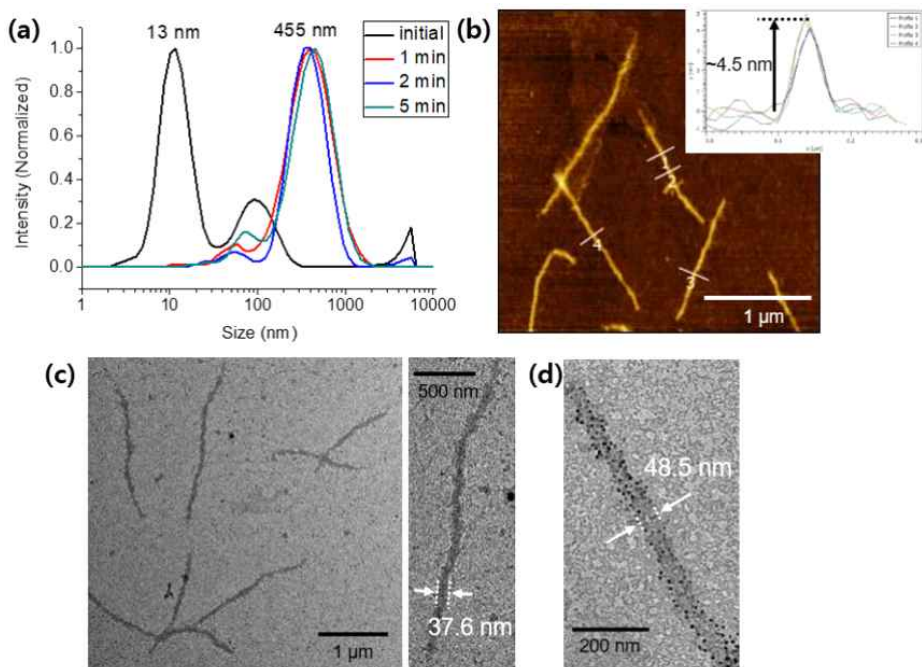


Figure 4.3. (a) DLS profiles of $\text{PONB}_{50}\text{-}b\text{-MeO-PPV}_{15}$ in THF at 0.1 mg/ml before and after LED irradiation for up to 5 mins. (b) AFM images of $\text{PONB}_{50}\text{-}b\text{-MeO-PPV}_{15}$ after isomerization in THF. Inset image showed height profiles along the white lines in AFM image. TEM images of $\text{PONB}_{50}\text{-}b\text{-MeO-PPV}_{15}$ after isomerization in THF (c) without staining and (d) after staining using aqueous solution of phosphotungstic acid.

Direct proof for the light-induced self-assembly of $\text{PONB}_{50}\text{-}b\text{-MeO-PPV}_{15}$ via isomerization was provided by dynamic light scattering (DLS) and imaging analysis. Before the isomerization, average hydrodynamic diameter (D_h) of the BCP in THF was 13 nm presumably reflecting the size of single polymer chains (Figure 4.3, a). But with irradiation of white LED over 1 minute, the D_h dramatically increased to over 450 nm. Atomic force microscopy (AFM) images

revealed that the $\text{PONB}_{50}\text{-}b\text{-MeO-PPV}_{15}$ after isomerization indeed self-assembled into fiber-like nanostructures with micrometer length and consistent height of 4.5 nm (Figure 4.3, b). The same nanofibers were also observed from transmission electron microscopy (TEM) images. The structures could be detected without staining process which only revealed the 2nd block of MeO-PPV_{15} core having width of 37.6 nm due to its high electron density of the conjugated block (Figure 4.3, c). After staining the shell on the 1st block using aqueous solution of phosphotungstic acid (1.0 mg/ml), the overall width increased to 48.5 nm (Figure 4.3, d).

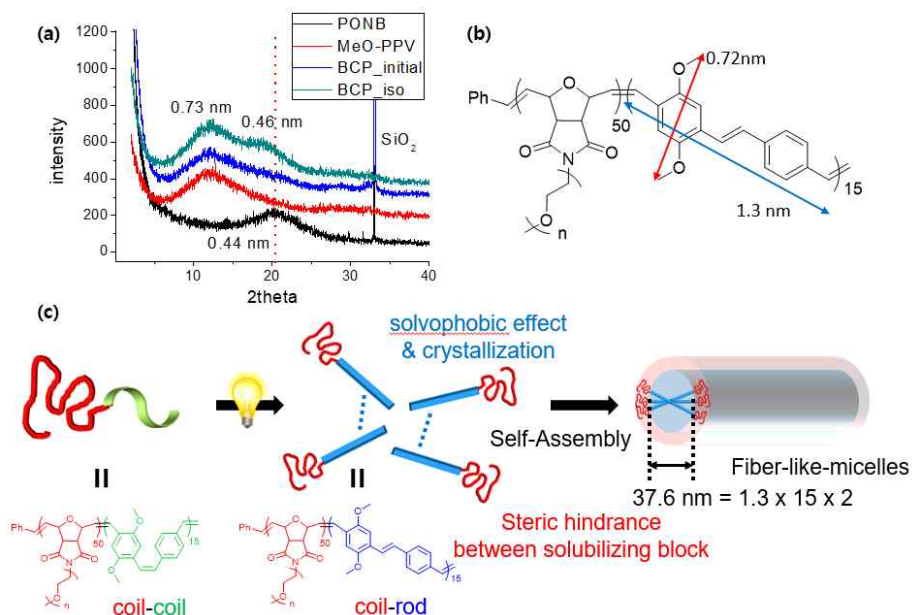


Figure 4.4. (a) Film XRD spectra of PONB_{50} , MeO-PPV_{15} homopolymers after isomerization, and $\text{PONB}_{50}\text{-}b\text{-MeO-PPV}_{15}$ before and after isomerization. (b) Estimated distance of *trans*- MeO-PPV repeat unit. (c) Proposed mechanism toward the formation of fiber-like micelles by light-induced crystallization-driven self-assembly of $\text{PONB}_{50}\text{-}b\text{-MeO-PPV}_{15}$.

To check crystallinity of the fiber-like micelles, film XRD spectra of the $\text{PONB}_{50}\text{-}b\text{-MeO-PPV}_{15}$ before and after isomerization were compared to those of PONB_{50} and isomerized MeO-PPV_{15} homopolymers (Figure 4.4, a). The absence of the signal from the interchain distance between PEG side chains of PONB_{50} (0.44 nm)¹¹ in the spectrum of $\text{PONB}_{50}\text{-}b\text{-MeO-PPV}_{15}$ indicated that the PONB_{50} shell formed an amorphous structure in the assembly structures. The signal at 0.73 nm observed from both MeO-PPV_{15} homopolymer and $\text{PONB}_{50}\text{-}b\text{-MeO-PPV}_{15}$ was in agreement with the distance between methoxy groups in one phenyl ring (Figure 4.4, b). After formation of fiber-like micelles by isomerization, a new signal appeared at 0.46 nm which was consistent with the reported PPV interchain distance during worm-like assembly structures,¹⁰ thereby supporting for LI-CDSA via photoisomerization.

Based on various analysis of $\text{PONB}_{50}\text{-}b\text{-MeO-PPV}_{15}$ during the isomerization, we propose a plausible mechanism for LI-CDSA (Figure 4.4, c). The MeO-PPV_{15} synthesized by ROMP has high content of *cis*-olefins, resulting in coil-coil BCP conformation and it is soluble in THF. After light irradiation, *cis*- MeO-PPV_{15} readily isomerizes to *trans*-configuration, and this rigidifies the backbone of MeO-PPV , thereby, decreasing solubility and increasing crystallinity. Such transformation from coil-coil to coil-rod BCP induces rapid self-assembly or epitaxial growth to nanofiber. Staggered stacking of BCPs may be favored due to large steric hindrance between shell on the 1st block, generating the core with width of 37.6 nm, matched with the twice value of the fully stretched *trans*- MeO-PPV_{15} . (Figure 4.3, c and 4.4, b and c).

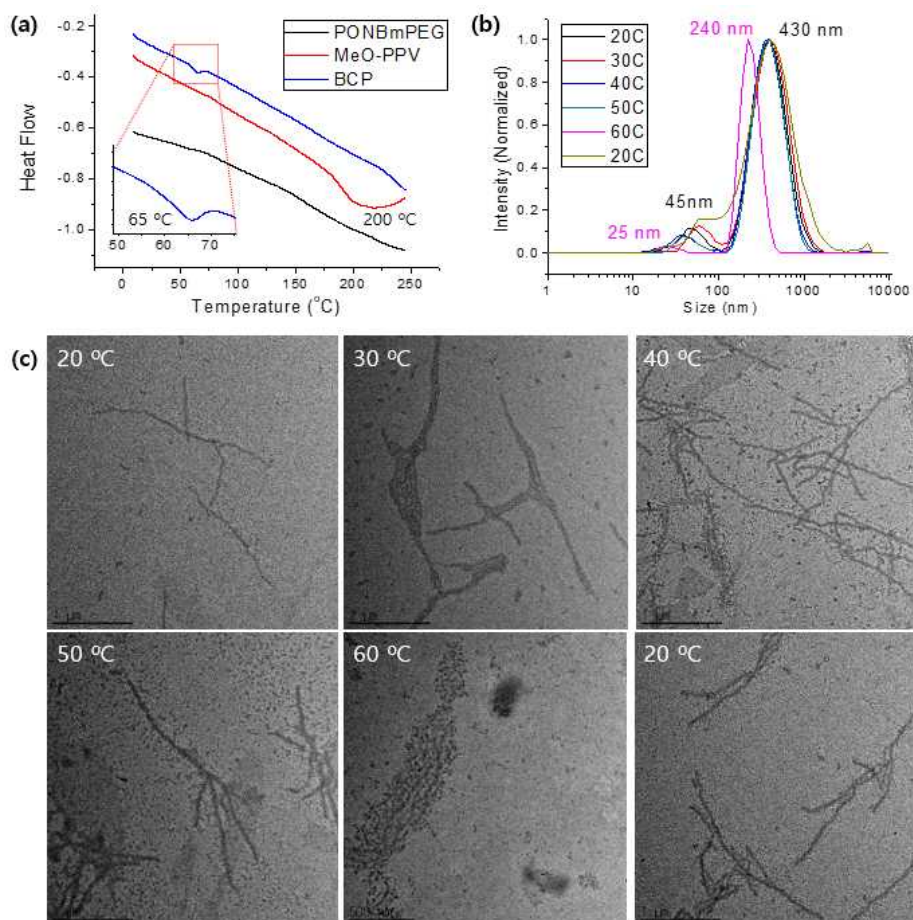


Figure 4.5. (a) DSC profiles of PONB₅₀, isomerized MeO-PPV₁₅, and isomerized PONB₅₀-b-MeO-PPV₁₅. (b) DLS profiles of isomerized PONB₅₀-b-MeO-PPV₁₅ in THF at 0.1 mg/ml at different temperatures. (c) TEM images of isomerized PONB₅₀-b-MeO-PPV₁₅ prepared at different temperatures.

Thermal stability of the fiber-like micelle was observed by differential scanning calorimetry (DSC) and DLS and TEM imaging at different temperatures (Figure 4.5). Slow heating (5 °C/min⁻¹, to 250 °C) of PONB₅₀-b-OMe-PPV₁₅ isomerized in THF exhibited transition

temperature around 65 °C, which was not observed from PONB₅₀ and OMe-PPV₁₅ homopolymers (Figure 4.5, a). We assumed that the transition temperature was originated from interaction of OMe-PPV₁₅ block at the core of the micelle, and carried out heating and cooling experiment of the THF solution of the nanofibers. DLS measurement showed decreasing D_h at 60 °C (from 430 nm to 240 nm, Figure 4.5, b) and the corresponding TEM image showed disassembly of micelle structures (Figure 4.5, c), supporting the fiber structures had phase transition around 60 °C.

4.3.2. Light-induced living crystallization-driven self-assembly

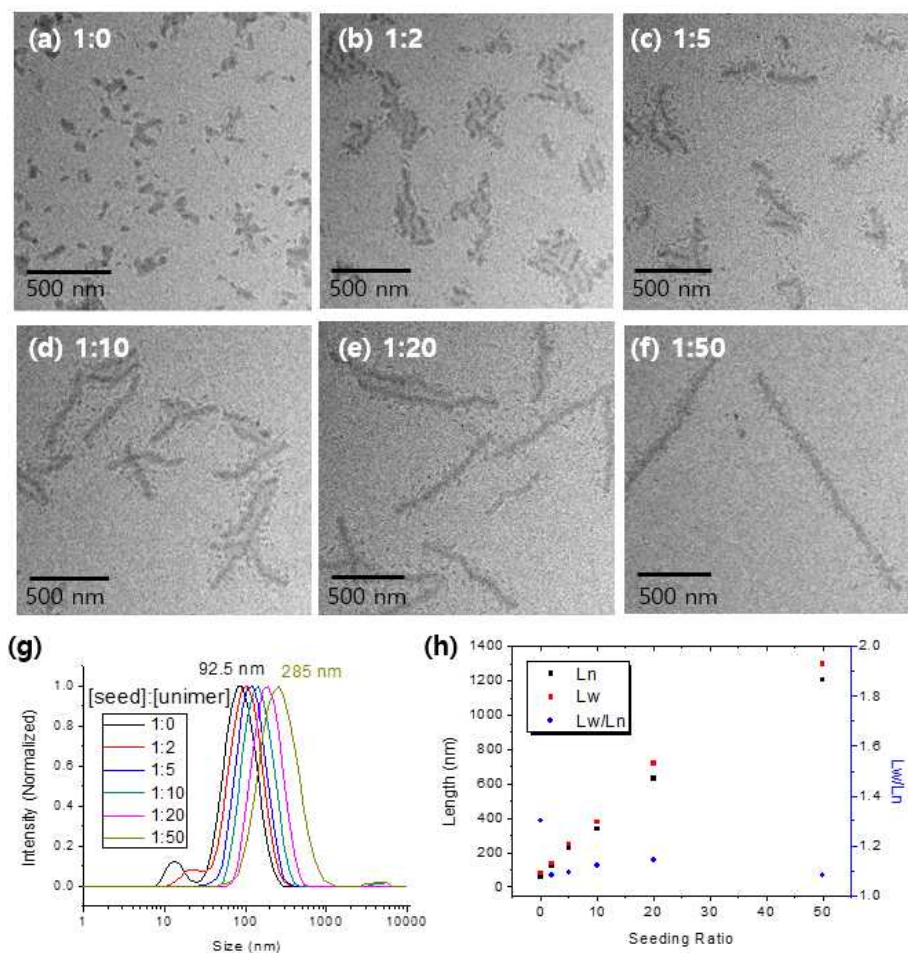


Figure 4.6. TEM images of fiber-like micelles prepared by 5 minutes of LED irradiation to a mixed solution of PONB₅₀-*b*-MeO-PPV₁₅ seed micelles and unimers with various ratio in THF (0.1 mg/ml). [unimer]/[seed] = (a) 1 (seed), (b) 2, (c) 5, (d) 10, (e) 20 and (f) 50. (g) DLS profiles of PONB₅₀-*b*-MeO-PPV₁₅ in THF at 0.1 mg/ml prepared by seeded growth with increasing unimer-to-seed ratios. (h) Plot of L_n , L_w and L_w/L_n values versus increasing unimer-to-seed ratios.

If the epitaxial growth via LI-CDSA was operative, we attempted light-induced seeded growth of $\text{PONB}_{50}\text{-}b\text{-MeO-PPV}_{15}$ to control the length of the fibers just like living polymerization by adding unimer of single polymer chain.² For seeded growth by CDSA, the seed micelles were prepared (Figure 4.6, a number average length, $L_n = 60$ nm, a weight average length, $L_w = 78$ nm, $L_w/L_n = 1.3$, $\sigma/L_n = 0.55$) by sonicating the THF solution of original nanofibers (0.1 mg/ml) at 0 °C for 30 min. Then, the unimer of $\text{PONB}_{50}\text{-}b\text{-MeO-PPV}_{15}$ at 0.1 mg/ml in THF without isomerization, was added to the solution of seed micelles with increasing unimer-to-seed ratio from 2 to 5, 10, 20 and 50. After irradiation of white LED for 5 minutes to each solution, DLS analysis indicated a gradual increase in D_h from 92.5 to 285 nm according to increasing unimer-to-seed ratio (Figure 4.6, g). More precisely, TEM images revealed that L_n of nanofiber linearly increased from 125, 227, 337, 631, to 1210 nm relative to the ratio as high as 50, and more surprisingly narrow length distribution ($L_w/L_n = 1.08\text{-}1.14$) were successfully obtained in all cases (Figure 4.6, a-f and h). In order to investigate the influence of isomerization temperature or rate on the controlled growth of the nanofibers, the same experiments were conducted at different temperatures (10 and 30 °C) using fluorescent light and 5W white LED as light sources. As a result, seeded growth was reproducible in these conditions (Figure S4.1-4.5), indicating that the LI-CDSA of $\text{PONB}_{50}\text{-}b\text{-MeO-PPV}_{15}$ was not sensitive to the isomerization condition. Therefore, we successfully controlled the seeded growth to obtain nanofibers with desired lengths and narrow length distribution by easy and rapid LI-CDSA of $\text{PONB}_{50}\text{-}b\text{-MeO-PPV}_{15}$ in just a few minutes at room temperature, as compared to other CDSA process which required long aging time at optimized temperature.²

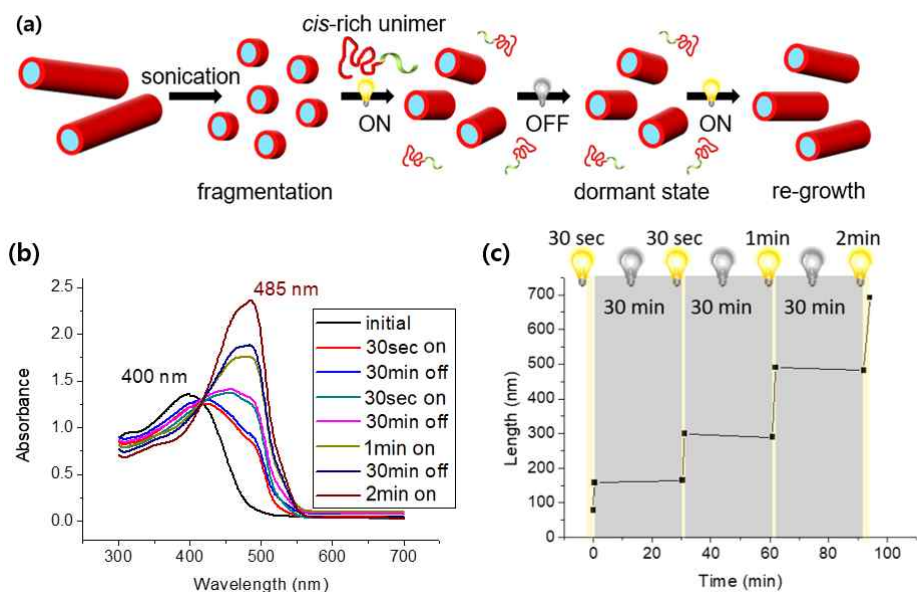


Figure 4.7. (a) Schematic illustration of nanofiber growth controlled by light on-off modulation via LI-CDSA. (b) UV/vis spectra of $\text{PONB}_{50}\text{-}b\text{-MeO-PPV}_{15}$ measured during light on-off cycles. (c) Plot of L_n versus time of light-on-off cycles (yellow regions: light on, grey regions: light off, light source: 5W white LED).

The living growth of nanofibers by irradiation brought up an idea of demonstrating the controlled growth by modulating light on-off just like the cases in light-induced living radical polymerization (LI-LRP).¹² In other word, turning on and off the light could control the degree of isomerization, driving force or trigger for self-assembly, and this should further control activation and deactivation of the seeded growth (Figure 4.7, a). The same seeded growth experiment of $\text{PONB}_{50}\text{-}b\text{-MeO-PPV}_{15}$ with unimer-to-seed ratio of 50 ($L_n = 69$ nm, $L_w = 77$ nm, $L_w/L_n = 1.13$, $\sigma/L_n = 0.36$) was repeated with multiple cycles of switching the light on and off. The LED was irradiated to the polymer solution for short period of time (30, 30, 60, and 120

seconds for each cycle) and was off for aging under dark condition for 30 minutes (Figure 4.7, c). The isomerization and seeded growth were monitored by UV/vis absorbance spectrum and TEM images, respectively, for each on-and-off cycles (5W white LED). LED Irradiation led to gradual red-shift in spectrum and increase in L_n of the nanofibers, but under dark condition, there was no sign changes in absorbance spectrum and the L_n of micelles indicating that suppression of CDSA and isomerization at dark (Figure 4.7, b and c). Then, repeating the on-and-off cycle of photoisomerization resulted stepwise increase in L_n from 69 to 158, 299, 490, and 692 nm while maintained its length at dark (Figure 4.7, c and S4.6).

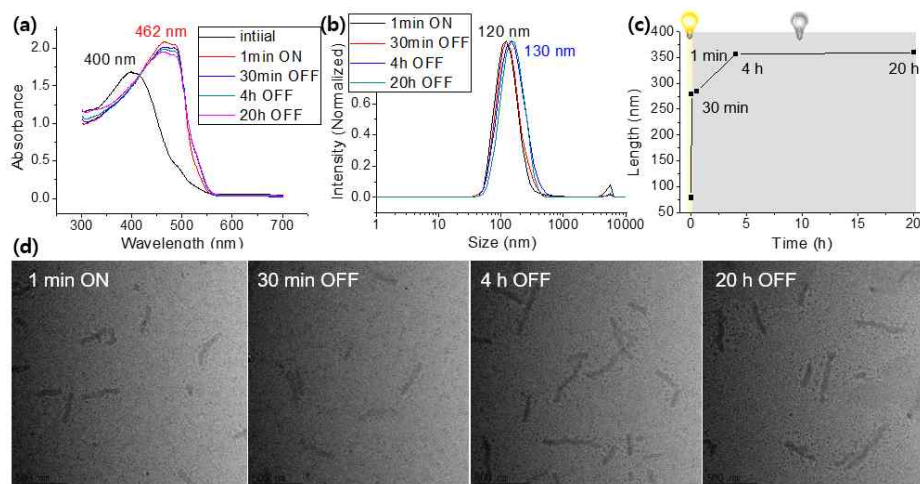


Figure 4.8. Various analysis of $\text{PONB}_{50}\text{-}b\text{-MeO-PPV}_{15}$ in THF after LED irradiation for 1 minutes followed by long-term aging at dark. (a) UV/vis spectra (b) DLS profiles (c) Plot of L_n versus time (yellow regions: light on, grey regions: light off) and (d) TEM images.

Long-term stability of partially isomerized nanofibers was examined by aging the THF solution of $\text{PONB}_{50}\text{-}b\text{-MeO-PPV}_{15}$ at dark

after LED irradiation for 1 minutes (Figure 4.8). Without light, UV/vis absorbance spectrum was not changed during long-term aging process, indicating configuration of MeO-PPV₁₅ was maintained without further photoisomerization (Figure 4.8, a). However, DLS measurement revealed that D_h increased slightly from 120 to 130 nm after aging over 4 hours (Figure 4.8, b). TEM images also exhibited slow increase in L_n of nanofibers from 279 nm (1 min irradiation) to 284, 357, and 360 nm according to 0.5, 4, and 20 hours of aging at dark, respectively (Figure 4.8, c and d). This result implied that the BCP had different crystallization rate depending on isomerization state or *cis-trans* ratio of PPV, thereby producing relatively short nanofibers rapidly with BCPs containing *trans*-rich PPV and then elongating the nanofibers slowly with BCPs containing less amount of *trans*-configuration. Therefore the seeded growth by LI-CDSA was driven by crystallization of photoisomerized PPV, and the living ends of micelles could be deactivated or become dormant state with much slower crystallization rate in the light-off state, which could be activated to grow rapidly again in the light-on state (Figure 4.7, a). Such on-off control on the seeded growth could provide a new platform to prepare precise hierarchical nanostructures.

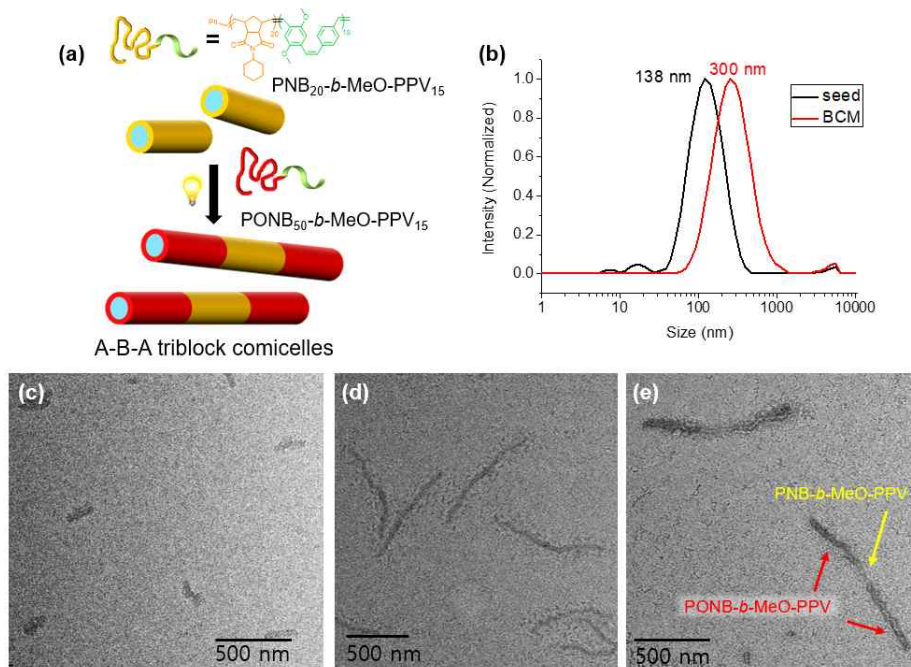


Figure 4.9. (a) Schematic illustration of the ABA triblock comicelles with a MeO-PPV core by seeded growth via LI-CDSA. (b) DLS profiles of seed micelles of $\text{PNB}_{20}\text{-}b\text{-MeO-PPV}_{15}$ and ABA triblock comicelles obtained by adding THF solution of $\text{PONB}_{50}\text{-}b\text{-MeO-PPV}_{15}$ to the seed micelles followed by LED irradiation. TEM images of (c) seed micelles of $\text{PNB}_{20}\text{-}b\text{-MeO-PPV}_{15}$ and ABA triblock comicelles (d) before and (e) after selective staining of PONB_{50} blocks by aqueous solution of phosphotungstic acid.

The living CDSA should enable preparation of block comicelles (BCMs) composed of two types of micelles having the same crystalline core but different outer shells (Figure 4.9, a).² Therefore, to prepare BCM by LI-CDSA, another micelles having the identical core but different shells composed of $\text{PNB}_{20}\text{-}b\text{-MeO-PPV}_{15}$ was prepared by one-shot ROMP ($M_n = 11.3$ kDa, PDI = 1.13, Table 4.1, entry 5)

followed by LED irradiation. After sonication to form seed micelles of PNB₂₀-*b*-MeO-PPV₁₅ ($L_n = 78$ nm, $L_w = 94$ nm, $L_w/L_n = 1.21$, $\sigma/L_n = 0.46$), seeded growth with unimer-to-seed ratio of 2 by LI-CDSA produced the initial short nanofibers as the another seed micelles for preparation of BCMs (Figure 4.9, c, $L_n = 218$ nm, $L_w = 255$ nm, $L_w/L_n = 1.17$, $\sigma/L_n = 0.42$). To these seed micelles, 4 equivalents of PONB₅₀-*b*-MeO-PPV₁₅ unimers were added by LED irradiation for 5 minutes. BCM was successfully prepared, which was confirmed by increase in D_h from 138 nm to 300nm by DLS measurement (Figure 4.9, b). Furthermore, TEM imaging also confirmed elongation of nanofibers from L_n of 218 to 802 nm (Figure 4.9, d, $L_w = 841$ nm, $L_w/L_n = 1.05$, $\sigma/L_n = 0.2$). Finally, selective staining on the PEG side chain of PONB₅₀ by aqueous solution of phosphotungstic acid showed a clear difference in electron density revealing darker fibers at the two ends than the unstained central block of comicelles (Figure 4.9, e). Additionally, measured L_n of the central block of the comicelles was almost identical to that of the initial seed micelles (Figure S4.9, about 220 nm) confirming that the ABA type triblock comicelles were successfully prepared by LI-CDSA of PONB₅₀-*b*-MeO-PPV₁₅ from PNB₂₀-*b*-MeO-PPV₁₅ seed micelles.

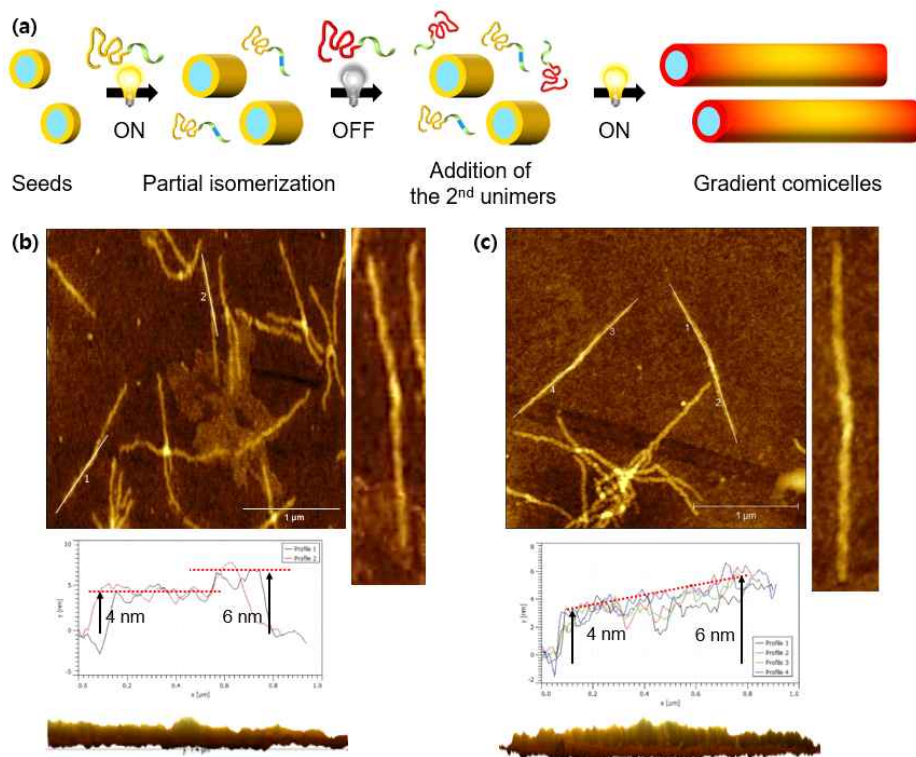


Figure 4.10. (a) Schematic illustration of preparing gradient comicelles by on-off controlled seeded growth via LI-CDSA. AFM images of ABA block comicelles (b) and gradient comicelles (c). Top left: full scale image, right: magnified image of individual comicelle, middle left: height profile along the white lines shown in full scale image, and middle bottom: 3D side view image.

Taking advantage of block comicelle preparation by living CDSA and on-off controlled seeded growth by LI-CDSA, we prepared gradient comicelle which had gradual composition of shell (Figure 4.10, a). Seeded growth of PNB₂₀-*b*-MeO-PPV₁₅ with unimer-to-seed ratio of 10 (using the same initial seed micelles which prepared for ABA block comicelles) by LI-CDSA was carried out with only 15 seconds LED

irradiation. Partial isomerization was confirmed by UV/vis absorbance spectrum, and generation of nanofibers was observed by DLS ($D_h = 260$ nm) and TEM image (Figure S4.10). To this mixture of nanofibers and partially isomerized unimers which did not self-assembled yet, 1 equivalent of $\text{PONB}_{50}\text{-}b\text{-MeO-PPV}_{15}$ unimers (seed: $\text{PNB}_{20}\text{-}b\text{-MeO-PPV}_{15}$: $\text{PONB}_{50}\text{-}b\text{-MeO-PPV}_{15} = 1:10:10$) was added followed by LED irradiation for 5 minutes. Fully isomerized BCPs confirmed by UV/vis absorbance spectrum produced elongated nanofibers, with D_h of 380 nm and L_n of 1120 nm (Figure S4.10 and S4.11, $L_w = 451$ nm, $L_w/L_n = 1.16$, $\sigma/L_n = 0.40$). Because of difficulty to distinguish gradient shell by TEM imaging even after selective staining on the PEG (Figure S4.10), AFM imaging was carried out. Height of the nanofibers composed of $\text{PNB}_{20}\text{-}b\text{-MeO-PPV}_{15}$ (~ 6 nm) was about 2 nm higher than that of $\text{PONB}_{50}\text{-}b\text{-MeO-PPV}_{15}$ (~ 4 nm, Figure S4.12), thereby enabling to distinguish composition of comicelles. As a result, the comicelles showed gradual height difference along the nanofibers with the lowest height (~ 4 nm) at the end and the highest height (~ 6 nm) at the center, which was different to the height profile of ABA block comicelles with clear height difference between each block (Figure 4.10, b and c). This result implied that the comicelles had gradually increasing composition of $\text{PNB}_{20}\text{-}b\text{-MeO-PPV}_{15}$ from end to center of nanofibers, due to faster photoisomerization and then self-assembly of partially isomerized $\text{PNB}_{20}\text{-}b\text{-MeO-PPV}_{15}$ than *cis*-rich $\text{PONB}_{50}\text{-}b\text{-MeO-PPV}_{15}$ which was added later.

4.4. Conclusion

In summary, ultra-fast LI-CDSA forming fluorescent nanofibers was successfully achieved by facile irradiation of light to the solution of PNB₅₀-*b*-MeO-PPV₁₅, which was easily prepared by simple one-shot ROMP. Introducing dimethoxy group on the PCPDE monomer not only improved the one-shot block copolymerization by slowing down its propagation by coordination to the catalyst, but also modulated solubility of the resulting 2nd block of MeO-PPV which was initially soluble but became insoluble after photoisomerization to trans configuration thereby enabling rapid self-assembly by light irradiation. Furthermore, living LI-CDSA was possible so that the length of the nanofibers was controlled linearly from 125 to 1210 nm with narrow distribution through the seeded growth at various unimer-to-seed ratio from 2 to 50. Notably, this seeded growth could be activated and deactivated by simply turning on and off the irradiated light, analogous to the LI-LRP. Taking advantage of living polymerization, ABA triblock comicelle and gradient comicelle were successfully prepared by seeded growth using two different BCPs. The scope of this self-assembly process can be broadened because all LI-CDSA was completed in a few minutes using 5W white LED and the BCPs were easily prepared by one-shot ROMP. In addition, since the shell block of PNB can be easily modified and the core contains fluorescent PPV, various functional polymeric materials with precise nanostructures and application can be designed.

4.5. Experimental section

Characterization

NMR spectra were recorded by Varian/Oxford As-500 (500 MHz for ^1H /125 MHz for ^{13}C) spectrometer. THF size exclusion chromatography (SEC) for polymer molecular weight analysis was carried out with Waters system (1515 pump, 2424 refractive index detector) and Shodex GPC LF-804 column eluted with THF (GPC grade, Honeywell Burdick & Jackson). The flow rate was 1.0 mL/min and temperature of the column was maintained at 35 °C. THF solution of polymers (0.1 mg/mL) was injected into GPC after filtration using a 0.20 μm PTFE filter. UV/vis spectra were obtained by a Jasco Inc. UV/vis spectrometer V-630, and fluorescence spectra were obtained by FP-8300 (Jasco Inc.). Dynamic light scattering (DLS) data were obtained by a Malvern Zetasizer Nano ZS. Film state X-ray diffraction (XRD) was performed by the National Instrumentation Center for Environmental Management (NICEM) at SNU using D8 Discover with GADDS (Bruker, Germany). IR spectra were measured on a Thermo Scientific Nicolet 6700 spectrometer. Multimode 8 and Nanoscope V controller (Veeco Instrument) were used for AFM imaging. All images were obtained on tapping mode using noncontact mode tip from Nanoworld (Pointprobe tip, NCHR type) with spring constant of 42 N m⁻¹ and tip radius of ≤ 8 nm.

Materials

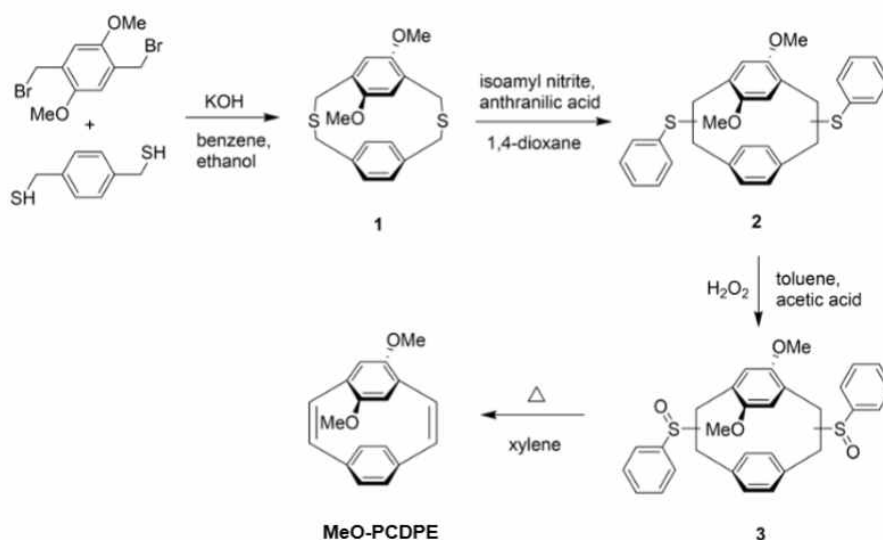
All reagents were commercially available from Acros, Alfa, Sigma Aldrich and TCI and used without further purification unless specified otherwise. All polymerizations were carried out under dry argon atmospheres using standard Schlenk techniques. THF was distilled over sodium and benzophenone and anhydrous deuterium THF solvent (\geq

99.95 %) were purchased from Euriso-Top[®]. THF solvents were degassed by argon bubbling for 10 minutes before using on polymerization. The third generation Grubbs catalyst was prepared by the reported method.¹³

Synthesis of monomers

ONB was prepared through previously reported procedures.⁹

Synthesis of 4,7-dimethoxy[2,2]paracyclophane-1,9-diene (MeO-PCPDPE)



Scheme 4.2. Synthetic routes to 4,7-dimethoxy[2,2]paracyclophane-1,9-diene.

Synthesis of 4,7-dimethoxy-2,11-dithia[3,3]-paracyclophane (1)

A deoxygenated mixture of 1,4-bis(bromomethyl)-2,5-dimethoxybenzene (2.52 g, 14.7 mmol) and 1,4-bis(thiolatomethyl)benzene (4.80 g, 14.8 mmol) in benzene (660 mL) was added dropwise to a solution of KOH (3.98 g, 71.1 mmol) in ethanol (530 mL) under a nitrogen atmosphere

for a period at least 72 hours. After a further 2 hours, the solvent was evaporated and the residue was extracted with HCl and DCM. The organic layers were combined, washed by water, dried with anhydrous MgSO_4 , filtered and evaporated. The residue were purified by column chromatography with using DCM:hexane (2:1) as the eluent. The cyclic compound was obtained as white solids in a yield of 53%. ^1H NMR (400 MHz, CDCl_3): δ 6.90-6.98 (m, 4H), 6.46 (s, 2H), 4.23-4.26 (d, 2H), 3.74-3.85 (m, 10H), 3.35-3.39 (d, 2H). HRMS (EI, $[\text{M}]^+$): calculated for $[\text{C}_{18}\text{H}_{21}\text{O}_2\text{S}_2]^+$: m/z 332.0905, found m/z 332.0906.

Synthesis of bis(sulfide) compounds (2)

Isoamyl nitrite (5.84 mL, 43.5 mmol) was added dropwise into a solution of anthranilic acid (3.50 g, 25.5 mmol) 4,7-dimethoxy-2,11-dithia[3,3]-paracyclophane (2.43 g, 7.3 mmol) in anhydrous 1,4-dioxane (190 mL) under reflux and a nitrogen atmosphere without light at least 15 minutes. The reaction mixture was boiled under reflux for another 3 hours. After the reaction mixture was concentrated under reduced pressure, the residue was purified by column chromatography using a solvent system of DCM and hexane (1:4). The cyclic compound was obtained as yellow solids in a yield of 43%. ^1H NMR (400 MHz, CDCl_3): δ 7.37-7.46 (m, 4H), 7.14-7.18 (m, 4H), 7.08-7.14 (m, 2H), 6.40-6.85 (m, 4H), 5.75-6.31 (m, 2H), 4.84-5.38 (m, 2H), 3.66-3.79 (m, 8H), 2.36-2.79 (m, 2H). HRMS (EI, $[\text{M}]^+$): calculated for $[\text{C}_{30}\text{H}_{29}\text{O}_2\text{S}_2]^+$: m/z 484.1531, found m/z 484.1528.

Synthesis of bis(sulfoxide) compounds (3)

Hydrogen peroxide (0.75 mL, 34.5wt%) was added dropwise to the solution of compound 2 (1.66 g, 3.43 mmol) in toluene (88 mL) and acetic acid (28 mL) at 0 °C under a nitrogen atmosphere over a period

of 20 minutes. The mixture was allowed to warm up to room temperature and stirred for additional 18 hours. The resulting solution was then extracted successively with brine and DCM, dried with MgSO_4 and concentrated to give pale yellow oil in an overall yield of 99%. The compounds contain a large number of stereoisomers and were used as starting materials for the next step without purification. ^1H NMR (400 MHz, CDCl_3): δ 7.70-7.79 (m, 4H), 7.51-7.60 (m, 4H), 7.18-7.21 (m, 2H), 6.44-6.77 (m, 4H), 5.32-6.14 (m, 2H), 4.65-4.78 (m, 2H), 3.53-3.74 (m, 8H), 2.78-2.93 (m, 2H). HRMS (EI, $[\text{MH}]^+$): calculated for $[\text{C}_{30}\text{H}_{29}\text{O}_4\text{S}_2]^+$: m/z 516.1429, found m/z 517.1509.

Synthesis of 4,7-dimethoxy[2,2]paracyclooctaphane-1,9-diene (MeO-PCPDE)

A solution of compound 3 in xylene was refluxed under a nitrogen stream for 20 hours. The solution was cooled to room temperature and extracted successively with dilute aqueous HCl and DCM, dried with anhydrous MgSO_4 , filtered and concentrate. The crude compound was then chromatographed over silica gel using DCM:hexane (1:6) for elution and gave compound OMe-PCPDE as white solids in a yield of 25%. ^1H NMR (400 MHz, CDCl_3): δ 7.15-7.16 (d, 2H), 6.92-6.94 (d, 2H), 6.81-6.83 (m, 2H), 6.47-6.50 (m, 2H), 5.80 (s, 2H), 3.69 (s, 2H). ^{13}C NMR (100 MHz, CDCl_3): δ 152.42, 137.82, 135.60, 133.84, 130.93, 127.05, 126.58, 118.76, 55.61. HRMS (EI, $[\text{M}]^+$): calculated for $[\text{C}_{18}\text{H}_{17}\text{O}_2]^+$: m/z 264.1150, found m/z 264.1154.

General procedure for the one-shot INCP of PNB-*b*-MeO-PPV and PONB-*b*-MeO-PPV

Both comonomers (25.2-62.8 μ mol for **M1** or **M2** and 18.9-25.2 μ mol for MeO-PCPDE) were weighed into a 2 mL sized screw-cap vial with a septum and purged with argon. Anhydrous and degassed THF was added (160-230 μ L) to the vial. THF solution of the third-generation Grubbs catalyst (1.26 μ mol) was added (20 μ L) to the monomer solution at once under vigorous stirring. The mixture was stirred for 7 h at 40 °C. The reaction was quenched by excess ethyl vinyl ether. The crude mixture was precipitated into methanol (Table 4.1, entry 1-3 and 5) or cold ether at -78 °C (Table 4.1, entry 4), and the obtained powder or sticky gel was dried *in vacuo*.

Poly(NBCyH)-*b*-poly(MeO-PCPDE) one-shot copolymers

Yield: 90-98% (see Table 4.1). ^1H NMR (500 MHz, CDCl_3): δ 7.01-7.42 (m), 6.61-6.82 (m), 5.76 (m), 5.47-5.52 (m), 3.87 (s), 3.44-3.51 (m), 3.27 (s), 2.67-3.04 (m), 2.12 (m), 1.81 (s), 1.58-1.64 (m), 1.21-1.29 (m). ^{13}C NMR (125 MHz, CDCl_3): δ 178.5, 151.8, 150.9, 134.0, 132.2, 131.9, 130.1, 129.5, 126.4, 113.3, 109.0, 56.1, 52.5, 51.6, 50.8, 46.2, 42.4, 41.0, 29.0, 26.1, 25.3.

Poly(ONBmPEG)-*b*-poly(MeO-PCPDE) one-shot copolymer

Yield: 95% (see Table 4.1). ^1H NMR (500 MHz, CDCl_3): δ 6.99-7.40 (m), 6.57-6.80 (m), 6.08 (s), 5.75-5.78 (d), 4.94-5.01 (m), 4.44 (s), 3.85 (s), 3.42-3.65 (m), 3.37 (s). ^{13}C NMR (125 MHz, CDCl_3): δ 175.6, 151.9, 150.9, 132.0, 131.1, 129.5, 127.6, 126.3, 113.6, 109.1, 81.1, 72.1, 70.7, 70.1, 67.0, 59.2, 56.0, 53.6, 52.7, 38.3, 29.8.

***In Situ* ^1H NMR Analysis of one-shot ROMP using NB and MeO-PCPDE**

157 μmol of NB and 62.8 μmol of MeO-PCPDE and hexamethyldisilane (~ 3 mg, an internal standard) were added into NMR tube and purged with argon. Anhydrous and degassed deuterated THF was added (550 μL) to the NMR tube and stabilized at 0 $^\circ\text{C}$ in NMR instrument. Then, the initial ratio of all compounds was measured by ^1H NMR analysis. After that, the solution of the third-generation Grubbs catalyst (3.14 μmol , 70 μL , 0 $^\circ\text{C}$) was added and the conversion of the two monomers was monitored by every 25 seconds. The measurement was done by Avance-500 (500 MHz for ^1H , Bruker, Germany) in the National center for Inter-University Research Facilities (NCIRF) at SNU.

Atomic force microscopy (AFM)

The atomic force microscopy experiments were performed with a thin film prepared by spin-coating one drop of the polymer solution (~ 0.05 mg polymer/mL, THF: spinning rate = 3000 rpm for 30 sec). The solvent was filtered by 0.2- μm PTFE filter before making the solution. The thin films were prepared on glass substrates. All images were obtained on tapping mode using non-contact mode tips from Nanoworld (Pointprobe tip, NCHR type) with spring constant of 42 N m^{-1} and tip radius of ≤ 8 nm.

Transmission electron microscopy (TEM)

Dry-TEM and cryo-TEM imaging were performed by JEM-2100 operated at 120 kV and SC 1000 CCD camera (Gatan Inc.). The samples for dry-TEM imaging were prepared by spin-coating one drop of the polymer solution (~ 0.1 mg polymer/mL, THF: spinning rate =

3000 rpm for 10 sec) on the carbon-coated copper grid. For the samples stained by phosphotungstic acid, one drop of phosphotungstic acid aqueous solution (1.0 mg/ml) was added onto the dried grid surface with samples, and most of the solution on the grid was absorbed by filter paper after 1 minute and the the grid was dried at room temperature. For each sample, length distributions of fiber-like micelles were calculated by measuring about 100 structures using Gatan Digital Micrograph software. Values of the number-average L_n and L_w of micelles were calculated as follows.

$$L_n = \frac{\sum_{i=1}^N N_i L_i}{\sum_{i=1}^N N_i} \quad L_w = \frac{\sum_{i=1}^N N_i L_i^2}{\sum_{i=1}^N N_i L_i}$$

where N_i is the number of micelles of length L_i , and N is the number of calculated micelles in each sample. The distribution of micellar length is characterized by both L_w/L_n and the standard deviation of the length distribution σ .

LI-CDSA of and seeded growth of nanofibers

PONB-*b*-MeO-PPV or PNB-*b*-MeO-PPV diblock copolymer was dissolved in THF (0.1 mg/mL) and kept the solution under the light using fluorescent light (for 2 hours) or 5W white LED (for 5 minutes) as the light source at different temperatures. For seeded growth, Seed micelles were prepared by sonicating the original long nanofibers (0.1 mg/mL) at 0 °C for 30 min. Different aliquots (1, 1.5, 2, 2, and 1.5 mL) of a THF solution of MeO-PPV block copolymers (0.1 mg/mL) were added into a seed solution (0.1 mg/ml, 0.5, 0.3, 0.2, 0.1, and 0.03 ml, respectively). The samples were kept under the light using fluorescent light (for 2 hours) or 5W white LED (for 5 minutes) as the light source at different temperatures.

4.6 Supporting information

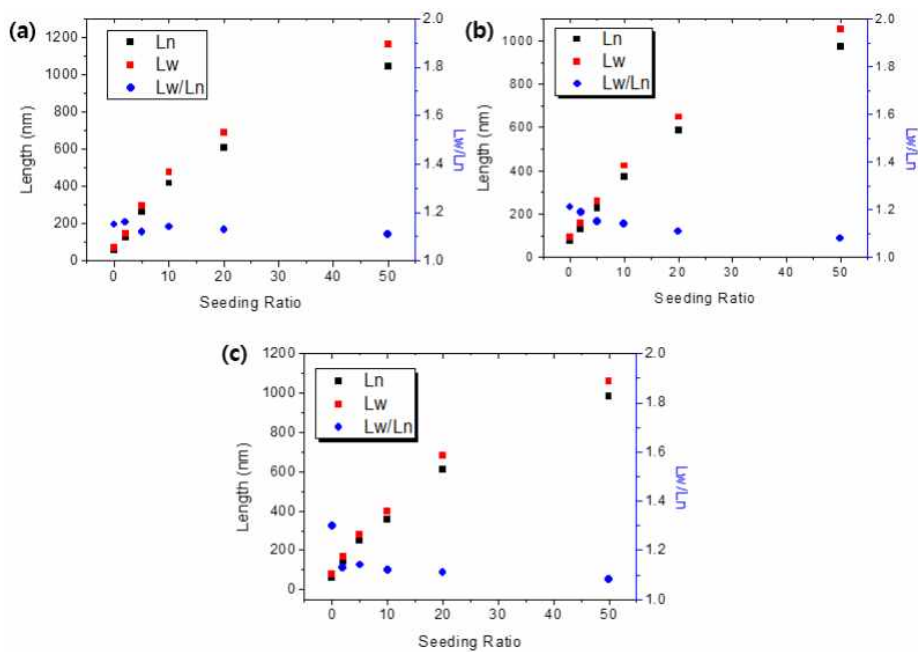


Figure S4.1. L_n , L_w and L_w/L_n values versus increasing unimer to seed ratios of light-induced seeded growth of PONB-*b*-MeO-PPV at 10 °C under (a) fluorescent light and (b) 5W white LED, and (c) at 30 °C under fluorescent light.

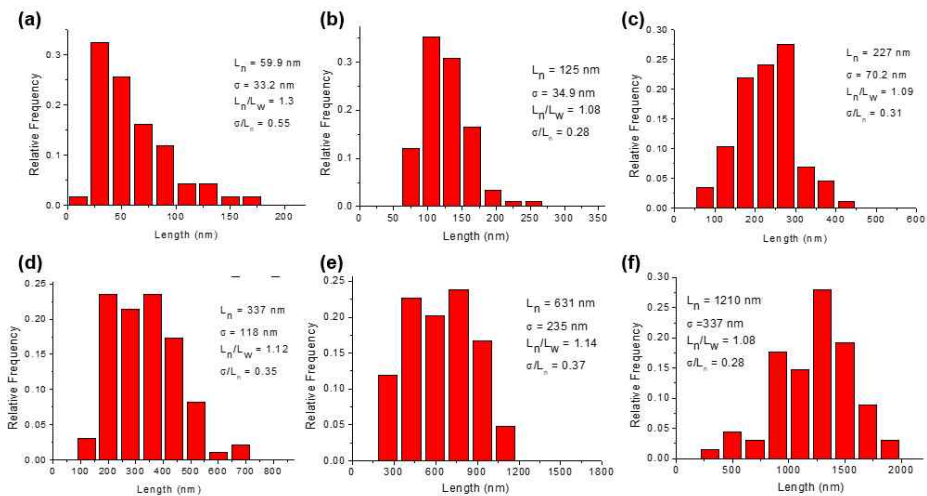


Figure S4.2. Contour length distributions of fiber-like micelles of PONB-*b*-MeO-PPV prepared by seeded growth using seed to unimer ratios of (a) 1:0, (b) 1:2, (c) 1:5, (d) 1:10, (e) 1:20, and (f) 1:50 by using 5W LED as the light source at room temperature.

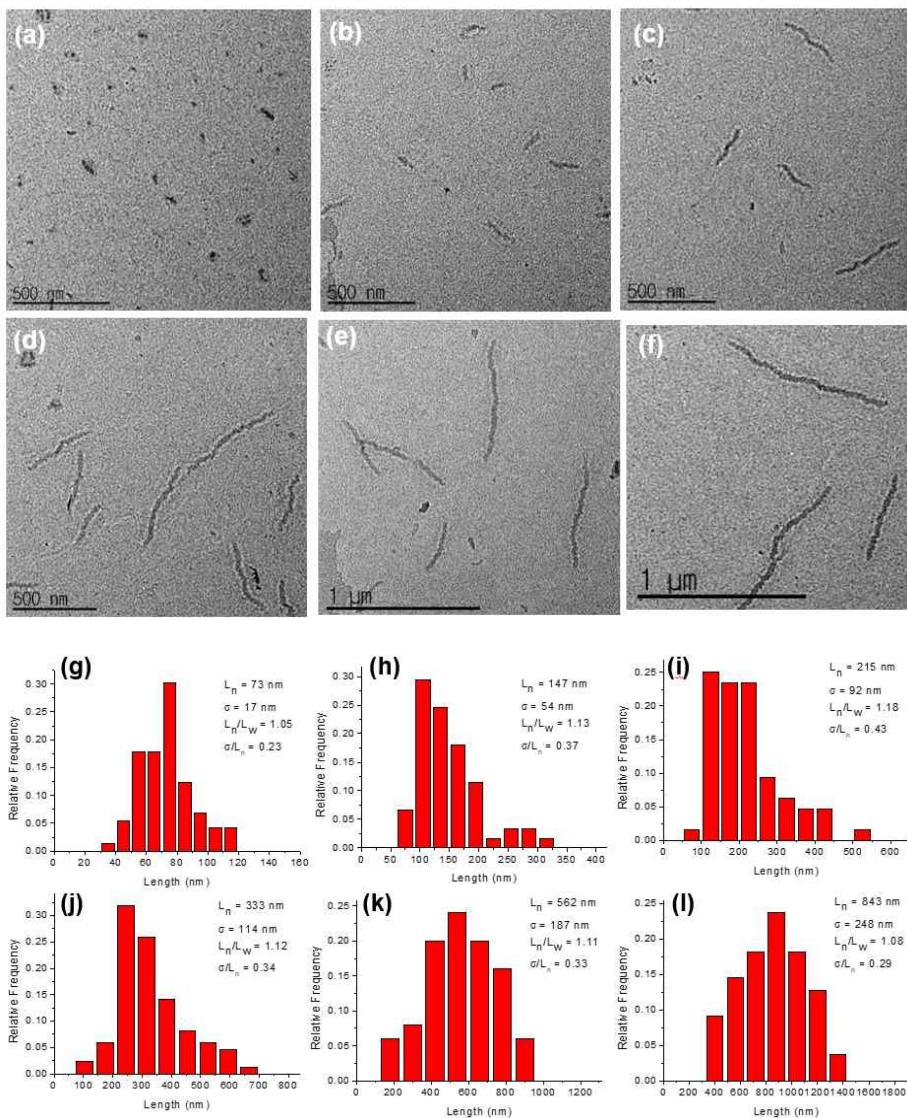


Figure S4.3. TEM images (a-f) and contour length distributions (g-l) of fiber-like micelles of PONB-*b*-MeO-PPV prepared by seeded growth using seed to unimer ratios of 1:0, 1:2, 1:5, 1:10, 1:20, and 1:50, respectively, by using fluorescent light as the light source at 10 °C.

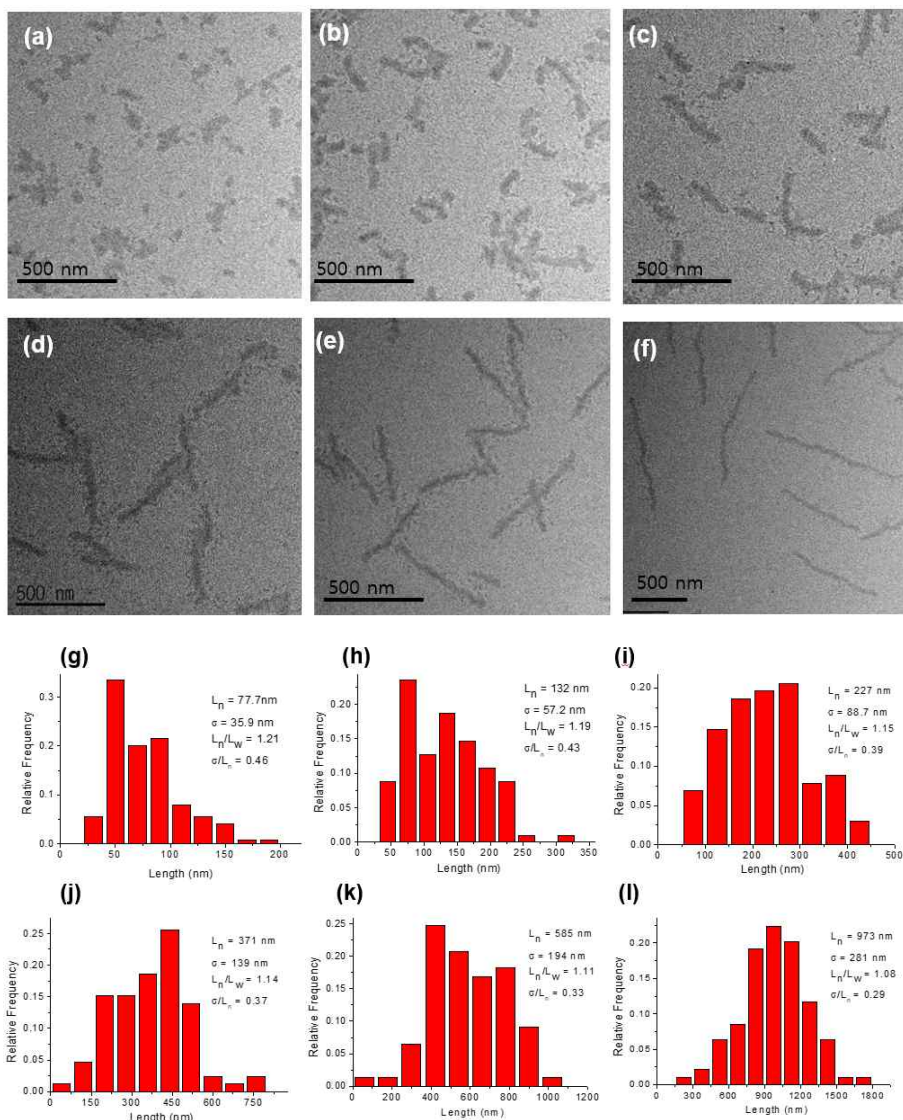


Figure S4.4. TEM images (a-f) and contour length distributions (g-l) of fiber-like micelles of PONB-*b*-MeO-PPV prepared by seeded growth using seed to unimer ratios of 1:0, 1:2, 1:5, 1:10, 1:20, and 1:50, respectively, by using 5W white LED as the light source at 10 °C.

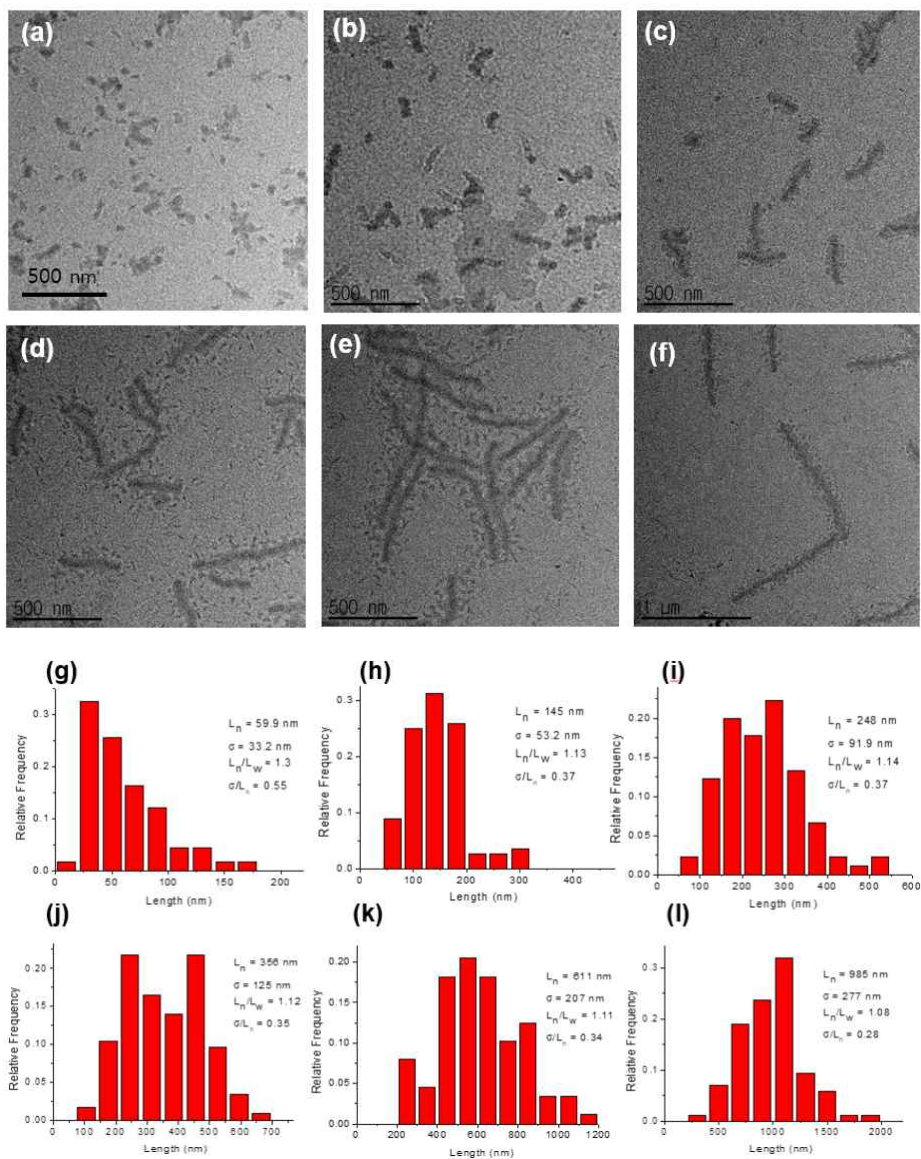


Figure S4.5. TEM images (a-f) and contour length distributions (g-l) of fiber-like micelles of PONB-*b*-MeO-PPV prepared by seeded growth using seed to unimer ratios of 1:0, 1:2, 1:5, 1:10, 1:20, and 1:50, respectively, by using fluorescent light as the light source at 30 °C.

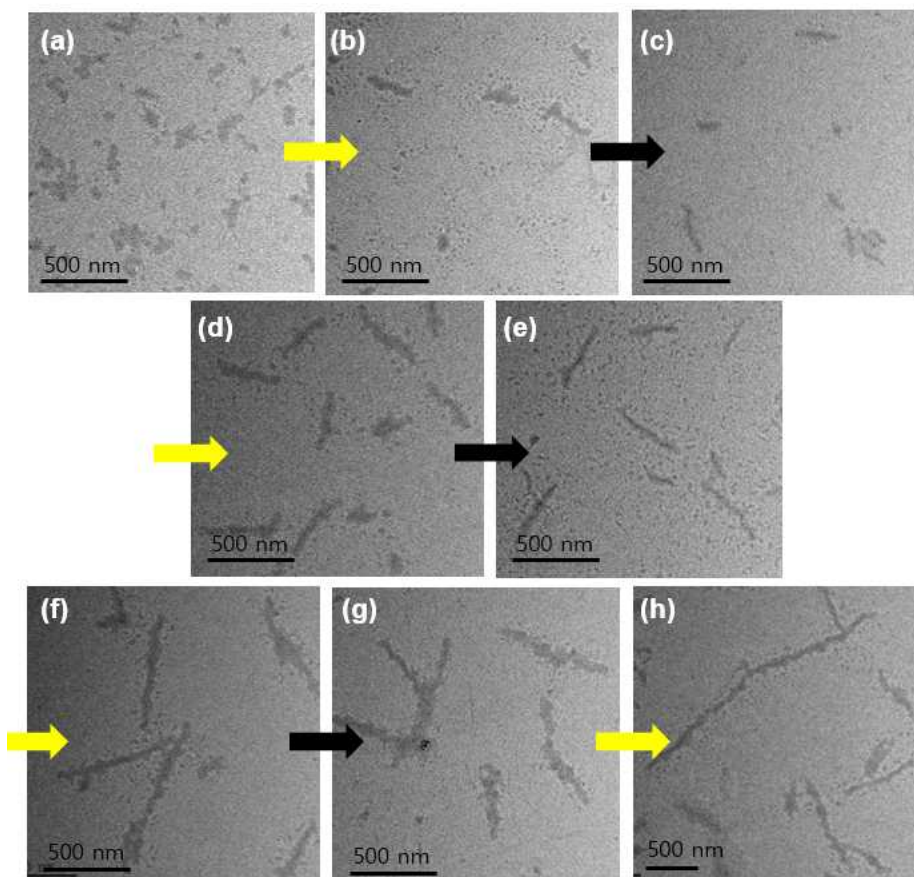


Figure S4.6. TEM images of fiber-like micelles of PONB-*b*-MeO-PPV prepared by seeded growth using seed to unimer ratios of 1:50 with irradiation of 5W white LED light for different time scales, (a) 0sec (initial seed), (b) 30 sec under light, (c) 30 min without light, (d) additional 30 sec under light, (e) 30 min without light, (f) additional 1 min under light, (g) 30 min without light, and (h) additional 2 min under light. Yellow arrows indicated light irradiation and black arrows indicated absence of light.

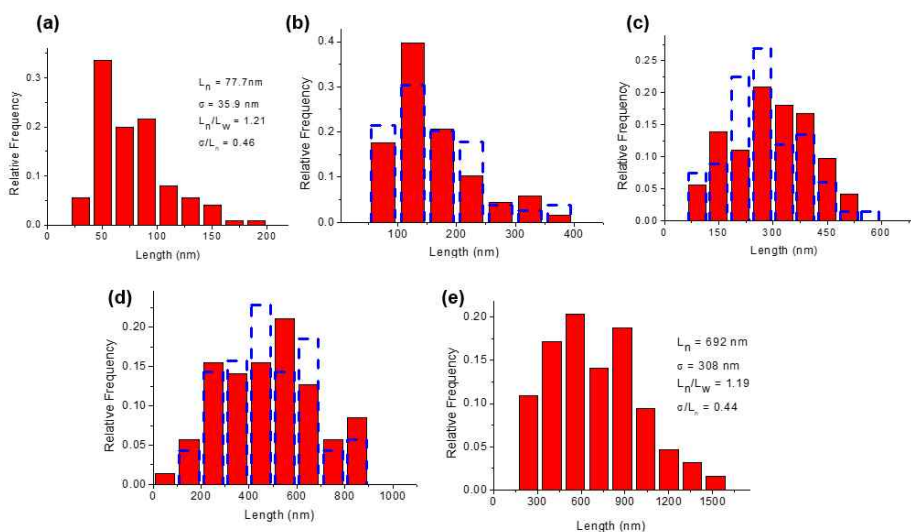


Figure S4.7. Contour length distributions of fiber-like micelles of PONB-*b*-MeO-PPV prepared by seeded growth using seed to unimer ratios of 1:50 with light on-off cycles using 5W white LED as the light source. (a) 0sec (initial seed), (b) 30 sec under light (red) and 30 min without light (empty), (c) additional 30 sec under light (red) and 30 min without light (empty), (d) additional 1 min under light (red) and 30 min without light (empty), and (e) additional 2 min under light.

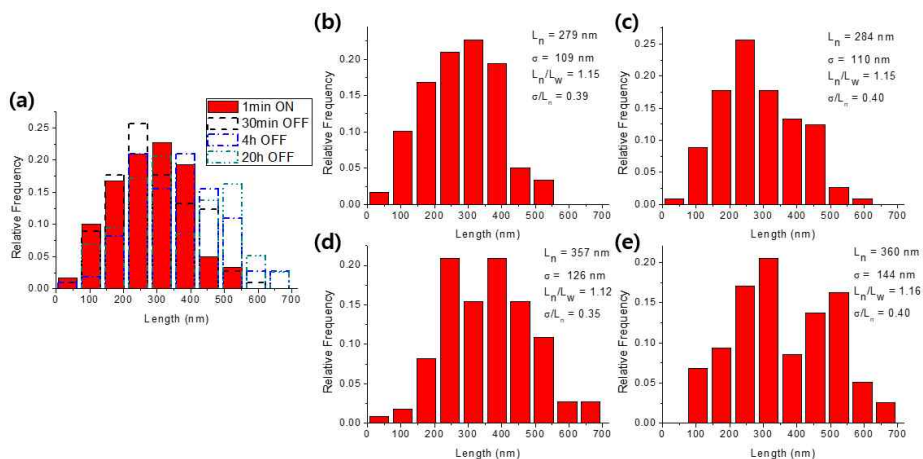


Figure S4.8. Contour length distributions of nanofibers of $\text{PONB}_{50}\text{-}b\text{-MeO-PPV}_{15}$ prepared by seeded growth with unimer-to-seed ratio of 1:50 with partial isomerization by LED irradiation for 1 min and then long-term aging at dark. (a) Overlay of all distributions, (b) photoisomerized for 1min, and aging at dark for (c) 30 min, (d) 4 h, and (e) 20 h.

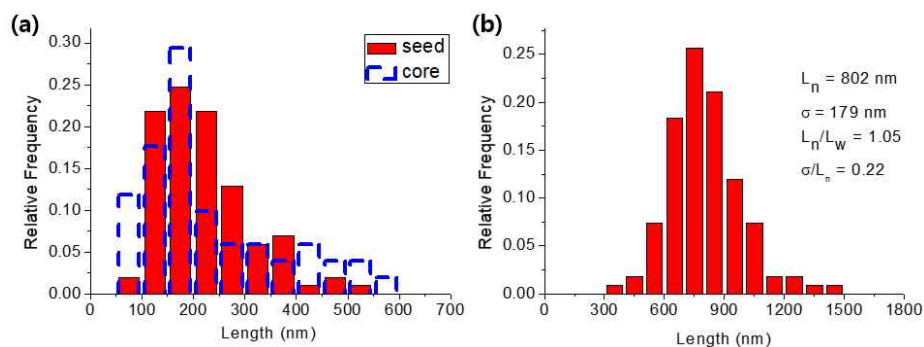


Figure S4.9. Contour length distributions of (a) seed micelles of $\text{PNB}_{20}\text{-}b\text{-MeO-PPV}_{15}$ (red) and the central block of ABA triblock comicelles (empty), and (b) ABA triblock comicelles.

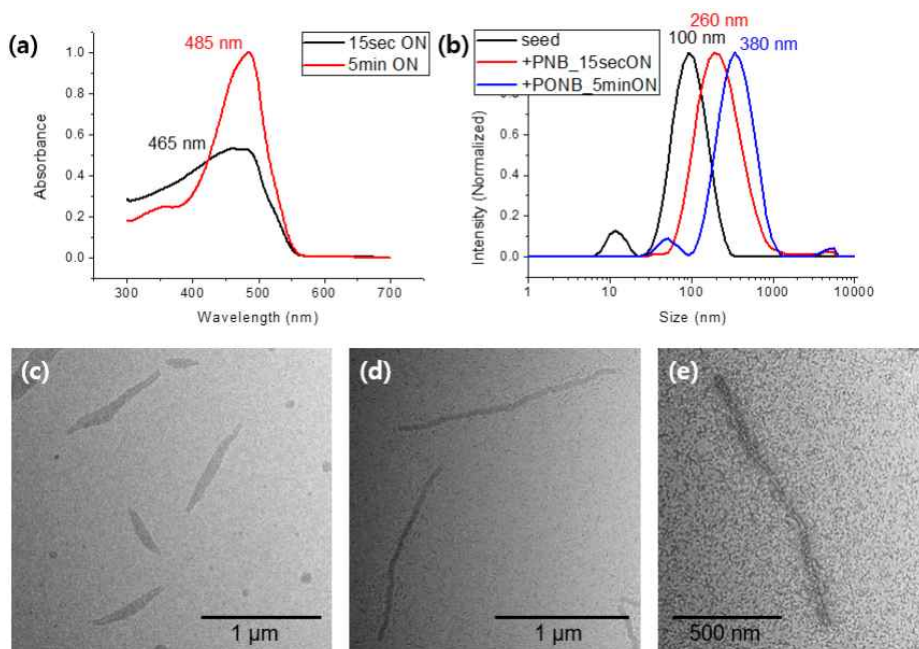


Figure S4.10. (a) UV/vis spectra and (b) DLS profiles of partially isomerized PNB₂₀-*b*-MeO-PPV₁₅ (LED irradiation for 15 sec) and fully isomerized gradient comicelles (LED irradiation for 5 min). TEM images of (c) partially isomerized PNB₂₀-*b*-MeO-PPV₁₅, (d) gradient comicelles, and (e) the comicelles after negative staining using aqueous solution of phosphotungstic acid.

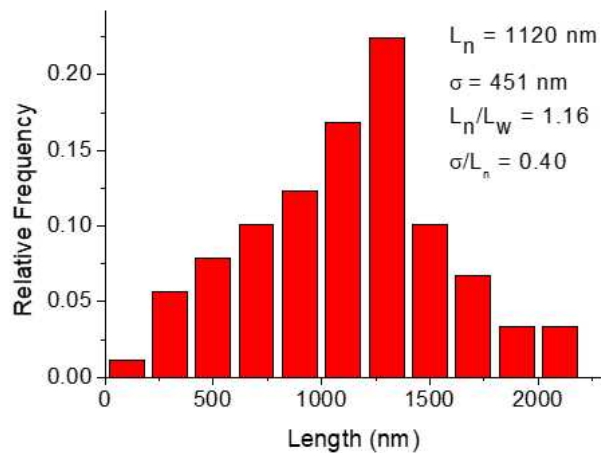


Figure S4.11. Contour length distributions of gradient comicelles.

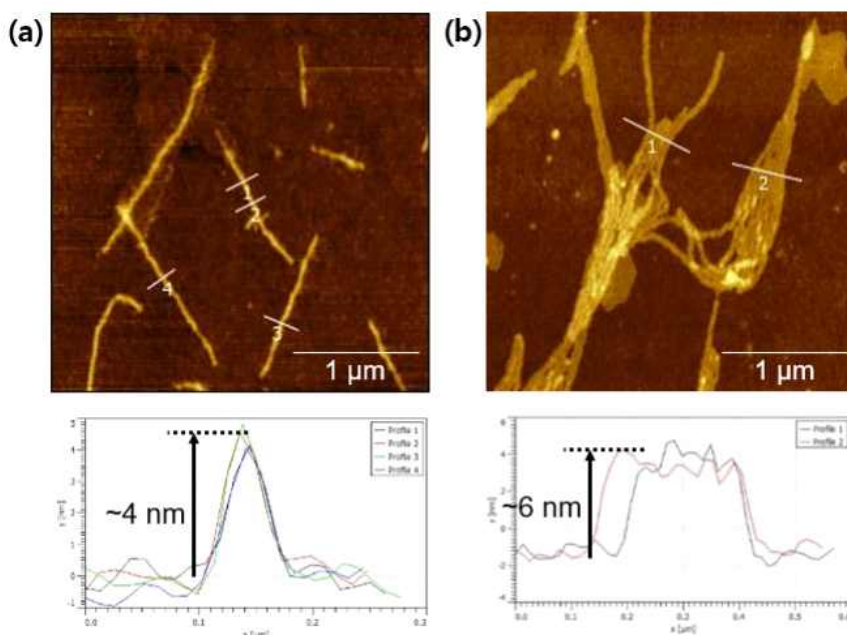


Figure S4.12. AFM images of nanofibers prepared by isomerized (a) $\text{PONB}_{50}\text{-}b\text{-MeO-PPV}_{15}$ and (b) $\text{PNB}_{20}\text{-}b\text{-MeO-PPV}_{15}$. Height profiles along the white lines of AFM images are at the bottom of each image.

4.7. References

- (1) (a) Tritschler, U.; Pearce, S.; Gwyther, J.; Whittell, G. R.; Manners, I. *Macromolecules* **2017**, *50*, 3439. (b) Wu, D.; Huang, Y.; Xu, F.; Mai, Y.; Yan, D. *J. Polym. Sci., Part A: Polym. Chem.* **2017**, *55*, 1459.
- (2) (a) Gilroy, J. B.; Gädt, T.; Whittell, G. R.; Chabanne, L.; Mitchels, J. M.; Richardson, R. M.; Winnik, M. A.; Manners, I. *Nat. Chem.* **2010**, *2*, 566. (b) Qui, H.; Hudson, Z. M.; Winnik, M. A.; Manners, I. *Science* **2015**, *347*, 1329. (c) Qui, H.; Gao, Y.; Boott, C. E.; Gould, O. E. C.; Harniman, R. L.; Miles, M. J.; Webb, S. E. D.; Winnik, M. A.; Manners, I. *Science* **2016**, *352*, 697.
- (3) Yoon, K.-Y.; Lee, I.-H.; Kim, K. O.; Jang, J.; Lee, E.; Choi, T.-L. *J. Am. Chem. Soc.* **2012**, *134*, 14291.
- (4) (a) Granier, T.; Thomas, E. L.; Gagnon, D. R.; Karasz, F. E.; Lenz, R. W. *J. Polym. Sci., Part B: Polym. Phys.* **1986**, *24*, 2793. (b) Chen, D.; Winokur, M. J.; Masse, M. A.; Karasz, F. E. *Polymer* **1992**, *33*, 3116.
- (5) Yu, C.-Y.; Turner, M. L. *Angew. Chem. Int. Ed.* **2006**, *45*, 7797.
- (6) (a) Katayama, H.; Nagao, M.; Nishimura, T.; Matsui, Y.; Umeda, K.; Akamatsu, K.; Tsuruoka, T.; Nawafune, H.; Ozawa, F. *J. Am. Chem. Soc.* **2005**, *127*, 4350. (b) Wang, F.; He, F.; Xie, Z.; Li, M.; Hanif, M.; Gu, X.; Yang, B.; Zhang, H.; Lu, P.; Ma, Y. *J. Polym. Sci., Part A: Polym. Chem.* **2008**, *46*, 5242.
- (7) Yoon, K.-Y.; Lee, I.-H.; Choi, T.-L. *RSC Adv.* **2014**, *4*, 49180.
- (8) Menk, F.; Mondeshki, M.; Dudenko, D.; Shin, S.; Schollmeyer, D.; Ceyhun, O.; Choi, T.-L.; Zentel, R. *Macromolecules* **2015**, *48*, 7435.
- (9) Menk, F.; Shin, S.; Kim, K.-O.; Scherer, M.; Gehrig, D.; Laquai, F.; Choi, T.-L.; Zentel, R. *Macromolecules* **2016**, *49*, 2085.
- (10) Chen, S. H.; Su, A. C.; Han, S. R.; Chen, S. A.; Lee, Y. Z.

Macromolecules **2004**, *37*, 181.

(11) Yin, G.; Chen, G.; Zhou, Z.; Li, Q. *RSC Adv.* **2015**, *5*, 33356.

(12) (a) Xu, J.; Jung, K.; Atme, A.; Shanmugam S.; Boyer, C. *J. Am. Chem. Soc.* **2014**, *136*, 5508. (b) Konkolewicz, D.; Schroder, K.; Buback, J.; Bernhard, S.; Matyjaszewski, K. *ACS Macro Lett.* **2012**, *1*, 1219.

(13) Kang, E.-H.; Lee, I. S.; Choi, T.-L. *J. Am. Chem. Soc.* **2011**, *133*, 11904.

Chapter 5.

Application of amplifying fluorescent polymer nanoparticles to selective detection of charge-neutral analytes

5.1. Abstract

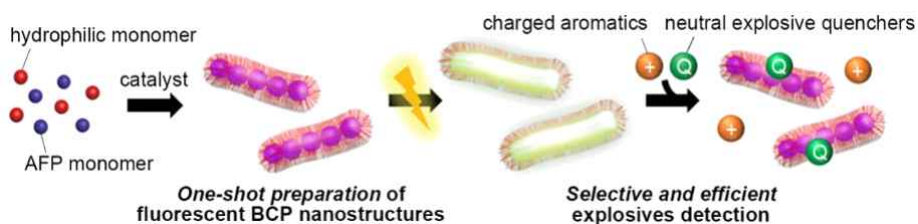
Water dispersible fluorescent nanostructures were prepared by a simple, one-shot *in situ* nanoparticlization of poly(*para*- phenylenevinylene) (PPV) block copolymers (BCPs) wherein the BCP formation and self-assembly occur simultaneously. Introduction of solubilizing block using polyethylene glycol (PEG) substituted oxanorbornene rendered the nanostructures water-dispersible, and the possibility to be utilized as a chemical sensor in aqueous solution was tested by fluorescent quenching experiments. The nanostructures exhibited morphology-dependent fluorescence quenching response in the presence of trace amounts of nitroaromatics, including 2,4,6-trinitrotoluene (TNT). The quenching response shows remarkable discrimination against paraquat, a widely used electron-acceptor and a strong quencher, in favor of neutral analytes.

5.2. Introduction

In previous chapters, we demonstrated that various nanostructures containing conjugated block copolymers (BCPs) could be prepared by simple one-shot *in situ* nanoparticlization of conjugated polymers (INCP) method, which induce spontaneous self-assembly during polymerization of block copolymers via one-shot feeding of comonomers. The development of simple preparation method for functional nanomaterials could lower the barrier to practical applications. The dimension of nanostructures prepared by INCP methods could be easily controlled by the monomer feed ratio, and they are stable under changes of environment such as pressure, temperature, and processing solvents due to strong π - π interaction of insoluble conjugated cores. We envisioned that such properties would allow us to evaluate the performance of dimensionally controlled conjugate polymer nanostructures in applications where energy transport properties play a crucial role, such as amplifying fluorescence sensing.¹

Fluorescent conjugated polymers are known for their extraordinary performances as chemical sensors, and are often called amplifying fluorescent polymers (AFPs).¹ In AFPs, the dimensionality of exciton migration plays a crucial role in their sensitivity. In the solid state, where extended intra- and interchain electronic interactions are possible, efficient three-dimensional transport of excitons leads to remarkable sensitivity towards analytes which can interact with the π -electronic structures of AFP, leading to strong fluorescence quenching in the presence of trace amounts of analytes.^{2a, b} In solution, however, the reduced sensitivity attributed to one-dimensional random walk of excitons confined to individual unimeric polymer chains lead to significant reduction in sensitivity. Therefore, strategies for using AFPs in solution-phase chemosensing have relied exclusively on enhancing the

strength of polymer-analyte binding constant by employing conjugated polyelectrolytes (CPEs) to detect oppositely charged molecules,^{2c-e} a scheme intrinsically dependent on the acidity and ionic strength of the media.^{2f} The selective detection of neutral analytes over ionic interferants in water is critical. For example, selective detection of neutral nitroaromatic analytes in water is important in sensing buried explosives and/or measuring water contamination levels.³ CPEs are quenched by neutral nitroaromatics in water,⁴ but with sensitivities three orders of magnitude lower than that of paraquat, a positively charged electron-poor quencher. Dimensionally controlled, water-dispersible nanostructures of AFPs capable of excluding charged analytes would therefore be of considerable importance.



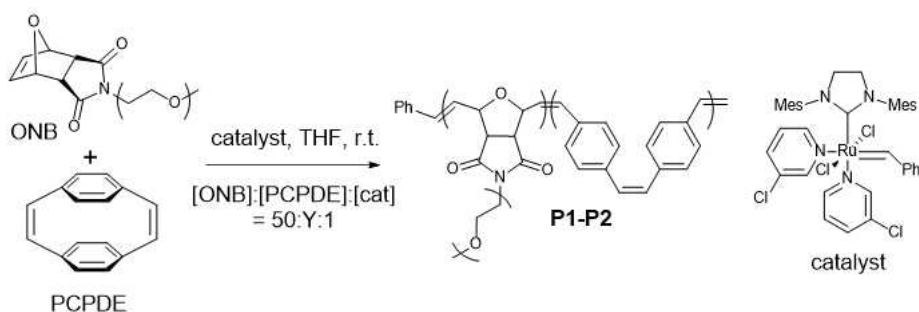
Scheme 5.1. Schematic representation of facile preparation of fluorescent BCP nanostructures by one-shot INCP method and their selective sensing ability toward neutral explosive quenchers against charged aromatic molecules.

In this chapter, we prepared water-dispersible fluorescent nanostructures composed of BCPs containing AFPs, poly(*para*-phenylenevinylene) (PPV), by one-shot INCP method. By varying the monomer feed ratio, control over the morphology of the resulting nanostructures was possible both in organic and aqueous solution. Notably, the resulting water-dispersible fluorescent polymer nanostructures exhibited dimensionality-dependent, discriminative

amplifying fluorescence sensing behavior toward trace amounts of explosive nitroaromatics, such as 2,4,6-trinitrotoluene (TNT), over ionic interferants, paraquat dichloride (PQ), with the Stern-Volmer quenching constants (K_{SV}) over 10^5 M^{-1} .

5.3. Results and discussion

Table 5.1. Synthesis of PONB-*b*-PPV by one-shot ROMP using ONB and PCPDE.



Polymer	[ONB]:[PCPDE]:[cat]	Reaction time (h)	PCPDE conv. (%) ^a	Yield (%)	D_h (nm) ^b
P1	50:5:1	4	>99	70	70
P2	50:15:1	12	>99	86	135

^aMeasured by ^1H NMR. ^bMeasured by DLS.

The strategy of one-shot synthesis of PPV BCPs could be expanded to prepare water-dispersible polymer nanostructures using oxanorbornene (ONB) monomer containing a poly(ethylene glycol) (PEG) side chain as the solubilizing block. Well-defined BCPs with monomer feed ratios, fast reacting ONB⁵ versus slow reacting [2.2]paracyclophane-1,9-diene (PCPDE),⁶ of 50:5 and 50:15 were synthesized in a one-shot manner using the highly active and fast initiating third-generation Grubbs

catalyst in tetrahydrofuran (THF) (Table 5.1). The DLS, AFM, and TEM analyses on the resulting **P1-P2** in aqueous solution showed the structural evolution from spheres (**P1**, hydrodynamic diameter (D_h) = 70 nm) to nanocaterpillars (**P2**, D_h = 135 nm) by 1D growth (Figure 5.1, b-e). Additionally, the same nanocaterpillar morphology was observed for **P2** in both chloroform and aqueous solutions by cryo-TEM (Figure 5.2, higher electron density of a chloroform solvent caused brighter shell part in the solution, different with the image of aqueous solution), indicating stable nanostructure formation that was unaffected by solvent change due to their strong π - π interactions.⁵ Notably, this is the first example of a water-dispersible conjugated BCP nanostructure prepared by one-shot polymerization, representing a promising strategy for a large-scale preparation of well-defined light-emitting polymer nanostructures.

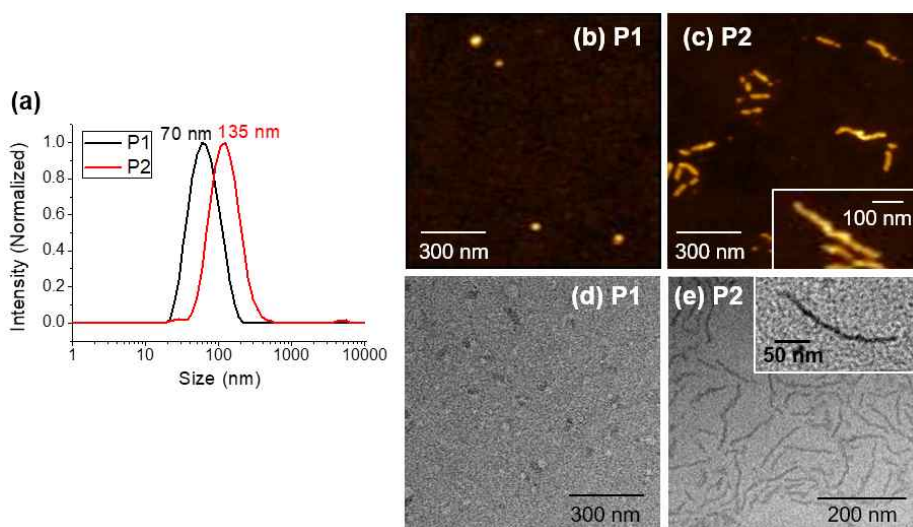


Figure 5.1. (a) DLS profiles of **P1** and **P2** in water at 0.1 mg/mL. (b and c) AFM images and (d and e) TEM images of nanostructures of BCPs prepared from aqueous solutions of **P1** and **P2**, respectively.

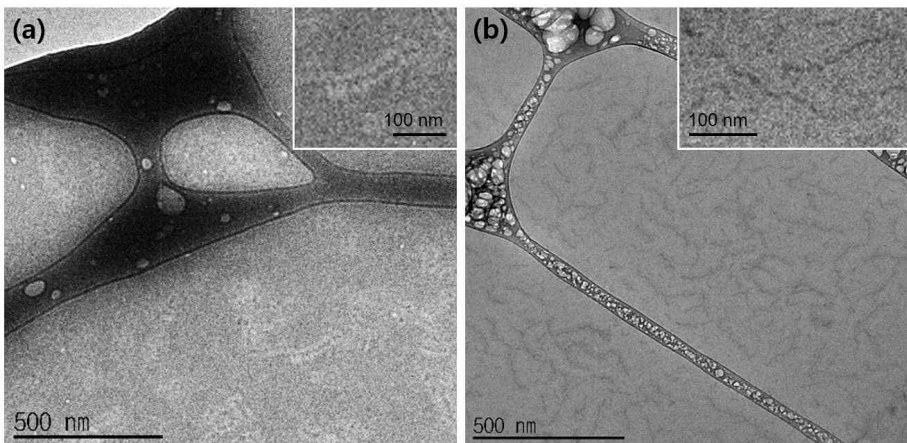


Figure 5.2. Cryo TEM images of **P2** in chloroform (a) and water (b). Inset images for higher magnification.

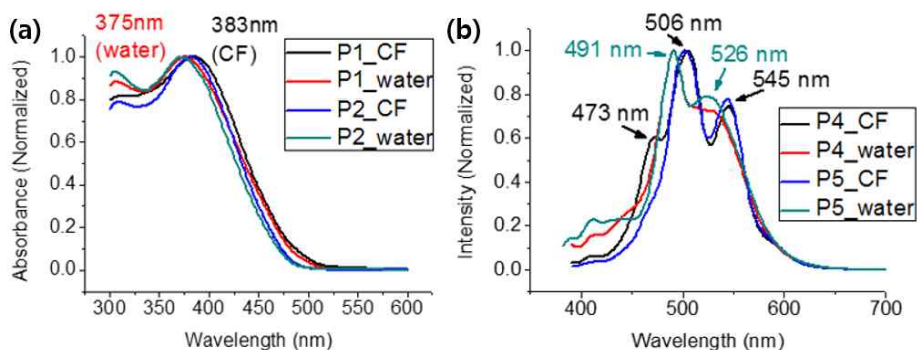


Figure 5.3. (a) The absorbance spectrum and (b) the emission spectrum of **P1-P2** in chloroform and water (Concentration of all polymer solution = 0.05 mg/ml). The additional peak at 473 nm of **P1** in chloroform stands for single-chromophore emission.

For application to AFP sensor materials, optical properties of BCPs were analyzed (Figure 5.3). The UV/Vis spectra of the PPV BCPs showed an absorption maximum at 383 nm in chloroform and

375 nm in water. The photoluminescence spectrum showed emission peaks at 506 and 545 nm in chloroform and 491 and 526 nm in water. The internal quantum yields of the nanoparticles were 17.8% and 2.4% (**P4**), and 17.5% and 3.3% (**P5**) in chloroform and aqueous solution, respectively.

To test the potential of using PPV BCP nanostructures as chemosensors, fluorescence titration studies of **P1** and **P2** were carried out using 2,4-dinitrotoluene (DNT) and TNT as analytes in water (Figure 5.4 and S5.1). The results showed a strong dependence of the sensory response on the nanoscale morphology of PPV BCPs. Approximately 30 μ M TNT was required to quench 40% of the fluorescence of spherical nanostructures of **P1**, whereas a similar degree of quenching was obtained even with only 1 μ M TNT using linear **P2** (Figure 5.4, a). The corresponding Stern-Volmer plot showed a linear relationship (Figure 5.4, b), and the K_{SV} of **P2** was $3.9 \times 10^5 \text{ M}^{-1}$, which is 26-fold higher than that of **P1** ($1.5 \times 10^4 \text{ M}^{-1}$). The K_{SV} value for **P2** is higher than previously-reported aggregated AFP-based systems, such as light-emitting oligosilole nanoparticles ($K_{SV} = 5.0 \times 10^3 \text{ M}^{-1}$), and pyrene-containing conjugated fluorescent polymer thin films ($K_{SV} = 3.26 \times 10^4 \text{ M}^{-1}$).⁷ Furthermore, the sensitivity of **P2** is significantly greater than other known classes of fluorescence-based aqueous-phase sensors for TNT, including a pentacene-based small molecule, pyrene nanocomposites, and metal-organic frameworks (Table S5.1).⁸ The fluorescence quenching was visually detectable, even at very low TNT concentrations (0.5 ppm, Figure 5.4, c). In both **P1** and **P2**, the K_{SV} values for DNT were lower than those for TNT by a factor of approximately 5, but **P2** still showed a 22-fold higher sensory performance than **P1** ($3.3 \times 10^3 \text{ M}^{-1}$ for **P1** and $7.2 \times 10^4 \text{ M}^{-1}$ for **P2**, Figure 5.4, b). Time-resolved photoluminescence measurements using the

aqueous solutions of **P1** showed decay profiles that were unaltered in the presence of DNT (Figure 5.4, d), suggesting that static quenching is the predominant quenching mechanism.

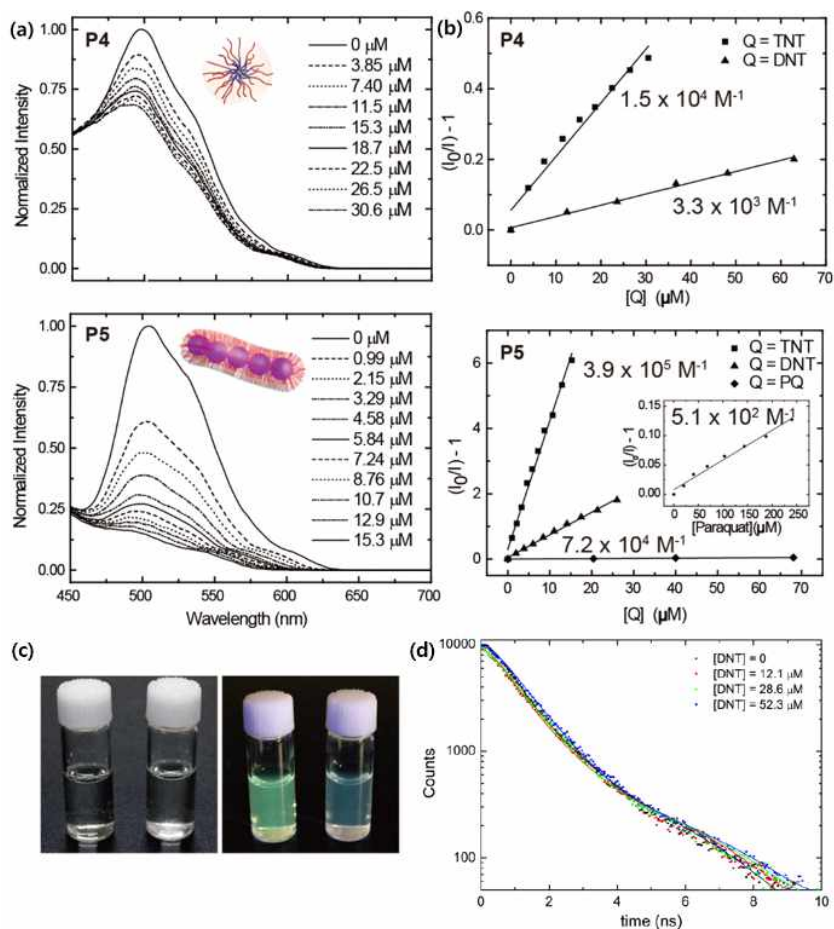


Figure 5.4. Fluorescence titration studies of for **P1** and **P2** using DNT, TNT, and paraquat dichloride (PQ) as analytes. (a) Evolution of photoluminescence spectra of aqueous solutions of spherical **P1** nanoparticles (top) and linear **P2** nanostructures (bottom) upon treatment with TNT. (b) Stern-Volmer plots for the aqueous-phase fluorescence quenching of **P1** (top) using DNT and TNT, and **P2** (bottom) using

DNT, TNT, and PQ (the inset shows the Stern-Volmer plot for PQ over a wider concentration range). K_{SV} values are shown below the corresponding linear fit. (c) Photographs of aqueous solutions of **P2** under room light (left) and under irradiation with a hand-held UV lamp (right) containing no quencher (left vial) and 0.5 ppm TNT (right vial). (d) Time-resolved photoluminescence decay profiles of **P1** in water in the presence of various amounts of DNT.

The increase in the degree of polymerization (from 5 to 15) of the PPV domain alone does not account for this more than 20-fold increase in the quenching efficiency between **P1** and **P2**. Previous studies on dilute solutions of soluble poly(p-phenyleneethynylene) (PPE) showed that the increase in molecular weight enhances K_{SV} (in the molecular weight ranges below the exciton migration length), but with a proportionality of less than 1 (i.e. the degree of K_{SV} enhancement is smaller than that of the molecular weight increase).⁹ Moreover, adding a small amount of a poor solvent into the PPE solutions to induce aggregation led to a much greater increase in K_{SV} .^{2b} Our one-shot INCP strategy makes it possible to tune the sensory performance of AFPs by controlling the dimensionality of BCP nanostructures without altering the solvent environment. This aspect is crucial for consistent solution-phase sensing applications.

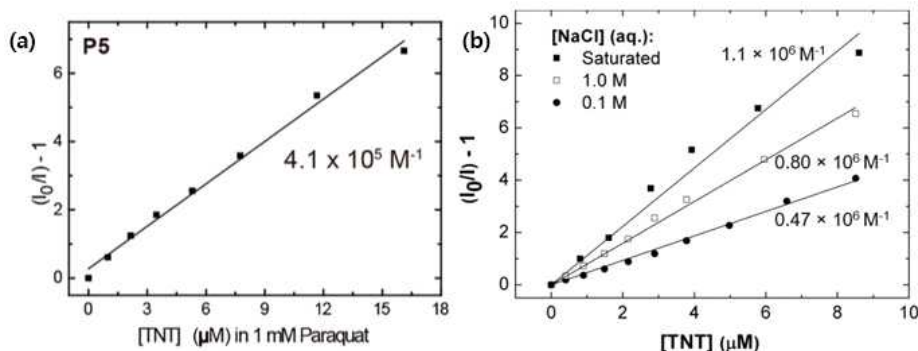


Figure 5.5. The Stern-Volmer plot of the fluorescence quenching of **P2** with (a) TNT in 1 mM aqueous PQ, and (b) under various concentrations of sodium chloride. The numbers next to the linear fits indicate the corresponding K_{SV} values.

To test the ability of the PPV BCP nanostructures to serve as discriminative sensors for neutrally charged analytes, quenching studies were performed using paraquat dichloride (PQ), a strong electron acceptor and a widely used as quenching agent. When a solution of the linear **P2** was treated with PQ, only a weak quenching response, with a K_{SV} of $5.1 \times 10^2 \text{ M}^{-1}$, was obtained (Figure 5.4, b and Figure S5.2). This small quenching efficiency of the PPV BCP toward PQ, despite the high efficiency of the photoinduced charge-transfer reported between unsubstituted PPV and ethyl viologen,¹⁰ could be ascribed to the suppressed penetration of the highly charged PQ across the PEG corona layer, preventing quenching interactions with the PPV core. Furthermore, the presence of PQ did not affect the quenching response of **P2** towards TNT. Fluorescence titration measurement of **P2** in 1 mM aqueous PQ with TNT showed nearly identical quenching efficiency ($K_{SV} = 4.1 \times 10^5 \text{ M}^{-1}$, Figure 5.5, a and S5.2) as that obtained from deionized water. To the best of our knowledge, these results constitute

the first example of highly discriminative sensing of neutral nitroaromatics over PQ in water using AFPs.

The sensor performance of **P2** in the presence of sodium chloride exhibited enhancement with increasing salt concentration (Figure 5.5, b). In saturated sodium chloride solution, a K_{SV} value of greater than 10^6 M^{-1} was obtained. The enhancement of the quenching constant in the presence of dissolved sodium chloride is attributed to the salting-out effect. The ability of **P2** to act as a highly sensitive fluorescence sensor in high ionic-strength solutions render the system promising for field applications.

5.4. Conclusion

In summary, we demonstrated a simple and efficient one-shot preparation of water-dispersible nanoparticles from amphiphilic fluorescent conjugated BCPs. Using comonomers having large rate difference, ONB derivatives and PCPDE, one-shot block copolymerization was possible and spontaneous *in situ* nanoparticlization to micelles and nanocaterpillars was induced by the strong π - π interactions among the second PPV block. The water-dispersible PPV BCP nanostructures showed a powerful quenching response towards trace amounts of explosive nitroaromatics in water (K_{SV} up to $4 \times 10^5 \text{ M}^{-1}$). Notably, the discriminative detection of TNT over PQ was achieved by effective shielding against charged interferants in water. This high-performance sensor application is the first application of INCP-prepared nanoparticles to useful optoelectronics and attests to the power of the one-shot INCP as a new synthetic platform for a rapid, scalable preparation of semiconducting polymer nanostructures with tailor-made nanoscale morphologies.

5.5. Experimental section

Characterization

NMR spectra were recorded by Varian/Oxford As-500 (500 MHz for ^1H /125 MHz for ^{13}C) spectrometer. UV/vis spectra were obtained by a Jasco Inc. UV/vis spectrometer V-630, and fluorescence spectra were obtained by FP-8300 (Jasco Inc.). Quantum efficiency was measured by QE-1200 (Otsuka Electronics). Dynamic light scattering (DLS) data were obtained by a Malvern Zetasizer Nano ZS. Multimode 8 and Nanoscope V controller (Veeco Instrument) were used for AFM imaging. All images were obtained on tapping mode using noncontact mode tip from Nanoworld (Pointprobe tip, NCHR type) with spring constant of 42 N m⁻¹ and tip radius of ≤ 8 nm. Quenching studies were conducted using PerkinElmer LS55 spectrometer. Time-resolved photoluminescence measurements were conducted using Horiba Fluorolog-3 fitted with FL3-TCSPC. Pulsed LED (334 nm) was used as the light source and the intensity was measured at 505 nm, with a 450 nm cut-off filter being used.

Materials

All reagents were commercially available from Acros, Alfa, Sigma Aldrich and TCI and used without further purification unless specified otherwise. All polymerizations were carried out under dry argon atmospheres using standard Schlenk techniques. THF was distilled over sodium and benzophenone and anhydrous deuterium THF solvent (≥ 99.95 %) were purchased from Euriso-Top[®]. THF solvents were degassed by argon bubbling for 10 minutes before using on polymerization. The third generation Grubbs catalyst was prepared by the reported method.¹¹

Synthesis

ONB was prepared through previously reported procedures.¹² PCPDE was prepared using same method in Chapter 3.

General procedure for the one-shot INCP of PONB-*b*-PPV

Both comonomers (62.8 μ mol for ONB and 6.28-18.8 μ mol for PCPDE) were weighed into a 2 mL sized screw-cap vial with a septum and purged with argon. Anhydrous and degassed THF was added (43-150 μ L) to the vial. THF solution of the third-generation Grubbs catalyst (1.26 μ mol) was added (20 μ L) to the monomer solution at once under vigorous stirring. The mixture was stirred for 4-12 h at the room temperature. The reaction was quenched by excess ethyl vinyl ether. The crude mixture was precipitated into cold ether at -78 °C, and the obtained sticky gel was dried *in vacuo*.

Poly(ONBmPEG)-*b*-poly(PCPDE) one-shot copolymers (P1-P2)

Yield: 70-86% (see Table 5.1). ¹H NMR (500 MHz, CD₂Cl₂): δ 7.28-7.37 (m), 7.06-7.13 (m), 6.71-6.77 (m), 6.53-6.59 (m), 6.36 (m), 6.08s (s, 1H), 5.77-5.80 (m, 1H), 4.92-5.01 (m, 1H), 4.45 (s, 1H), 3.33-3.67 (m, 41H). ¹³C NMR (125 MHz, CDCl₃): δ 175.6, 131.9, 131.0, 81.0, 72.0, 70.7, 70.0, 66.9, 59.1, 53.6, 53.4, 52.5, 38.1 (all the PONBmPEG-*b*-P(PCPDE) one-shot copolymers have identical ¹H NMR and ¹³C NMR spectra).

Atomic force microscopy (AFM)

The atomic force microscopy experiments were performed with a thin film prepared by spin-coating one drop of the polymer solution (~0.02mg polymer/mL, CHCl₃: spinning rate = 3000 rpm for 30 sec). The solvent was filtered by 0.2- μ m PTFE filter before making the

solution. The thin films were prepared on glass substrates. All images were obtained on tapping mode using non-contact mode tips from Nanoworld (Pointprobe tip, NCHR type) with spring constant of 42 N m⁻¹ and tip radius of ≤ 8 nm.

Transmission electron microscopy (TEM)

Dry-TEM and cryo-TEM imaging were performed by JEM-2100 operated at 120 kV and SC 1000 CCD camera (Gatan Inc.). The samples for dry-TEM imaging were prepared by drop casting one drop ($\sim 10 \mu\text{L}$) of sample solution (0.1 mg/mL) on the carbon-coated copper grid. The cryo-TEM experiments were performed with a thin film of solution (5 μL , 0.1 mg/mL) transferred to a lacey supported grid. The thin solution films were prepared under solvent vapor saturated condition (chloroform) within a custom-built environmental chamber in order to prevent evaporation of solvent from sample solution. The excess liquid was blotted with filter paper for 2-4 seconds, and the thin solution films were rapidly vitrified by plunging them into liquid ethane (-170 °C) using Gatan CryoplungeTM3 system. The grid was transferred on a Gatan 626 cryoholder, using a cryo-transfer device. After that they were transferred to a JEM-2100. Direct imaging was carried out at a temperature of approximately -175 °C and with a 120 kV accelerating voltage.

Fluorescence Quenching Studies.

20 mM solutions of DNT and TNT were prepared by dissolving appropriate amounts of each quencher in ethanol. Quencher stock solutions for fluorescence titration were prepared by diluting the 20 mM stock solutions by a factor of 200 with aqueous PPV BCP stock solution (2×10^{-6} M based on PPV repeating unit), so as to give the

final quencher concentration of 0.1 mM and to make dilution effects negligible. Excitation wavelength used was 371 nm. For each quenching study, initial fluorescence emission intensity was measured, followed by the addition of aliquots of the quencher stock solution. Fluorescence intensity was measured 20 minutes after each addition to allow sufficient time for equilibration. Measurements were performed in triplicate with R-squared values of >0.98 for each set of conditions.

5.6 Supporting information

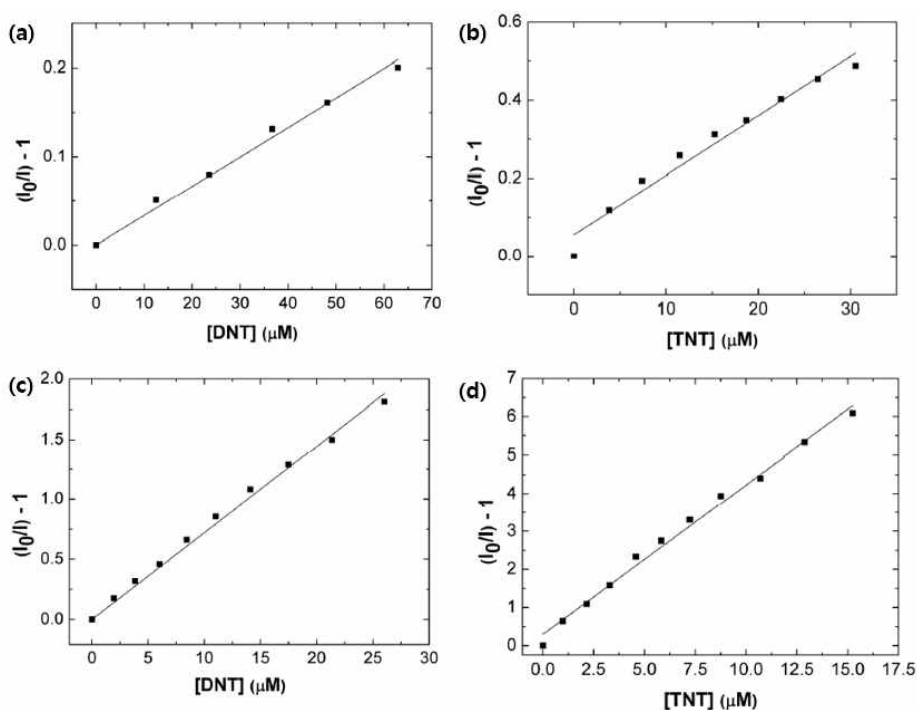
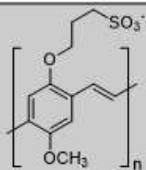
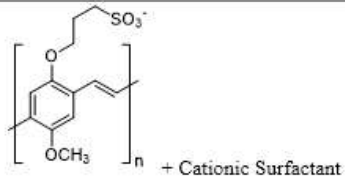
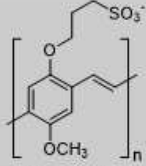
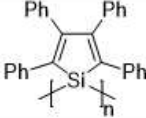
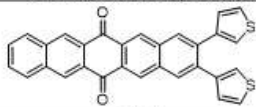
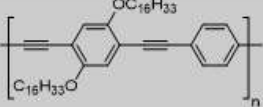
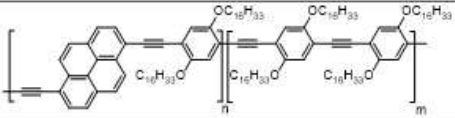


Figure S5.1. Stern-Volmer plot for the fluorescence titration of **P1** with (a) DNT ($K_{SV} = 3.3 \times 10^3 \text{ M}^{-1}$) and (b) TNT ($K_{SV} = 1.5 \times 10^4 \text{ M}^{-1}$). Stern-Volmer plot for the fluorescence titration of **P2** with (c) DNT ($K_{SV} = 7.2 \times 10^4 \text{ M}^{-1}$) and (d) TNT ($K_{SV} = 3.9 \times 10^5 \text{ M}^{-1}$).

Table S5.1. Stern-Volmer quenching constants of various fluorescent probes, representative of their own material class, toward TNT and paraquat in water.²

Probe	Structure/Notes	Analyte	Quenching Constant (K_{SV}, M^{-1})
PPV		TNT	1.02×10^4
PPV		TNT	9.13×10^4
PPV		Paraquat	1.7×10^7
Oligosilole Nanoparticle		TNT	4,500
Metal-Organic Framework	$Zr_6O_4(OH)_4(TCPP)_3$ (TCPP = tetrakis(4-carboxyphenyl)porphyrin)	TNT	3.5×10^4
Pentacenequinone Derivative Nanoaggregates		TNT	4,300
PPE Thin Film		TNT	7,750
Pyrene-Containing PPE Thin Film		TNT	3.65×10^4
Pyrene-Polyethersulfone Composite Nanofiber	N/A	TNT	1.80×10^5

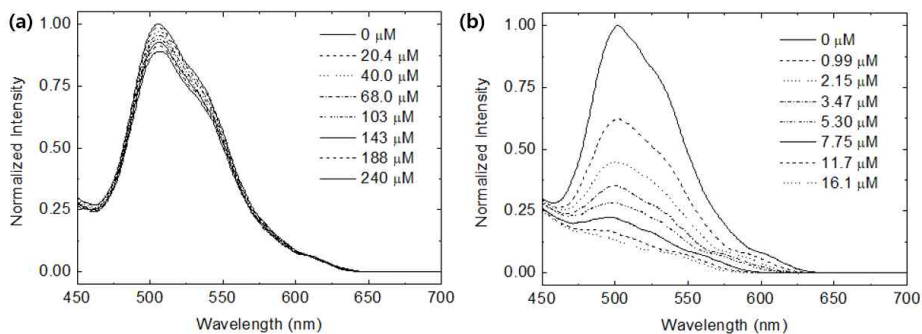


Figure S5.2. Photoluminescence spectra of (a) aqueous **P2** in presence of various amounts of paraquat dichloride and (b) of **P2** in 1 mM aqueous paraquat upon treatment with increasing amounts of TNT.

5.7. References

[†]Portions of this chapter have been previously reported, see: Shin, S.; Lim, J.; Gu, M.-L.; Yu, C.-Y.; Hong, M.; Char, K.; Choi, T.-L. *Polym. Chem.* **2017**, *8*, 7507.

(1) Thomas, S. W.; Joly, G. D.; Swager, T. M. *Chem. Rev.* **2007**, *107*, 1339.

(2) (a) Rose, A.; Lugmair, C. G.; Swager, T. M. *J. Am. Chem. Soc.* **2001**, *123*, 11298.

42. (b) Zahn, S.; Swager, T. M. *Angew. Chem. Int. Ed.* **2002**, *41*, 4225. (c) Chen, L.; McBranch, D. W.; Wang, H. L.; Helgeson, R.; Wudl F.; Whitten, D. G. *Proc. Natl. Acad. Sci. U. S. A.* **1999**, *96*, 12287. (d) Tan, C.; Atas, E.; Müller, J. G.; Pinto, M. R.; Kleiman, V. D.; Schanze, K. S.; *J. Am. Chem. Soc.* **2004**, *126*, 13685.

(e) Tan, C.; M. Pinto R.; Schanze, K. S. *Chem. Commun.* **2002**, 446.

(f) Fan, Q.-L.; Zhou, Y.; Lu, X.-M.; Hou, X.-Y.; Huang, W. *Macromolecules* **2005**, *38*, 2927.

(3) Toal, S. J.; Trogler, W. C. *J. Mater. Chem.* **2006**, *16*, 2871.

(4) Chen, L.; McBranch, D.; Wang, R.; Whitten, D. *Chem. Phys. Lett.*

2000, 330, 27.

(5) Yoon, K.-Y.; Lee, I.-H.; Kim, K. O.; Jang, J.; Lee, E.; Choi, T.-L. *J. Am. Chem. Soc.* **2012**, 134, 14291.

(6) Miao, Y.-J.; Bazan, G. C. *Macromolecules* **1994**, 27, 1063.

(7) (a) Toal, S. J.; Magde, D.; Trogler, W. C. *Chem. Commun.* **2005**, 5465. (b) He, G.; Yan, N.; Yang, J.; Wang, H.; Ding, L.; Yin, S.; Fang, Y. *Macromolecules* **2011**, 44, 4759.

(8) (a) Bhalla, V.; Gupta, A.; Kumar, M. *Org. Lett.* **2012**, 14, 3112. (b) Sun, X. C.; Liu, Y. X.; Shaw, G.; Carrier, A.; Dey, S.; Zhao, J.; Lei, Y. *Acs. Appl. Mater. Inter.* **2015**, 7, 13189. (c) Yang, J.; Wang, Z.; Hu, K. L.; Li, Y. S.; Feng, J. F.; Shi, J. L.; Gu, J. L.; *Acs. Appl. Mater. Inter.* **2015**, 7, 11956.

(9) Zhou, Q.; Swager, T. M. *J. Am. Chem. Soc.* **1995**, 117, 12593.

(10) Lee, J. I.; Lee, H. Y.; Shim, H. K.; Eom, H. S.; Jeoung, S. C.; Kim, D. *Mol. Cryst. Liq. Cryst. Sci. Technol., Sect. A Mol. Cryst. Liq. Cryst.* **1998**, 316, 257.

(11) Kang, E.-H.; Lee, I. S.; Choi, T.-L. *J. Am. Chem. Soc.* **2011**, 133, 11904.

(12) Menk, F.; Shin, S.; Kim, K.-O.; Scherer, M.; Gehrig, D.; Laquai, F.; Choi, T.-L.; Zentel, R. *Macromolecules* **2016**, 49, 2085.

Appendix.

Supramolecular Switching between Flat Sheets and Helical Tubules Triggered by Coordination Interaction

Abstract

Here we report the spontaneous formation of switchable sheets in aqueous solution, which is based on bent-shaped aromatic amphiphiles containing *m*-pyridine units at the terminals and a hydrophilic dendron at the apex. The aromatic segments self-assemble into flat sheets consisting of a zigzag conformation through π - π stacking interactions. Notably, the sheets reversibly transform into helical tubules at higher concentration and into discrete dimeric macrocycles at a lower concentration in response to Ag(I) ions through reversible coordination interactions between the pyridine units of the aromatic segments and the Ag(I) ions. While maintaining the coordination bonding interactions, the helical tubules reversibly transform into the dimeric macrocycles in response to the variation in concentration.

Introduction

The spontaneous assembly of small molecular modules by the orchestrated interplay of various non-covalent interactions is a challenging research topic in the field of supramolecular chemistry.¹ The reversibility of such noncovalent interactions opens up interesting applications to direct the systems toward the formation of dynamic architectures with responsive functions.² Rigid-rod amphiphiles consisting of hydrophobic aromatic and hydrophilic coil segments have been proven to be promising scaffolds for switchable superstructures in response to external forces.^{2b,3} For example, dumbbell-shaped aromatic rods grafted to hydrophilic oligoether dendrons aggregate to form porous capsules with gated lateral pores in response to changing temperature.⁴ Lateral attachment of dendritic segments into an aromatic rod leads the molecules to self-assemble into foldable sheets that spontaneously roll up into scrolled tubules.⁵ We recently reported that synthetic tubules can be constructed by self-assembly of bent-shaped aromatic building blocks containing an oligoether dendron at the apex.⁶ The bent-shaped rigid segments with an internal angle of 120° fit together easily to form non-covalent hexameric macrocycles that have flexible diameters because of the sliding motions between the molecules, creating dynamic tubules.⁷ Increasing the strength of the aromatic interactions of the rigid building blocks causes non-covalent macrocycles based on a cisoid stacking pattern to transform into two-dimensional (2D) layers based on a fully overlapped zigzag packing arrangement.⁸

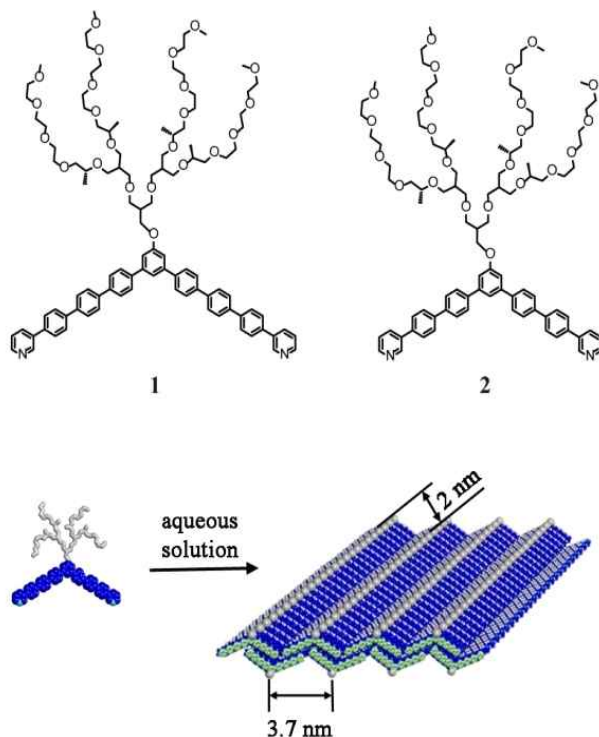


Figure 1. Molecular structures of bent-shaped amphiphiles **1** and **2** and schematic representation of the formation of responsive 2D sheets with a fully overlapped zigzag conformation of the bent-shaped aromatic segments in aqueous solution.

We envisioned that the introduction of meta-linked pyridine units at both ends of the bent-shaped aromatic segment might form stimuli-responsive 2D structures, since pyridine units are well-known to interact specifically with Ag(I) ions through reversible coordination bonds.⁹ This recognition event would cause reversible rearrangement of the fully overlapped zigzag packing arrangement of the bent-shaped rigid segments to maximize the coordination interactions between pyridine donors and Ag(I) ions at the expense of π - π stacking

interactions between aromatic rod segments.¹⁰ Consequently, this metal-directed rearrangement of the aromatic segments would endow the 2D structures with dynamic responsive functions. With this direction of research in mind, we synthesized self-assembling molecules **1** and **2** consisting of a long bent-shaped aromatic segment containing *m*-pyridine units at both ends and a hydrophilic oligoether dendron with an *S* configuration grafted at the apex. Here we report their spontaneous self-assembly to form responsive 2D sheets in aqueous solution (Figure 1). Notably, these 2D sheets reversibly transform into hollow tubules with helical cavities through a cyclic conformation of the aromatic segments in response to Ag(I) ions (see Figure 5).

Results and discussion

The aromatic amphiphiles were synthesized starting with Suzuki coupling of a 2,6-dibromophenol derivative with trimethylsilyl (TMS)-protected phenylboronic acid. The resulting compound was subjected to an etherification reaction with an oligoether dendritic chain. The transformation of the TMS groups to iodo groups was achieved by iodination with ICl. Suzuki couplings of the diiodo compound with TMS-substituted biphenylboronic acid and TMS-substituted phenylboronic acid were used to prepare the precursors of **1** and **2**, respectively. The final compounds were successfully synthesized by Suzuki coupling with 3-pyridylboronic acid. The resulting molecules were characterized by ^1H and ^{13}C NMR spectroscopies and MALDI-TOF mass spectroscopy and shown to be in full agreement with the structures presented.

Molecule **1** self-assembles into flat sheets in dilute aqueous solutions. Cryogenic transmission electron microscopy (cryo-TEM) showed sheet-like objects with curved edges against the vitrified solution background (Figure 2a), indicative of the formation of flexible sheets in bulk solution. To obtain more information on these sheets, we additionally performed TEM experiments with samples cast onto a TEM grid and negatively stained with uranyl acetate. The image shows planar sheets with regular stripes having a periodicity of 2 nm against a dark background (Figure 2b inset). This result suggests that the aromatic segments with a zigzag conformation are oriented parallel to the sheet plane, similar to the organization in the layered structures of bent-shaped molecules.⁸ The interapex distance of 3.7 nm within the zigzag conformation, as obtained from molecular modeling, indicates that the adjacent aromatic segments are slipped relative to each other with an angle of 57.4° to release the steric hindrance between the

bulky dendritic chains (Figure 1).

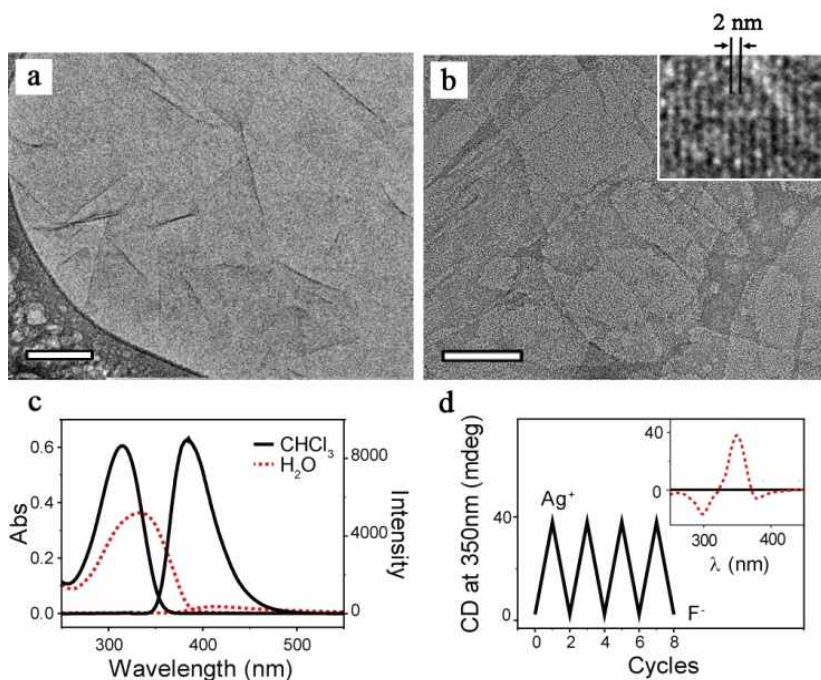


Figure 2. (a) Cryo-TEM image and (b) negative-stain TEM image of **1** obtained from a 0.03 wt % aqueous solution (scale bars = 100 nm). The inset is a magnified image of (b). (c) Absorption and emission spectra of **1** (0.03 wt %) in CHCl_3 solution (solid black lines) and aqueous solution (dotted red lines); $\lambda_{\text{ex}} = 315$ and 333 nm, respectively. (d) Reversible CD signal changes at $\lambda_{\text{max}} = 350$ nm for an aqueous solution of **1** (0.03 wt %) upon cycles of complexation and subsequent decomplexation. The inset shows CD spectra of an aqueous solution of **1** (0.03 wt %) without Ag(I) ions (solid black line) and with Ag(I) ions (dotted red line).

Optical spectroscopy investigation of **1** displayed that the absorption maximum in aqueous solution is red-shifted and the fluorescence intensity significantly quenched with respect to those

observed in chloroform solutions, indicative of the formation of aqueous aggregates through π - π interactions of the aromatic segments (Figure 2c).^{3a,11} When molecule **1** in aqueous solution was subjected to circular dichroism (CD) measurements, no CD signals could be detected, as would be expected for symmetric 2D objects, even though **1** contains chiral side groups (Figure 2d). To investigate the effect of the length of the aromatic segments for the 2D sheets, we also investigated **2**, an analogue of **1** with shorter aromatic segments. In great contrast to **1**, **2** did not show any aggregation behavior in aqueous solution even at high concentrations.

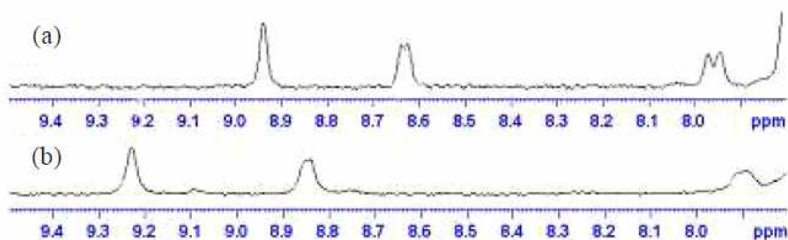


Figure 3. Comparison of ^1H -NMR spectra (300MHz, CDCl_3) of (a) **1** and (b) **1** after addition of silver salt.

The formation of flat sheets with a pyridine interior suggested that **1** in aqueous solution would exhibit Ag(I) ion-responsive behavior because the pyridine units would interact with Ag(I) ions through coordination bonds.⁹ This interaction was confirmed by ^1H NMR measurements for **1** upon the addition of 1 molar equivalent of silver triflate (Figure 3). The proton resonances associated with the pyridine units were considerably shifted downfield, demonstrating that the Ag(I) ions were coordinated to the pyridine units of the aromatic segments.¹² Remarkably, addition of the silver salt to the solution of **1** at a

concentration of 0.03 wt % induced significant CD signals (Figure 2d), suggesting that the 2D structures transformed into chiral superstructures. The CD signals immediately disappeared upon decomplexation by the addition of tetra-*n*-butylammonium fluoride (Bu_4NF),¹³ indicating that this transformation is reversible over many cycles (Figure 2d).

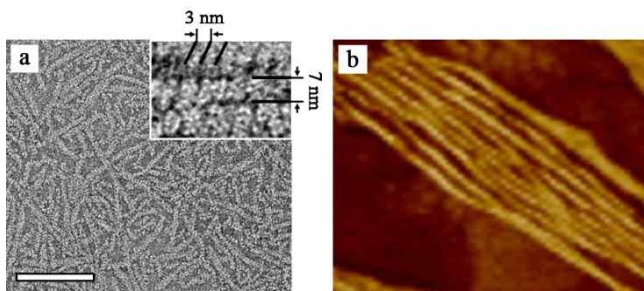


Figure 4. (a) TEM image (scale bar = 200 nm; the inset is a magnified image) and (b) AFM image (450 nm \times 350 nm) of an aqueous solution of **1** with Ag(I) ions (0.03 wt %).

The structural transformation of the 2D structure upon the addition of Ag(I) ions was visualized by TEM (Figure 4a). When the sample was cast from the solution and then negatively stained with uranyl acetate, the image showed undulated helical objects with a uniform diameter of 7 nm and a left-handed helical sense with a pitch of 3 nm. To corroborate further the handedness of the helical objects, we performed atomic force microscopy (AFM) experiments on a SiO_2/Si wafer in a completely dried state. The images revealed bundles of rodlike aggregates with a diameter of ~ 10 nm, which is larger than the value determined from TEM (Figure 4b). This difference could in part arise from deformation of the rodlike objects on the wafer surface. Closer examination of the image (Figure 4b) revealed a left-handed helical structure with a regular pitch along the rod axis, which is consistent with the result obtained from TEM.

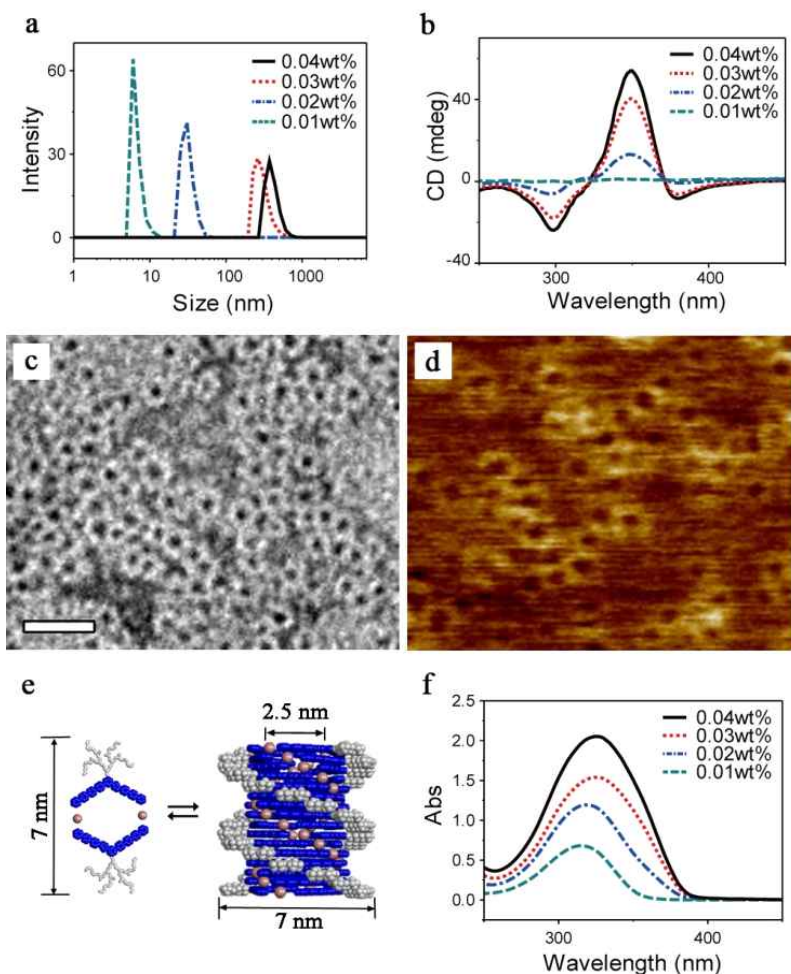


Figure 5. (a) Size distribution from DLS measurements and (b) CD spectra of aqueous solutions of **1** with Ag(I) ions at decreasing concentrations from 0.04 to 0.01 wt %. (c) TEM image (scale bar = 25 nm) and (d) AFM image (250 nm × 200 nm) of aqueous solution of **1** with Ag(I) ions (0.01 wt %). (e) Schematic representation of the switch between Ag(I) ion-mediated dimeric macrocyclic structure and the tubular structure. (f) UV spectra of **1** with Ag(I) ions in aqueous solution at various concentrations.

The question arose in this step whether the helical structures were based on helical folding of the coordination-bonded polymeric chains or helical stacking of metal-mediated aromatic macrocycles. To answer this question, we performed dynamic light scattering (DLS) experiments using diluted solutions of **1** with decreasing concentration (Figure 5a). As the concentration decreased from 0.03 to 0.01 wt %, the size (hydrodynamic diameter) abruptly decreased from 200 to 8 nm, suggesting that the helical objects originated from helical stacking of small objects rather than helical folding of polymeric chains. When the diluted solution with a concentration of 0.01 wt % was subjected to TEM measurements, uniform toroidal structures were observed (Figure 5c). The electron density profile showed that the external diameter and the diameter of the internal cavity of the toroid were 7 and 2.5 nm, respectively. To provide further confirmation of the formation of the toroids, we performed AFM measurements on samples prepared by drop-casting of the 0.01 wt % aqueous solution onto the SiO₂/Si wafer (Figure 5d). The image clearly revealed toroidal objects with a height of 4 Å, demonstrating that the toroidal objects were single stacks of these macrocycles.

To gain further insight into the toroidal structure, we conducted vapor pressure osmometry (VPO) measurements in tetrahydrofuran solution over the concentration range 8.5-17.0 g/kg (sample/solvent). The molecular weight of the primary aggregate was measured to be 3902 Da, which is 2 times larger than that of a single molecule containing a silver ion (1894 Da) (Figure 6), indicating the metal-containing dimeric association. All of these observations, together with inspection of Corey.Pauling.Koltun (CPK) models, indicate that **1** self-assembles into dimeric macrocycles formed through coordination bonding interactions between pyridines and Ag(I) ions under diluted

conditions at a concentration of 0.01 wt % (Figure 5e).

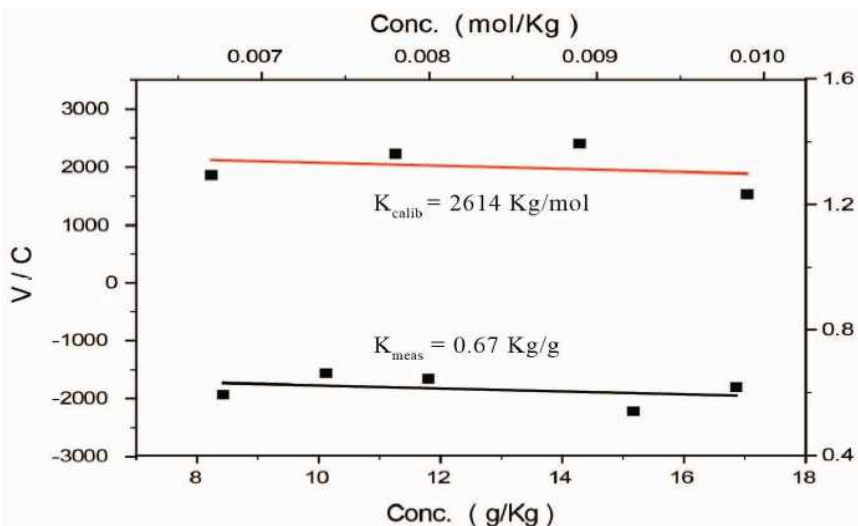


Figure 6. VPO results using R¹OTs as a standard for the determination of K of the instrument, $K_{\text{calib}} = 2614 \text{ Kg/mol}$ and **1** as sample, $K_{\text{meas}} = 0.67 \text{ Kg/g}$. Molecular Weight = $K_{\text{calib}}/K_{\text{meas}} = 3901.5 \text{ g/mol}$. Calculated for [dimer of **1** + 2 Ag] : 3786.4 g/mol.

On the basis of these results, it can be concluded that the helical objects observed for a complex solution with a concentration of 0.03 wt % consisted of helical stacks of Ag(I) ion-mediated dimeric macrocycles that resulted in a tubular structure with an external diameter of 7 nm and an internal cavity diameter of 2.5 nm (Figure 5e). The formation of tubules based on helical stacks of the macrocycles is also reflected in the preservation of the external dimension of the macrocycle, which was essentially unaltered relative to that of the helical objects even after the concentration was increased. CD spectra showed increased intensity with increasing concentration (Figure 5b), indicative of helical stacking of the macrocycles with a

preferred handedness, which is consistent with the results observed by TEM and AFM. This result demonstrates that the primary dimeric macrocycles stack on top of each other with mutual rotation in the same direction. Consequently, this helically staggered stacking of the dimeric macrocycles leads to a tubular structure with a left-handed supramolecular chirality (Figure 5e).

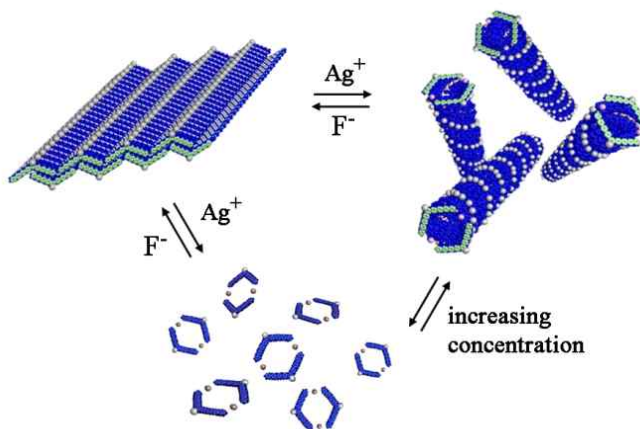


Figure 7. Schematic representation of reversible transformation through flat sheets, helical tubules and discrete toroids in response to external stimuli.

The results described here demonstrate that Ag(I) ions trigger drastic supramolecular switching between nonchiral flat sheets and helical tubules with supramolecular chirality (Figure 7). This structural transformation originates from the dissociation of the zigzag polymer chains through a breakup of the π - π stacking interactions upon the addition of silver salt to form discrete dimeric macrocycles mediated by strong coordination bonding interactions.¹⁰ The breakup of the π - π stacking interactions upon the addition of silver salt is manifested in the blue shift of the absorption maximum ($\lambda_{\text{max}} = 315 \text{ nm}$) relative to that of the dilute solution of **1** at a concentration of 0.01 wt % (λ_{max}

= 333 nm).³ This blue shift of the absorption maximum ($\lambda_{\max} = 325$ to 315 nm) was also observed with decreasing concentration of the Ag(I) complex solution (Figure 5f), indicating the absence of π - π stacking interactions under dilute conditions at a concentration of 0.01 wt %. It should be mentioned that the blue-shifted absorption maximum was also observed for the molecularly dissolved state in CHCl_3 solution (Figure 2c). When Bu_4NF was added to break the coordination bond interactions through decomplexation, the absorption maximum was red-shifted to recover that of the solution of **1**, indicating that the decomplexed aromatic segments reassemble into the sheets through π - π stacking interactions, as confirmed by TEM.

On the basis of all of the data described here, the sheets can be considered to undergo a drastic transformation into helical tubules at a higher concentration and a transformation into discrete dimeric macrocycles at a lower concentration through reversible coordination interactions between the pyridine units of the aromatic segments and Ag(I) ions (Figure 7). Another interesting point to be noted is that the metal-containing macrocycles reversibly stack on top of each other to form helical tubules in response to a variation in the concentration. The primary driving force responsible for the metal-directed switching behavior of the sheets is the dominant coordination interactions between the pyridine units of the aromatic segments and Ag(I) ions, which overcome the weak stacking interactions of the aromatic segments. This interplay of different non-covalent interactions allows the 2D structures to be transformed immediately into helical or macrocyclic structures depending on the concentration.

Conclusion

In conclusion, we have demonstrated that stimuli-responsive 2D structures can be constructed by the aqueous self-assembly of bent-shaped aromatic rods containing pyridine units at their terminals. The sheets respond to Ag(I) ions by changing their shape into helical tubules at a higher concentration and discrete macrocycles at a lower concentration. It is worth noting that the metal-containing macrocycles reversibly stack on top of each other to form helical tubules in response to the variation in concentration. In comparison with conventional fixed 2D structures,¹⁴ the most notable feature of our systems is their ability to respond to external stimuli by a direct structural change from nonchiral flat 2D structures to 1D hollow structures with helical pores. Such a unique switch of the open sheets into closed tubules with helical pores opens up the new possibility of using the 2D structures to capture specific proteins selectively in their helical interior and release them to their target.

Experimental section

Characterization

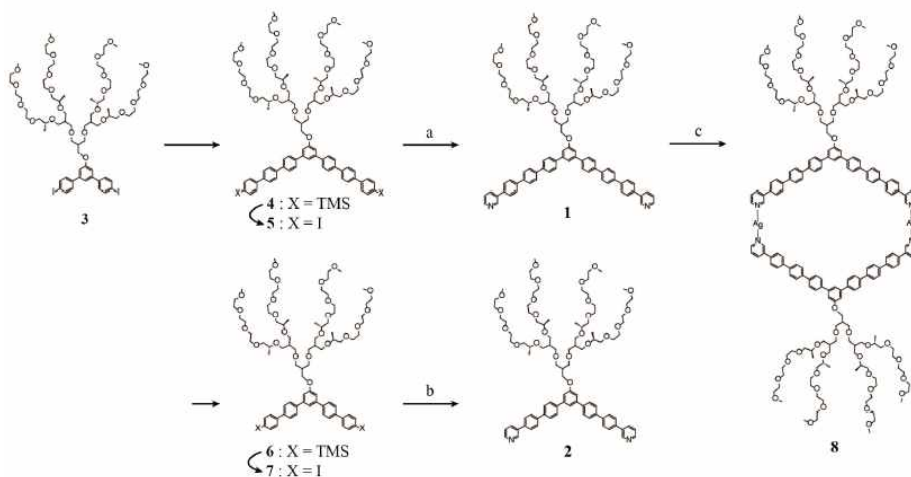
¹H-NMR and ¹³C-NMR spectra were recorded from CDCl₃ solutions on a Bruker Avance DPX-300. The purity of the products was checked by thin layer chromatography (TLC; Merck, silica gel 60). Recycling preparative high-pressure chromatography (HPLC) was performed for further purification by using HITACHI model pump L-7110, JAI model UV detector 310 and JAI model RI detector RI-7S. The UV/vis spectrometer was obtained from Hitachi U-2900. The fluorescence spectra were obtained from a Hitachi F-7000 Fluorescence Spectrophotometer. Circular Dichroism (CD) spectra were obtained using Jasco J-810 spectropolarimeter. The AFM measurements were performed using a Nanoscope IIIa microscope (Veeco Instruments, Santa Barbara, CA) in air at ambient temperature (ca. 25 °C) with standard silicon cantilevers (NCH, NanoWorld, Neuchatel, Switzerland) in the tapping mode. VPO measurements were performed with Knauer K-7000 vapor pressure osmometer in THF solution. Compounds were synthesized according to the procedure described scheme 1. The DLS measurements were performed using an ALV/CGS-3 Compact Goniometer System. MALDI TOF-MS spectroscopy (MALDI-ToF-MS) was performed on a Bruker Microflex LRF20 using α -cyano-4-hydroxy cinnamic acid (CHCA) as matrix.

Materials

Tetrakis(triphenylphosphine) palladium(0) (99 %), NaH (60 %), and p-toluenesulfonyl chloride (98 %) from TCI and Tokyo Kasei were used as received. 2,6-dibromophenol, 4-phenylboronic acid, iodine monochloride (1.0 M solution in dichloromethane), boron tribromide (1.0 M solution in dichloromethane) from Aldrich were used as

received. Unless otherwise indicated, all starting materials were obtained from commercial suppliers (Aldrich, Lancaster, and TCI, etc.) and were used without purification. Methylene chloride, acetonitrile, and THF were distilled before use. Visualization was accomplished with UV light and iodine vapor. Flash chromatography was carried out with Silica Gel 60 (230-400 mesh) from EM Science.

Material Synthesis



Scheme 1. Synthetic routes to compound **1** and **2**

Compounds **3-7** were prepared according to the procedures as described previously⁸

Compounds **1** and **2** : Compounds **1** and **2** were synthesized using the same procedure. A representative example is described for compound **1**. **5** (150 mg, 0.079 mmol), and 3-pyridylboronic acid (29 mg, 0.239mmol) were dissolved in degassed THF (2 ml). Degassed 2.0 M aqueous K_2CO_3 (1 ml) was added to the solution and then tetrakis(triphenylphosphine) palladium(0) (35 mg, 30 μ mol) was added.

The mixture was refluxed for 24 hrs with vigorous stirring under argon. Cooled to room temperature, the layers were separated, the aqueous layer was washed twice with ethyl acetate. The combined organic layer was dried over anhydrous MgSO_4 and filtered. The solvent was removed in a rotary evaporator, and the crude products was purified by column chromatography (silica gel, ethyl acetate : methanol = 8 : 1) and then was purified by recrystallization (cyclohexane : acetone = 10 : 1) to yield 55 mg of white waxy solid.

1 : yield 39%. $^1\text{H-NMR}$ (300MHz, CDCl_3) δ 8.93 (s, 2H), 8.62 (d, J = 3.3 Hz, 2H), 7.94 (d, J = 7.8 Hz, 2H), 7.80 . 7.77 (m, 20H), 7.70 (d, J = 8.1 Hz, 4H), 7.51 (s, 1H), 7.40 (dd, J = 5.0, 7.7 Hz, 2H), 7.21 (s, 1H), 4.19 (d, J = 5.1 Hz, 2H), 3.63 . 3.31 (m, 88H), 2.45 (quin, J = 5.4 Hz, 1H), 2.10 (quin, J = 5.7 Hz, 2H), 1.10 (d, J = 6.0 Hz, 12H); $^{13}\text{C NMR}$ (75MHz, CDCl_3) δ 160.2, 148.8, 148.5, 142.8, 140.6, 140.4, 140.1, 139.9, 139.6, 137.0, 136.3, 134.4, 127.9, 127.9, 127.8, 127.7, 127.7, 127.6, 123.8, 118.6, 112.5, 77.7, 77.2, 76.8, 75.2, 75.0, 75.0, 72.1, 70.9, 70.8, 70.8, 70.7, 69.8, 69.6, 67.6, 59.2, 41.0, 40.3, 17.3; MALDI-TOF-MS $[\text{M}+\text{H}]^+$ calcd for $\text{C}_{104}\text{H}_{141}\text{N}_2\text{O}_{23}$: 1785.99; Found : 1786.05; $[\text{M}+\text{Na}]^+$ calcd for $\text{C}_{104}\text{H}_{140}\text{N}_2\text{NaO}_{23}$: 1807.97; Found: 1807.94.

2 : **7** (130 mg, 0.075 mmol), 3-pyridylboronic acid (28 mg, 0.225 mmol) and tetrakis(triphenylphosphine) palladium(0) (35 mg, 30 μ mol) were refluxed in mixture of 2.0 M aqueous K_2CO_3 (1.5 ml) and degassed THF (2 ml) for 24 hrs to yield 45 mg of white waxy solid **2** : yield 37%. $^1\text{H-NMR}$ (300MHz, CDCl_3) δ 8.92 (s, 2H), 8.62 (d, J = 3.6 Hz, 2H), 7.95 (d, J = 7.8 Hz, 2H), 7.79 (d, J = 8.1 Hz, 4H), 7.76 (s, 8H), 7.70 (d, J = 8.4 Hz, 4H), 7.50 (s, 1H), 7.40 (dd, J = 4.8, 7.8 Hz, 2H), 7.20 (s, 2H), 4.18 (d, J = 5.1 Hz, 2H), 3.63 . 3.31 (m,

88H), 2.43 (quin, $J = 5.4$ Hz, 1H), 2.10 (quin, $J = 5.6$ Hz, 2H), 1.09 (d, $J = 6.0$ Hz, 12H); ^{13}C NMR (75MHz, CDCl_3) δ 160.2, 148.8, 148.5, 142.7, 140.6, 140.5, 139.7, 137.1, 136.3, 134.4, 127.9, 127.9, 127.8, 127.6, 123.8, 118.6, 112.5, 77.7, 77.2, 76.8, 75.2, 75.0, 72.1, 70.9, 70.8, 70.7, 69.8, 69.5, 67.6, 59.2, 41.0, 40.3, 17.3; MALDI-TOF-MS $[\text{M}+\text{Na}]^+$ calcd for $\text{C}_{92}\text{H}_{132}\text{N}_2\text{NaO}_{23}$: 1655.91; Found: 1656.19; $[\text{M}+\text{K}]^+$ calcd for $\text{C}_{92}\text{H}_{132}\text{KN}_2\text{O}_{23}$: 1671.89; Found: 1672.15.

8 : Complexation of **1** with silver triflates : **1** (3 mg, 1.7 μ mol) was dissolved in water (10 ml) and then silver triflate (0.44 mg, 1.7 μ mol) was added to the solution. The mixture solution was vortexed about 5 min. At 25°C. MALDI-TOF-MS $[\text{M}+\text{Ag}]^+$ calcd for $\text{C}_{104}\text{H}_{140}\text{AgN}_2\text{O}_{23}$: 1891.89; Found: 1893.22

TEM Experiments

Transmission electron microscopy observation was carried out with a JEOL JEM-2100 operated at 120 kV. The cryogenic transmission electron microscopy (cryo-TEM) experiments were performed with a thin film of aqueous solution of amphiphiles (5 ML) transferred to a lacey supported grid. The thin aqueous films were prepared under controlled temperature and humidity conditions (97.99%) within a custom-built environmental chamber in order to prevent evaporation of water from sample solution. The excess liquid was blotted with filter paper for 2-3 seconds, and the thin aqueous films were rapidly vitrified by plunging them into liquid ethane (cooled by liquid nitrogen) at its freezing point. The grid was transferred, on a Gatan 626 cryoholder, using a cryo-transfer device and transferred to a JEM-2010 TEM. Direct imaging was carried out at a temperature of approximately -175 °C and with a 120 kV accelerating voltage, using the images acquired with a

Dual vision 300 W and SC 1000 CCD camera (Gatan, Inc.; Warrendale, PA)

Supporting information

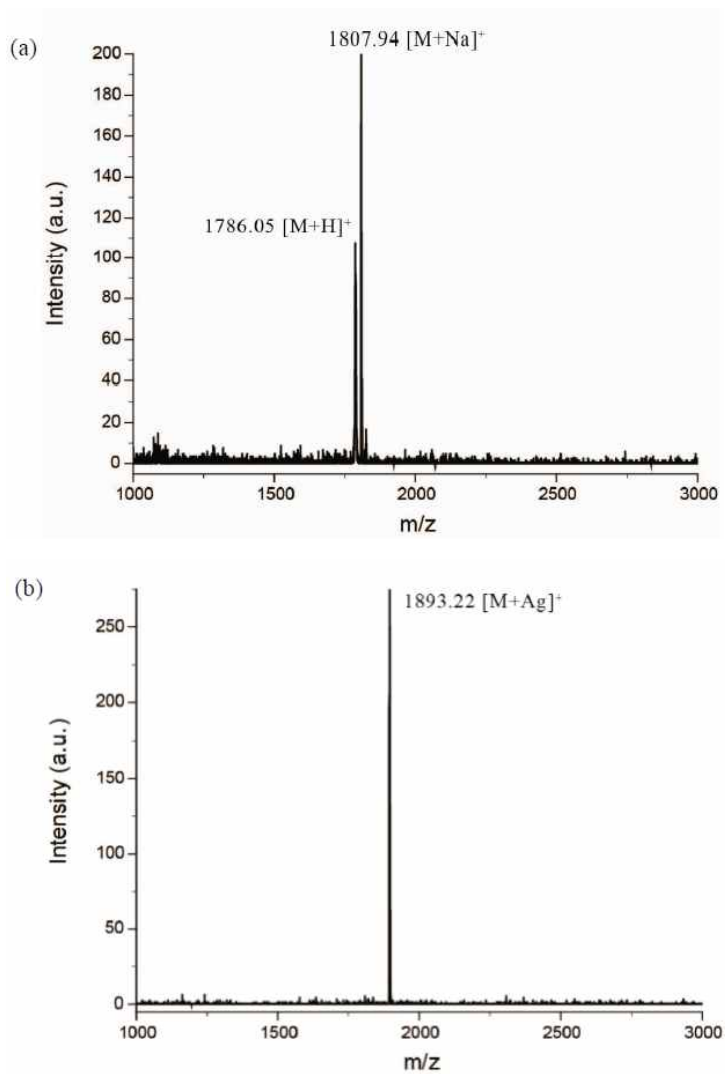


Figure S1. MALDI-TOF results of (a) **1** and (b) **8**.

References

[†]Portions of this chapter have been previously reported, see: Shin, S.; Lim, S.; Kim, Y.; Kim, T.; Choi, T.-L.; Lee, M. *J. Am. Chem. Soc.* **2013**, *135*, 2156.

(1) (a) Aida, T.; Meijer, E. W.; Stupp, S. I. *Science* **2012**, *335*, 813. (b) De Greef, T. F. A.; Smulders, M. M. J.; Wolffs, M.; Schenning, A. P. H. J.; Sijbesma, R. P.; Meijer, E. W. *Chem. Rev.* **2009**, *109*, 5687.

(2) (a) Yagai, S.; Kinoshita, T.; Kikkawa, Y.; Karatsu, T.; Kitamura, A.; Honsho, Y.; Seki, S. *Chem. Eur. J.* **2009**, *15*, 9320. (b) Kim, H.-J.; Kim, T.; Lee, M. *Acc. Chem. Res.* **2010**, *44*, 72. (c) Goto, H.; Furusho, Y.; Yashima, E. *J. Am. Chem. Soc.* **2007**, *129*, 109.

(3) (a) Ryu, J.-H.; Hong, D.-J.; Lee, M. *Chem. Commun.* **2008**, 1043.

(b) Huang, Z.; Kang, S.-K.; Lee, M. *J. Mater. Chem.* **2011**, *21*, 15327.

(4) Kim, J.-K.; Lee, E.; Lim, Y.-b.; Lee, M. *Angew. Chem., Int. Ed.* **2008**, *47*, 4662.

(5) Lee, E.; Kim, J.-K.; Lee, M. *Angew. Chem., Int. Ed.* **2009**, *48*, 3657.

(6) Kim, H.-J.; Kang, S.-K.; Lee, Y.-K.; Seok, C.; Lee, J.-K.; Zin, W.-C.; Lee, M. *Angew. Chem., Int. Ed.* **2010**, *122*, 8649.

(7) Huang, Z.; Kang, S.-K.; Banno, M.; Yamaguchi, T.; Lee, D.; Seok, C.; Yashima, E.; Lee, M. *Science* **2012**, *337*, 1521.

(8) Kim, H.-J.; Liu, F.; Ryu, J.-H.; Kang, S.-K.; Zeng, X.; Ungar, G.; Lee, J.-K.; Zin, W.-C.; Lee, M. *J. Am. Chem. Soc.* **2012**, *134*, 13871.

(9) Khlobystov, A. N.; Blake, A. J.; Champness, N. R.; Lemenovskii, D. A.; Majouga, A. G.; Zyk, N. V.; Schroder, M. *Coord. Chem. Rev.* **2001**, *222*, 155.

(10) (a) Wilkinson, G.; Gillard, R. D.; McCleverty, J. A. *Comprehensive Coordination Chemistry: The Synthesis, Reactions, Properties and Applications of Coordination Compounds*; Pergamon

- Press: Oxford, U.K., 1987. (b) Zhang, J.; Moore, J. S. *J. Am. Chem. Soc.* **1992**, *114*, 9701.
- (11) Bae, J.; Choi, J.-H.; Yoo, Y.-S.; Oh, N.-K.; Kim, B.-S.; Lee, M. *J. Am. Chem. Soc.* **2005**, *127*, 9668.
- (12) Kilpin, K. J.; Gower, M. L.; Telfer, S. G.; Jameson, G. B.; Crowley, J. D. *Inorg. Chem.* **2011**, *50*, 1123.
- (13) Kim, H.-J.; Lee, J.-H.; Lee, M. *Angew. Chem., Int. Ed.* **2005**, *44*, 5810.
- (14) (a) Nam, K. T.; Shelby, S. A.; Choi, P. H.; Marciel, A. B.; Chen, R.; Tan, L.; Chu, T. K.; Mesch, R. A.; Lee, B. C.; Connolly, M. D.; Kisielowski, C.; Zuckermann, R. N. *Nat. Mater.* **2010**, *9*, 454. (b) Tang, Z.; Zhang, Z.; Wang, Y.; Glotzer, S. C.; Kotov, N. A. *Science* **2006**, *314*, 274.

국문 초록

용액상에서의 블록공중합체 자기조립 전략의 발전은 나노구조를 원하는 잘 조절된 형태와 기능을 갖도록 만드는 것을 가능하게 하였다. 이렇게 개발된 새로운 나노구조가 실질적인 응용으로 발전하기 위해서는 나노구조를 효율적이고 쉽게 준비할 수 있는 방법에 대한 연구가 필요함에도 불구하고, 이에 관련된 연구는 상대적으로 제한적이었다. 본 논문에서는 유용한 성질을 가진 공액고분자 블록공중합체로 이루어진 나노구조를 준비하는 매우 간단한 방법에 대하여 네 장에 걸쳐 소개하고자 한다.

제 2장에서는 polyacetylene (PA)의 블록공중합체를 이용해 전도성 고분자의 중합과 자기조립 현상이 단일 과정으로 이루어지는 방법을 개발하였다. 고리개환복분해중합을 이용한 블록 공중합체의 합성에 사용된 단량체들인 nobornene (NB) 유도체와 cyclooctatetraene (COT)의 큰 중합속도의 차이를 이용하여, 각 단량체가 혼합물 상태에서도 순차적으로 반응하여 단 한번의 개시반응으로 블록 공중합체가 중합될 수 있었다. 또한 중합된 PA 블록은 용매에 녹지 않는 성질을 가져 중합 도중 바로 나노구조를 형성하였다. 이러한 방법에 있어 다른 종류의 단량체인 *endo*-tricyclo[4.2.2.0]deca-3,9-diene (TD) 유도체의 사용이 중합 반응성 및 나노구조의 형성에 미치는 영향 또한 연구되었다.

제 3장에서는 앞서 개발한 방법을 통해 형광성질으로 유용한 poly(*para*-phenylenevinylene) (PPV)의 블록공중합체를 이용한 자기조립 현상을 연구하였다. PPV의 단량체는 다른 단량체와의 반응성 차이가 COT보다 더욱 커 혼합물 상태에서의 공중합체 중합이 더욱 블록 공중합체에 가깝게 이루어졌다. 또한 반응성의 매우 큰 차이가 반응 도중에 형성되는 자기조립 현상에 미치는 영향이 확인되었고, 이를 통해 독특한 프랙탈 나노구조를 형성할 수 있었다.

제 4장에서는 methoxy 기를 도입한 PPV의 블록 공중합체를

이용하여 혼합물 상태에서의 완벽한 블록 공중합체로의 순차적 중합에 성공하였다. 또한 중합 직후 좋은 용해도를 보여 나노구조를 이루지 않는 시스-구조가 간단한 빛 쪼임 과정으로 용해도가 나쁜 트랜스-구조로 매우 빠르게 이성질화 된 후 결정구조를 이루어 1D 형태의 나노구조를 형성하는 것을 확인하였다. 만들어진 구조는 마치 고분자의 리빙-중합과 같은 방식으로 구조의 길이와 자람을 조절할 수 있었다.

마지막 장에서는 제 3장에서 발표한 방법으로 준비한 형광 성질을 갖는 나노구조를 수용액상 센서로 응용한 예를 보고하였다. 수용액상에서도 안정하게 존재하는 나노구조들의 형광을 띠는 PPV 핵 구조가 2,4,6-trinitrotoluene (TNT)와 같은 폭발성 화합물을 높은 효율의 형광 소거 반응으로 감지하는 것을 확인하였다. 또한, 나노구조의 형태에 따른 감도의 차이와, 대전된 분자들 사이에서 중성의 폭발성 분자들만 선택적으로 감지하는 현상에 대하여 기술하였다.

종합하면, 본 논문에서는 블록 공중합체를 단량체의 혼합물에서부터 단 한번의 반응으로 중합하는 간단한 합성법과, 중합 도중에 자기조립 구조를 형성하거나, 간단한 빛 쪼임으로 자기조립 구조를 형성하는 간단한 자기조립방법을 조합하여 공액고분자로 이루어진 나노구조체를 손쉽게 준비하는 전략에 대해 설명하였다. 또한 본 전략을 이용해 준비한 형광성 나노구조체를 수용액상 폭발물 감지 센서로 응용하는 예시를 제안하였다. 이와 같은 본 논문의 연구가 유용한 나노구조체를 간단하게 만들 수 있는 다양한 전략의 확보에 기여하기를 바란다.

주요어: 전도성 고분자의 직접적 자기 조립 현상, 단일 개시 블록 공중합체 중합법, 고리개환복분해중합법, 폴리아세틸렌, 폴리파라페닐렌 비닐렌, 결정화 유도 자기조립법, 화학 센서

학번: 2012-20281